UNIVERSITY OF CAPE TOWN
IYUNIVESITHI YASEKAPA • UNIVERSITEIT VAN KAAPSTAD

ANALYTICAL BEHAVIOUR OF FRP STRENGTHENED REINFORCED CONCRETE BEAMS UNDER LOW VELOCITY IMPACT LOAD INCORPORATING RATE DEPENDENT MATERIAL CONSTITUTIVE MODELS

By

ALTON RUITERS

Submitted in partial fulfilment of the requirements for the degree

MSc Eng

DEPARTMENT OF CIVIL ENGINEERING

FACULTY OF ENGINEERING AND BUILT ENVIRONMENT

UNIVERSITY OF CAPE TOWN

Supervisor: Prof. P. Moyo

February 2014

DECLARATION

I know the meaning of plagiarism and declare that all the work in the document, accept for that which is properly acknowledged, is my own.

Signature……

Date…….

In loving memory of my father, Peter Solomon Ruiters.

ACKNOWLEDGEMENTS

Praise be to God for his blessings and love.

I would like to express my sincere gratitude to my supervisor, Prof. Pilate Moyo, for his guidance, advice and encouragement during the research period at the University of Cape Town. It was a privilege to study under your supervision.

Special thanks to my mom, brothers and extended family for their love, prayers and unwavering support.

Finally, a special word of thanks to my wife, Shivvon. Your love, support and patience remains true and constant. For that, I am blessed and grateful.

ABSTRACT

Since the 1980s, the use of fibre reinforced polymer (FRP) composites in strengthening and rehabilitation of existing reinforced and prestressed structures has gained popularity. Versatility, high strength to weight ratio, corrosion resistance, excellent creep and fatigue behaviour, and ease of installation are amongst some of the advantages offered by externally bonded FRP systems over traditional strengthening methods.

In addition to strengthening for static loading, there are many scenarios where strengthening is required to elements subjected to dynamic loads. The static behaviour of FRP strengthened RC beams has been the subject of extensive research. However, the dynamic behaviour of FRP strengthened RC beam elements remains unclear. Limited experimental studies are available that are focused on the response of FRP strengthened RC beams subjected to low velocity impact events. Furthermore, many of the Finite Element (FE) analysis models developed in these studies yielded results that were inconsistent with the test data. Key shortcomings of these models relate to a lack of definition of the FRP-concrete bond interface and considering rate dependent material behaviour.

In an attempt to address these limitations, the aim of this study is to develop and verify a numerical model based on the finite element (FE) approach, capable of describing the dynamic response of FRP strengthened beams subjected to low velocity impact by accounting for FRP interfacial bond behaviour and dynamic properties of constituent materials at high strain rates. The FE model was developed in Abaqus/Explicit version 6.10.

The FE model was verified through comparisons of its predictions with test results of selected experimental impact studies by Tang (2002) and Tang & Saadatmanesh (2003). Mid span displacement and support reaction force time histories as well as crack patterns were compared against the results of the impact tests A total of four test beam specimens, with different impact energies and FRP laminate types, was

simulated. Results of the comparison demonstrate that the FE model shows reasonable agreement with observed peak displacements and reactions, whilst some discrepancies were noted for frequencies of the associated peak responses. However, for subsequent reaction and deflection cycles, the FE computed response showed a closer correlation with observed cycles.

TABLE OF CONTENTS

LIST OF FIGURES

LIST OF TABLES

1 INTRODUCTION

1.1 Background

Rehabilitation and repair of existing civil infrastructure, particularly concrete structures, is becoming of increasing importance to utility owners, researchers and engineers. In the United States of America alone, it was estimated that the backlog in maintenance and repair of 600 000 bridges amounts to US$200 billion (Institute of Civil Engineers, 2008). The need for the rehabilitation and repair of reinforced concrete (RC) structures is driven by the following key aspects related to structural deficiency and degradation (Hollaway *et al*, 2008):

- *Change in use:* Structures may be subjected load to intensities and configurations that differ from the original design concept.
- *Degradation*: The serviceability and ultimate capacity of structures may be adversely affected with excessive deterioration of its components. Deterioration mechanisms include corrosion and fatigue. Hazard events such as impact and blast loading can also result in structural degradation.

The most common method of strengthening for RC structures employing epoxy bonded steel plates were introduced in the 1960s (Täljsten, 2004). Despite the widespread use of this method, it poses some disadvantages. Steel plates are subject to corrosion, should protective coatings fail and degrade. Steel plates are cumbersome to handle and install, requiring extensive temporary support systems. Sustained contact pressure is required during the hardening phase of the epoxy adhesive thereby prolonging disruption to users.

Since the 1980s, the use of fibre reinforced polymer (FRP) composites in strengthening and rehabilitation of existing RC and prestressed structures as an alternative to steel has gained popularity (Hollaway *et al*, 2008). Figure 1 provides an overview of the development of FRP composites in civil engineering from the early 1970s into the 21st century.

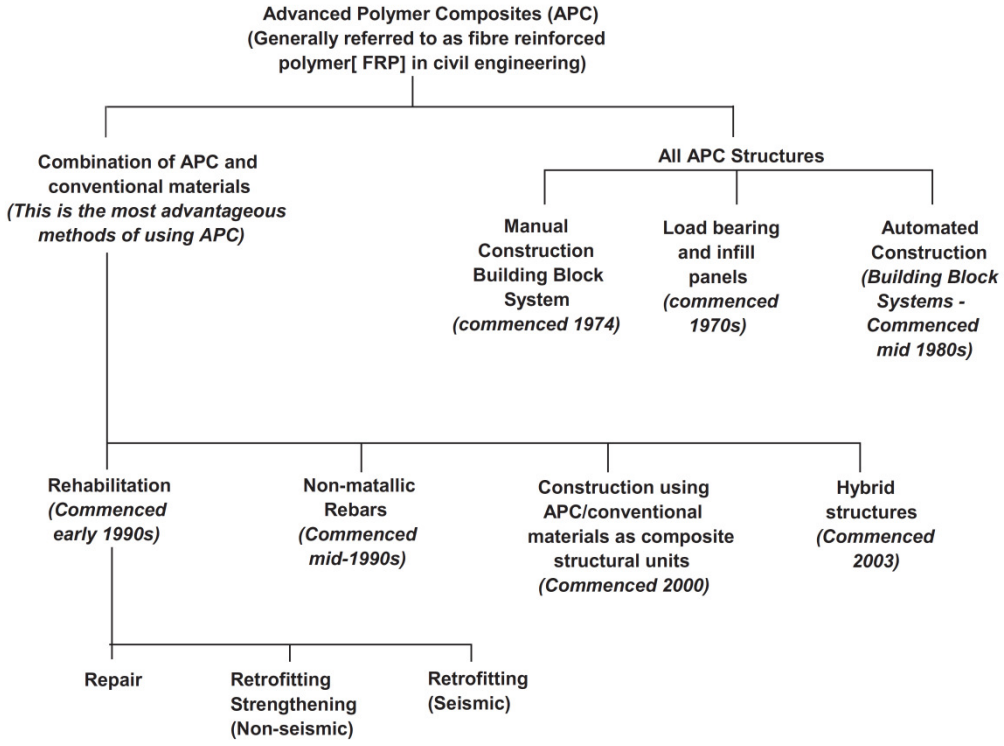

Figure 1: Development of FRP composite systems (Hollaway, 2010)

Versatility, high strength to weight ratio, corrosion resistance, excellent creep and fatigue behaviour, and ease of installation owing to low weight are amongst the advantages offered by externally bonded FRP systems over strengthening methods employing steel (Perumalsamy *et al*, 2009; Lin *et al*, 2001).

1.2 Brief overview of FRP strengthening of concrete structures

FRP composites comprise of two constituents, namely fibre reinforcement and the matrix material. Carbon, aramid, and glass are the typical fibre reinforcements used in structural strengthening applications as the load bearing components. Matrices, commonly in the form of epoxy resin, provide the shear load path between the fibre components and the concrete substrate.

FRP strengthening techniques may be used to improve strength, stiffness, and fatigue behaviour of RC structural elements (Perumalsamy *et al*, 2009). In addition to

strengthening for static loading, there are many scenarios where strengthening is required to elements subjected to dynamic loads. For example, bridge deck beams may be strengthened to withstand accidental vehicular impact and transient traffic loading. Furthermore, structural elements of buildings may be retrofitted with FRP to withstand seismic events, wind loads, and blast impact.

In the last few decades, numerous studies were undertaken to define the static behaviour of FRP strengthened concrete elements (Teng *et al*, 2002; Teng *et al*, 2003). This ongoing research has led to the development of several design guideline documents (Ceci *et al*, 2012; CRC Construction Innovation, 2002). On the other hand, research focused on the dynamic response of FRP strengthened concrete elements remains in its infancy despite the potential of this method for retrofitting and strengthening existing structures subjected to dynamic loading (Hamed & Rabinovitch, 2007). Limited experimental studies have been conducted to investigate the dynamic response of FRP strengthened beams under low velocity impact (Jerome, 1996; Erki & Meier, 1999; White *et al*, 2001; Capozucca & Nilde Cerri, 2002; Tang, 2002). Analytical and numerical models presented in most of these studies predicted the dynamic response with varying degrees of accuracy. These variations are related to the complexity in defining and integrating dynamic parameters unique to the analysis of FRP strengthened RC beams. These include the definition of suitable constitutive and FRP bond interface models.

The strength, stiffness and ductility behaviour of concrete may differ substantially under high loading rates when compared to that of the static loading condition (Grote *et al*, 2001; Tang, 2002). Therefore, the rate dependent response of materials is an important consideration in defining material models for dynamic analyses.

FRP debonding, either by laminate peeling or bond splitting of the cover concrete, is a common failure mechanism for beams strengthened for increased flexural strength (Perumalsamy *et al*, 2009; Hollaway *et al*, 2008; White *et al*, 2001). Hence, integrating suitable FRP bond interface models in dynamic analyses is essential to capture the full-spectrum response of the FRP strengthened beam.

1.3 Aim of research

Owing to limitations of existing studies for the prediction and evaluation of the dynamic response of FRP strengthened beams subjected to low velocity impact, it is proposed to develop an analysis tool using finite element code capable of describing the dynamic response by accounting for FRP interfacial bond behaviour and dynamic properties of constituent materials at high loading rates.

1.4 Hypothesis statement

A finite element (FE) model based on appropriate load-rate dependent constitutive models that accounts for FRP interfacial bond behaviour can provide accurate predictions of the dynamic response of the FRP strengthened beams under low velocity impacts.

1.5 Objectives and scope of study

The following are the key objectives of the study:

i) To understand the behavior of FRP strengthened RC beams.

ii) To understand the dynamic behaviour of concrete at high loading rates and methods used in the analysis thereof.

iii) To develop a numerical model based on the finite element approach capable of describing the dynamic response of FRP strengthened beams subjected to low velocity impact.

1.6 Limitations

The study will be limited to the investigation of the dynamic response of rectangular RC beams strengthened for flexure with uni-directional FRP subjected to a single impact event.

1.7 Report structure

This report consists of six chapters, organized as follow.

Chapter 1 gives the background of this research project and the objectives of the study. The formulated hypothesis and limitations of study also form this chapter.

Chapter 2 provides a literature review on the behaviour of FRP strengthened RC beams, the dynamic response of concrete at high loading rates, and impact analysis methods.

Chapter 3 presents the theoretical framework for the development of the FE model. Structural dynamic theories, constitutive material models, and FRP bond interface models considered for model implementation are described in this chapter.

Chapter 4 describes the development of the FE model using the Abaqus modelling programme.

Chapter 5 reports the findings and observations of the study.

Chapter 6 summarizes the work of this report; draws conclusions and gives recommendations for future work.

2 LITERATURE REVIEW

2.1 Introduction

During the last decades, numerous studies have been undertaken on the use of FRP strengthening as a means of extending the services life of existing RC structures (Teng *et al*, 2002; Teng *et al*, 2003). This ongoing research has led to the development of several design guideline documents (Ceci *et al*, 2012; CRC Construction Innovation, 2002). Although the static behaviour of FRP strengthened RC beams are well documented, dynamic behaviour remains unclear. Dynamic behaviour is influenced by the strain-rate effects on constituent materials. A fundamental understanding of the static behaviour of FRP strengthened beams is essential in investigating the response of constituent materials at high-loading rates.

2.2 FRP strengthening of RC beams

Structurally deficient RC beams may be strengthened by employing either near surface mounted (NSM) FRP rods or FRP external plate bonding (EPB). Flexural or shear strengthening using the NSM technique entails cutting a groove in the concrete cover region into which a FRP rod of circular or rectangular cross section is secured in place with an epoxy paste The FRP EPB strengthening method involves the bonding of FRP sheets or fabric on the external face of the RC beam using an epoxy adhesive (Hollaway, 2010).

Externally-bonded FRP composites comprise of two constituents, namely fibre reinforcement and the matrix material. Carbon (CFRP), Aramid (AFRP) and Glass (GFRP) are the typical fibre reinforcements used in structural engineering applications as the load bearing components. Matrices, commonly in the form of epoxy resin, provide the shear load path between the fibre components and the concrete substrate. FRP installations are generally classified into two categories, namely wet lay-up systems and prefabricated systems. Wet lay-up systems are in situ techniques where the dry unidirectional or multidirectional fibre sheets or fabrics are saturated with resin at the installation site. Prefabricated systems involve pre-

manufactured cured FRP plates or sheets that are installed to the concrete substrate with the use of adhesives (FIB, 2001; ACI, 1996).

The wet lay-up system is one of the most cost efficient and readily deployable techniques for the external strengthening of structures. The dry fibre fabric of this system can be easily transported to the work site in manageable rolls and is mouldable to suit a variety of conditions on-site. This technique may be used for shear and flexural strengthening of RC beams.

2.2.1 FRP strengthening for shear

According to Hollaway *et al* (2008), FRP strengthening for shear may be considered when an RC beam is deficient in shear or when its shear capacity is less than the flexural capacity. Flexural failure is ductile and allows for stress redistribution whereas shear failure is brittle and catastrophic. Therefore, flexural failure is generally preferred to shear failure as the governing failure mode (Hollaway, L. C.; Teng, J. G. Eds, 2008).

Shear strength enhancement of RC beams with the use of externally bonded FRP may be achieved using various techniques. For beams, FRP sheets or strips may be applied to side faces, side faces and tension face or complete wrapping to all faces (ACI, 2002). Effective shear strengthening is achieved by orienting fibres parallel to the direction of the maximum principal tensile stress (i.e. perpendicularly to potential shear cracks), although it is normally more practical to orientate fibres transversely to the beam axis (FIB, 2001; Zureick *et al*, 2010; ACI, 2002). For load reversal conditions associated with seismic events, fibres may be applied in two different directions to ensure shear strength enhancement for both directions (Hollaway *et al*, 2008). Typical shear strengthening schemes are shown in Figure 2.

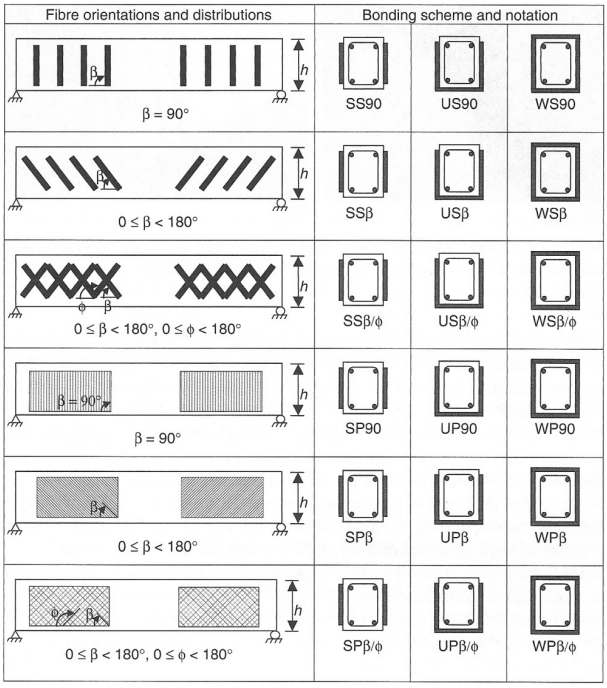

Figure 2: Typical shear strengthening schemes using externally bonded FRP (Hollaway and Teng, 2008)

The notation presented in Figure 2 represents the bonding configuration (**S**ides, **U**-Shape or **W**rapped), fibre distribution (**S**trips or **P**lates) and orientation of the primary and secondary fibres (degrees).

Numerous studies have demonstrated the effectiveness of FRP strengthening in increasing the shear capacity of beams (Perumalsamy *et al*, 2009). Results from selected studies are presented to illustrate the efficacy of FRP shear strengthening schemes.

Mosallam and Banerjee (2007) studied the shear enhancement of RC beams externally strengthened with CFRP and GFRP. Full-scale beam specimens were prepared for three different classes; namely unstrengthened, pre-damaged and FRP retrofitted. The pre-damaged beams were repaired with epoxy resin crack injection prior to FRP application and load testing. Large stirrup spacing was used to ensure that all beams were deficient in shear. Test results showed that the FRP succeeded in restoring the original shear capacity of the pre-damaged specimens. Ultimate shear capacity of the retrofitted specimens was increased by 56% and 42%, in comparison to the unstrengthened specimens, for the CFRP and GFRP laminates respectively.

Furthermore, strengthened specimens exhibited a more ductile flexural failure mode, together with increased deflections at ultimate load, in comparison to the brittle shear failure of the unstrengthened specimens.

Mitolidis *et al* (2012) conducted a comparative study for CFRP and steel reinforced polymers (SRP) in flexural and shear strengthening of RC beams. Low strength concrete was used in the production of the specimens to simulate concrete grades typically found in existing RC structures. The mean concrete cube strength was recorded as 26.4 MPa. Test results indicated substantial shear enhancement for the CFRP strengthened specimens. Shear strength increases of 90% were observed. Furthermore, the preferable ductile flexural failure behaviour noted by Mossallam and Banerjee (2007) was replicated in this study.

2.2.2 FRP strengthening for flexure

Since its initial development in 1982 by the Swiss Federal laboratory for Materials Testing and Research (EMPA), the FRP strengthening technique has proven effective in addressing structural deficiencies in RC beams (Meier, 1995). Flexural strengthening of RC beams with FRP entails the attachment of FRP fabric or pultruded plates to the extreme tension face of the beam as shown in Figure 3.

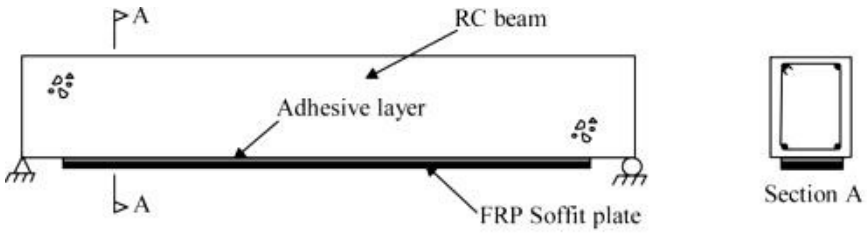

Figure 3: RC beam bonded with soffit FRP plate (Smith and Teng, 2002)

The main consequences of flexural strengthening are increased strength and reduced ductility (Hollaway *et al*, 2008). Outcomes of selected experimental studies are presented to demonstrate these enhancements.

Ceroni (2010) studied the behaviour of RC beams strengthened for flexure using CFRP and near Surface Mounted (NSM) bars under monotonic and cyclic loads. Cyclic load tests comprised the application of 10 cycles in the elastic and post-elastic range. RC beams under monotonic loading showed strength increases varying between 26% and 50% for relatively low steel reinforcement ratios (1%). For higher ratios (1.5%), strength increases between 17% and 33% were observed. Furthermore, these beams exhibited reduced ductility owing to the brittle of FRP failure and increased stiffness when compared to unstrengthened control beams. CFRP strengthened beams tested under cyclic loading showed a strength reduction ranging from 10% to 13% compared to similar monotonically loaded beams.

Kachlakev and McCurry (2000) evaluated the load carrying capacity and bending characteristics of full-scale FRP strengthened RC beams replicated from an existing bridge. Four-point bending tests were conducted on beam specimens strengthened for shear and flexure with varying configurations of CFRP and GFRP. The beams were tested for the design traffic loads to reproduce the loading conditions of the existing bridge. For the beam strengthened in flexure, results showed an increase in static load capacity and midspan deflection at failure of 145% and 124% respectively, when compared to test data of the unstrengthened control beam.

2.2.3 Failure modes for FRP strengthened RC beams

Several unique failure modes of RC beams strengthened with FRP have been identified in numerous experimental studies (Saxena *et al*, 2008; Hollaway and Teng, 2008). FIB (2001) defined two broad classes into which these failure modes may be categorised. These include those where the full composite action of the beam is maintained until compressive failure of the concrete is attained, and where the debonding of the FRP occurs prior to the concrete failure.

Typical failure modes identified in flexural load tests on more than 70 FRP strengthened RC beam specimens, having spans between 2m and 7m, conducted by the Swiss Federal Laboratories for Materials Testing and Research (EMPA) are shown in Figure 4 (Meier, 1995).

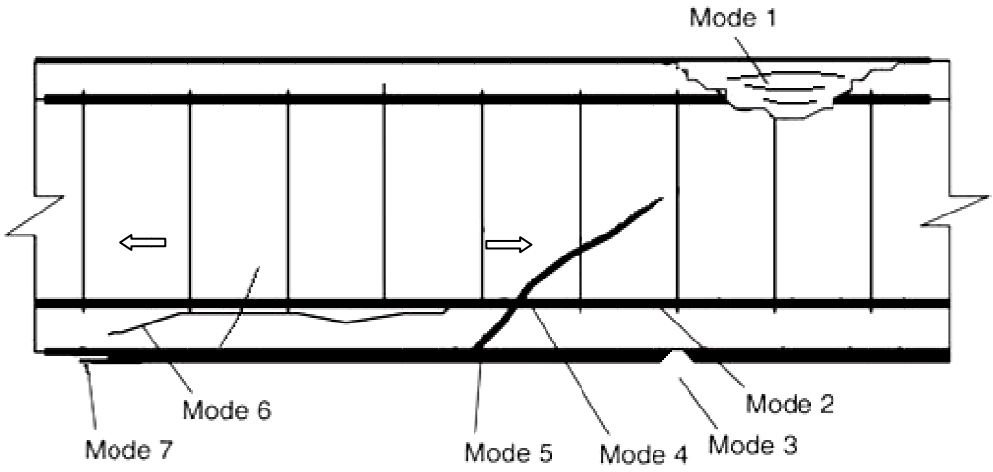

Mode 1	*Concrete crushing*
Mode 2	*Yield of tensile steel reinforcement*
Mode 3	*Tensile rupture of FRP plate*
Mode 4	*Shear failure of concrete in tension zone*
Mode 5	*Local FRP peel due to vertical displacement at shear crack*
Mode 6	*Delamination of cover concrete*
Mode 7	*Plate end interfacial debonding*
Mode 8	*Adhesive failure at concrete-adhesive interface*
Mode 9	*Adhesive failure at adhesive-FRP interface*
Mode 10	*Inter-laminar shear within the FRP plate*

Figure 4: Typical failure modes in RC beams strengthened by FRP's

(Adopted from Meier, 1995 & Hollaway and Head, 2001)

Failure for under-reinforced RC beams strengthened with FRP initiates with mode 2 (yield of tensile reinforcement) followed by mode 1 (concrete crushing). Mode 3 (FRP rupture) may govern when an under-reinforced RC beam remains under-reinforced after FRP strengthening. Conversely, failure of over-reinforced RC beams strengthened with FRP initiates with mode 1 (concrete crushing) followed by mode 2 (yield of tensile reinforcement). Mode 6 (concrete cover delamination) may propagate outwards from shear or flexural cracks in the beam midspan region or inwards from the plate end zones. Mode 7 (FRP peeling at anchorage) results from the high interfacial shear and normal stresses in this region of the beam (Saxena *et al*, 2008; Hollaway and Teng, 2008; Park and Hewson, 2008).

These modes are useful in describing the mechanisms for shear, flexure and debonding failures. An overview of these failure modes is presented in the following sections.

Shear failure modes

The shear failure mechanism for RC beams strengthened with FRP is similar to RC beams without FRP strengthening since it is associated with the propagation of either a single critical diagonal shear crack or multiple diagonal shear cracks (Hollaway *et al*, 2008). Numerous studies have shown that the shear failure of FRP strengthened beams mainly occur in one of the two modes (Cheng & Teng, 2003a). These include tensile rupture of FRP and FRP debonding from the sides of the RC beam. The shear failure mode for a given FRP strengthened RC beam depends on the configuration of the strengthening scheme (Arya *et al*, 2002).

FRP rupture at shear cracks:

FRP rupture is related to the strain behaviour of the fibres intersecting diagonal shear cracks in the concrete member (Chen & Teng, 2003b). As the width of the diagonal crack increases, the FRP is stretched until a strain level is attained when rupture initiates in the most highly stressed point in the FRP. This strain is termed the effective strain $\varepsilon_{frp,e}$ and is generally less than the tensile fracture strain $\varepsilon_{frp,u}$ owing to local stress concentrations in the fibres (FIB, 2001; Khalifa *et al*, 1998). FRP rupture propagates along the diagonal shear crack leading to collapse of the RC beam (Chen & Teng, 2003b). Results of available test data indicate that FRP rupture has occurred in the majority of beams strengthened using FRP sheets and in some beams strengthened with U-jackets (Hollaway *et al*, 2008).

Several studies were undertaken in the development of models to predict the shear strength of FRP strengthened RC beams. Chen and Teng (2003a) reviewed existing models and accounted for their deficiencies in developing rational shear strength design models for beams. The authors recognised that different models were required to account for each of the predominant shear failure modes, namely FRP debonding and FRP rupture. The model accounts for various strengthening configurations and the non-uniform stress distribution in the FRP along a shear crack in the case of FRP rupture.

The contribution of FRP to shear strength of a RC strengthened beam with failure by FRP rupture is given by (Chen and Teng, 2003a):

$$\mathrm{V_{FRP}} = 2\frac{f_{FRP,ed}}{\gamma_{FRP}} t_{FRP} w_{FRP} \frac{h_{FRP,e}\,(sin\beta + cos\beta)}{s_{FRP}} \tag{2.1}$$

Where:
- $f_{FRP,ed}$ – Average/effective design stress of FRP
- γ_{FRP} – Partial safety factor
- t_{FRP} – Thickness of FRP
- $h_{FRP,e}$ – Effective height of FRP on the sides of the beam
- w_{FRP} – Width of FRP strip
- β – Angle of inclination of FRP fibre
- s_{FRP} – Spacing of FRP strips

The design effective stress $f_{FRP,ed}$ is given by

$$f_{FRP,ed} = D_{FRP}\delta_{FRP,max} \tag{2.2}$$

where D_{FRP} is termed the stress distribution factor, and $\delta_{FRP,max}$ is the maximum tensile stress in the FRP. The stress distribution factor D_{FRP} describes the non-uniform strain distribution in FRP along a shear crack. The maximum design stress $\delta_{FRP,max}$ is the factored ultimate tensile strength of the FRP to account for the strength reduction that may result from stress concentrations at the corners of the beam. These parameters are given by:

$$D_{FRP} = 0.5\ (FRP\ U - jacket\ and\ \ wrapping) \tag{2.3}$$

$$\delta_{FRP,max} = \begin{cases} 0.8 f_{FRP} & if\ \dfrac{f_{FRP}}{E_{FRP}} \leq\ \varepsilon_{max} \\ 0.8\varepsilon_{max} E_{FRP} & if\ \dfrac{f_{FRP}}{E_{FRP}} >\ \varepsilon_{max} \end{cases} \tag{2.4}$$

with E_{FRP} being the Young's modulus of FRP, f_{FRP} the tensile strength of FRP, and ε_{max} the maximum usable strain of FRP for shear strengthening.

FRP debonding at shear cracks:

FRP debonding is governed by the ultimate bond strength between the FRP and the concrete (Chen & Teng, 2003b). High tensile stresses develop in the FRP intersecting the critical shear crack due to the vertical separation of the concrete on either side of the crack. Interfacial bond stresses provide the transfer mechanism for the tensile stress between FRP and concrete. FRP debonding occurs when the interfacial bond is compromised prior to the tensile rupture of the FRP (Khalifa *et al*, 1998). Current experimental data shows that failure due to FRP debonding occurs in almost all beams with FRP side strips and in the majority of beams strengthened with U-jackets (Hollaway *et al*, 2008).

As with FRP rupture, Chen & Teng (2003b) developed a shear strength model for the FRP debonding failure mode. The model accounts for the non-uniform stress distribution in the FRP along a shear crack and the bond strength between FRP and concrete. Whilst the contribution of FRP to shear strength with FRP debonding failure is also given by equation (2.1), the maximum design stress in the FRP $\delta_{FRP,max}$ in equation (2.4), is obtained by using the 95th percentile characteristic value of the bond strength given by (Chen & Teng, 2003b):

$$\delta_{FRP,max} = 0.315\beta_w\beta_L\sqrt{\frac{E_{FRP}}{t_{FRP}}\sqrt{f'_c}} \leq f_{FRP} \qquad (2.5)$$

with β_w being the FRP bond length coefficient, β_L the FRP strip width coefficient and f'_c concrete cylinder compressive strength.

Factors influencing shear failure modes:

Extensive investigations have been undertaken in defining factors influencing the shear behaviour and failure modes for RC beams with FRP shear enhancement.

Bousselham and Chaallal (2004) synthesised the findings of research studies carried out thus far on shear strengthening of RC beams with externally bonded FRP. In excess of one hundred tests were considered in the synthesis. The study focused on the analysis of parameters that have the greatest influence on the shear behaviour. It was concluded that the shear span ratio, longitudinal steel reinforcement ratio, and the

geometry of the member also have influence on the shear behaviour in addition to the shear steel reinforcement and FRP properties.

In later experimental studies, Bousselham and Chaallal (2004) evaluated the capacity of various strengthening systems in the rehabilitation of shear deficient RC beams. The composite systems evaluated in the study included wet layup CFRP U-jacket strips, GFRP U-jacket strips and pre-cured vertical CFRP strips. The authors concluded that shear span-to-depth ratio *(a/d)* has a significant effect on the shear strength capacity of FRP strengthened RC beams. Furthermore, it was noted that the shear span-to-depth ratio has a significant role in determining the shear failure mode. For a/d ratios less than 2.5, the failure is predominantly by FRP rupture whereas values more than 3.2 are associated with FRP debonding.

Flexural failure modes

Flexural failure of FRP strengthened beams occur in one of the two brittle and explosive modes, namely tensile rupture of FRP and compressive crushing of the concrete (Buyukozturk & Hearing, 1998). FRP rupture initiates after yielding of the tensile steel in under-reinforced beams, whereas concrete crushing occurs when the concrete compression strain attains the maximum failure strain in over-reinforced beams (FIB, 2001; Hollaway *et al*, 2008).

Numerous studies have been conducted to evaluate the flexural behaviour and strength of FRP strengthened beams. Most researchers have concluded that the analysis of the ultimate moment capacity of the strengthened beam, in both failure modes, may be determined based on stress-strain equilibrium (Buyukozturk & Hearing, 1998).

Using this approach, Teng *et al* (2002) presented an expression for the moment capacity M_u of the strengthened beam as follows:

$$M_u = k_1 \frac{f_{cu}}{\gamma_c} b_c x \left(\frac{h}{2} - k_2 x\right) + \sum_{i=1}^{n} \delta_{si} A_{si} \left(\frac{h}{2} - d_{si}\right) + \delta_{frp} A_{frp} \left(\frac{h}{2} - d_{frp}\right) \qquad (2.6)$$

where k_1 and k_2 are the mean stress and centroid factors, respectively; f_{cu} is the concrete cube compressive strength; γ_c is the partial safety factor for concrete; b_c is the beam width; x is the depth of the neutral axis; δ_{si} and δ_{frp} are the stresses in the steel bars and FRP, respectively; A_{si} is the total area of steel in i, n is the total number of steel layers; A_{frp} is the area of FRP; d_{si} and d_{frp} are distances from the extreme concrete compression fibre to the neutral axis, the centroid of steel bars in layer i and the centroid of the FRP, respectively.

The flexural failure mode may be determined for a beam with a given FRP ratio ρ_{frp} by evaluating the critical FRP ratio $\rho_{frp,cr}$ given by:

$$\rho_{frp,cr} = \frac{k_1 \frac{f_{cu}}{\gamma_c} \frac{x_{cr}}{h} + \sum_{i=1}^{n} \delta_{si} \rho_{si}}{\frac{f_{frp}}{\gamma_{frp}}} \tag{2.7}$$

where γ_{frp} is the partial safety factor for FRP, ρ_{si} is the steel reinforcement ratio of layer i, and x_{cr} is the critical depth of the neutral axis. The beam fails by FRP rupture if $\rho_{frp} > \rho_{frp,cr}$, however beam failure by concrete crushing occurs if $\rho_{frp} < \rho_{frp,cr}$.

Factors influencing flexural failure modes:

The behaviour of RC beams strengthened for flexure has been the focus of extensive research (Ceroni, 2010; Kachlakev & McCurry, 2000). The variation of reported strength increases and failure modes is attributable to the characteristics of the FRP system and RC beam specimens employed in testing regimes (Kachlakev & McCurry, 2000). These include type, thickness, and fibre orientation for the FRP system, and geometry, steel reinforcement ratio and original condition for the RC beam.

Chajes *et al* (1994) evaluated the flexural capacity of RC beams strengthened with different FRP systems. Four-point bending tests were conducted on RC beams strengthened with CFRP, AFRP and GFRP. For the strengthened beams, the reported increases in flexural capacity ranged from 36 to 57%, with flexural stiffness increases ranging from 45 to 53%. For the beams strengthened with GFRP and CFRP, the

observed failures were as a result of tensile rupture of the FRP in the maximum moment region. The beams reinforced with AFRP failed due to the crushing of the compression concrete.

Toutanji *et al* (2006) investigated the behaviour of RC beams strengthened with FRP using varying layer configurations, bonded with an inorganic matrix. FRP rupture was reported for beams strengthened with three and four layers of FRP, whereas FRP delamination failure was noted for the beams strengthened with five and six layers. Furthermore, the ultimate moment capacity increase ranged from 42.6% to 70.2% for the addition of three and six layers, respectively.

FRP debonding failure modes

FRP debonding in RC elements occur in regions of high stress concentrations, which are generally associated with material discontinuities and with the presence of shear or bending crack flaws (Buyukozturk *et al*, 2004). Debonding occurs either within the concrete cover zone or the interfacial zone between the concrete surface and the FRP layers. This premature failure mode is brittle as it occurs before steel yielding and is therefore undesirable (Saxena *et al*, 2008). Debonding failure modes are shown in Figure 5.

.

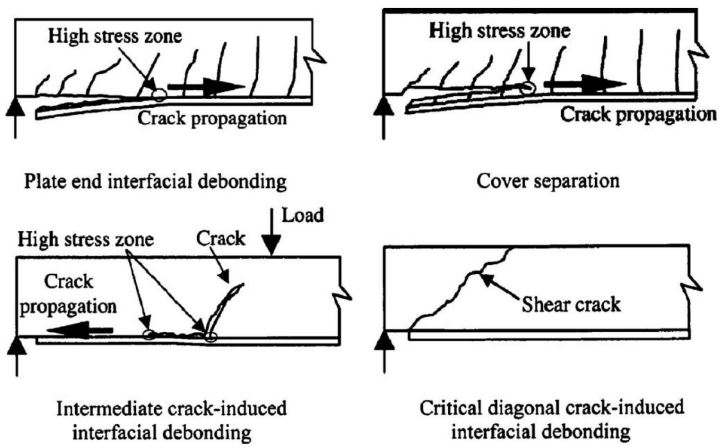

Figure 5: Debonding failure modes in RC beams strengthened by FRP's (Saxena, 2008)

Concrete-cover separation:

According to Saxena *et al* (2008), concrete-cover separation is characterised by a crack forming in the vicinity of the FRP plate end, propagating to the tension

reinforcement level then propagating horizontally along the reinforcement level, thereby resulting in separation of the cover concrete.

Plate-end interfacial debonding:
Plate end interfacial debonding occurs in the concrete layer adjacent to the interfacial zone between concrete and the FRP adhesive (Saxena *et al*, 2008). This failure mode is associated with high interfacial shear and normal stresses near the FRP plate end (Hollaway *et al*, 2008). Since the ultimate tensile and shear strength of the epoxy adhesive is generally greater than that of the adjacent concrete, debonding occurs within the concrete zone (FIB, 2001).

Intermediate crack-induced interfacial debonding:
Cracks formed by shear or flexural fracture in the RC beam results in high localised stresses in the FRP plate. The resulting localised FRP debonding propagates towards the nearest plate end when the interfacial stresses between FRP and concrete reach critical values under increasing loading (Meier, 1995; Hollaway *et al*, 2008).

Critical diagonal crack-induced interfacial debonding:
This mode occurs in the region of low moment and high shear stress (i.e. near the plate end of a simply supported beam) of RC beams strengthened for flexure. Major diagonal shear cracks propagate in this region, intersecting the FRP plate near the plate end. The debonding crack propagates towards the plate end when the high interfacial stresses between the FRP plate and concrete, at the widening crack tip, attains critical failure levels (Hollaway *et al*, 2008).

2.3 Response of RC structures subjected to impact load

According to Fujikake *et al* (2009), the response of a structural component under impact loading consists of two phases, as shown in Figure 6. The first phase corresponds to the response due to the stress wave that occurs at the loading point during a short period after contact. This peak response depends on the test apparatus, weight of impactor and specimen support conditions. The second phase relates to the overall response due to the elastic-plastic dynamic behaviour of constituent materials

and the loading rate effect. Typically, dynamic loading results in an amplification of the overall structural response of the structure.

Thus, an understanding of dynamic loading and the associated amplification response of the structure is essential to the development of appropriate analyses tools for FRP strengthened RC beams subjected to impact loading. An overview of dynamic loading, impact test methods and concrete behaviour under dynamic loading is presented in the sections that follow

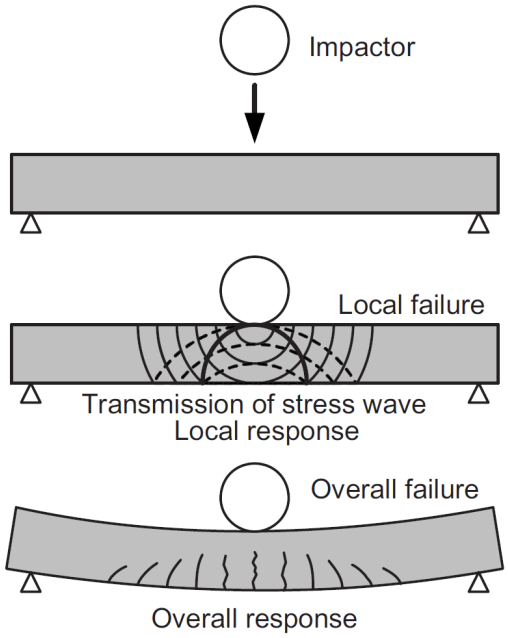

Figure 6: Dynamic response of RC member under impact loading (Fujikake et al, 2009)

2.3.1 Time-dependent classification of dynamic loading

Loads on structures are generally classified as either static or dynamic based on the magnitude of inertial forces, and their duration of application and variation with time. Static loads are long-term applications with negligible variation in intensity with time. Conversely, dynamic loads are loads that vary in both duration and intensity and generate inertial forces.

Dynamic loads may be classified into two categories, namely periodic and non-periodic, based on the attributes of the time variation (Clough & Penzien, 2003). Periodic loading involves the same time variation of a load for a large number of consecutive cycles. Sinusoidal simple harmonic motion is the simplest form of periodic loading. This form of periodic loading is generated by the unbalanced-mass effects in rotating machinery. Non-periodic loadings exhibit irregular time-history variations. These loads may be either long-duration loadings, such as seismic events, or short-duration impulsive loadings, such as explosion or impact (Clough & Penzien, 2003).

The effects of dynamic loads may be categorised within the time domain in terms of the strain rate ($\dot{\varepsilon}$) given by (Macaulay, 1987) :

$$\dot{\varepsilon} = \frac{d\varepsilon}{dt} \tag{2.8}$$

Strain rate, given in units of strain per second (s^{-1}), describes the rate of deformation of the material subjected to impact. The time duration for a given load event is inversely proportional to the induced strain rate. For instance, high strain rates associated with impact events occur over short time scales (Macaulay, 1987; Sierakowski & Chaturvedi, 1997). Typical loading types for various strain rate regimes are presented in Figure 7.

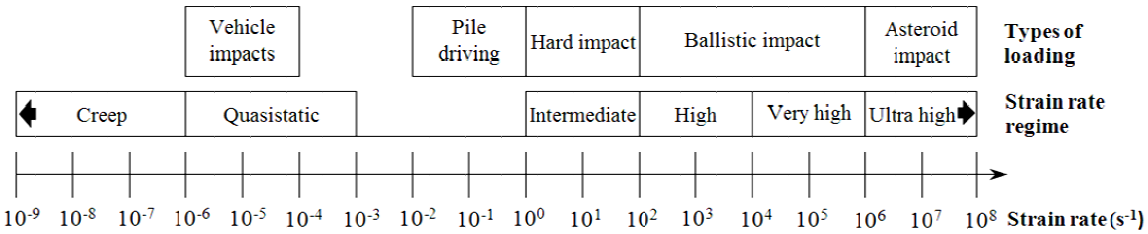

Figure 7: Loading types for various strain rate regimes
(Adopted from Sharpe, 2008 and Kappos, 2002)

For impulsive loads such as hard impact, projectile velocity is used as the classifying parameter. Impacts are generally defined as low, intermediate, or high velocity for most practical applications (Abrate, 2011). Impacts are classed as low velocity up to

10 m/s. This is based on test methods, such as the drop-weight impact test, employed in simulating impact events within the 10^0 s^{-1} to 10^2 s^{-1} strain rate range (Cantwell & Morton, 1991; Kilic, 2008; Sharpe, 2008). Impact velocities are defined as intermediate within the 10 m/s to 50 m/s range. Examples of this type of impact include secondary blast, hurricane and tornado debris. High velocity impacts, ranging from 50 m/s to 1000 m/s, are generally associated with ballistic projectiles (Kappos, 2002; Abrate, 2011).

The kinetic energy of the projectile determines the strain rate and mode of response of the target (Abrate, 1998; Kappos, 2002). High velocity impact of small projectiles leads to localised damage, as the impact duration is sufficiently short such that the target does not have time to respond. The response is dominated by stress wave propagation under high strain rate conditions. On the other hand, low velocity impacts of a large mass will result in a dynamic response of the target. The impact duration is sufficiently long to allow for the global response of the target, resulting in more energy being absorbed elastically (Abrate, 2011). Therefore, when assessing the dynamic response of a structure, careful consideration must be given to the selection of appropriate test methods to ensure that test conditions simulate impact loading experienced by the actual structure.

2.3.1.1 Low velocity impact testing

The mechanical behaviour of a concrete element is governed by the strain rate of the applied dynamic loading (Grote *et al*, 2001). Test methods have been developed to assess dynamic response and mechanical behaviour for a broad range of strain rates. Response in the high strain rate range (10^2 s^{-1} to 10^4 s^{-1}) may be assessed using the Hopkinson pressure bar tests and gas gun impact testing (Sharpe, 2008; Cantwell and Morton, 1991). For low velocity impact in the intermediate strain rate range (10^0 s^{-1} to 10^2 s^{-1}), methods include the split Hopkinson pressure bar tests and drop-weight impactor test (Sharpe, 2008; Grote *et al*, 2001). These methods are discussed in the sections that follow.

2.3.1.2 Split Hopkinson pressure bar test method

The split Hopkinson pressure bar (SHPB) test method is a commonly used experimental technique to determine the dynamic behaviour of a material in compression, tension and torsion (Gary & Bailly, 1998). A typical SHPB arrangement consists of a striker bar, short specimen, an input bar and an output bar as shown in Figure 8.

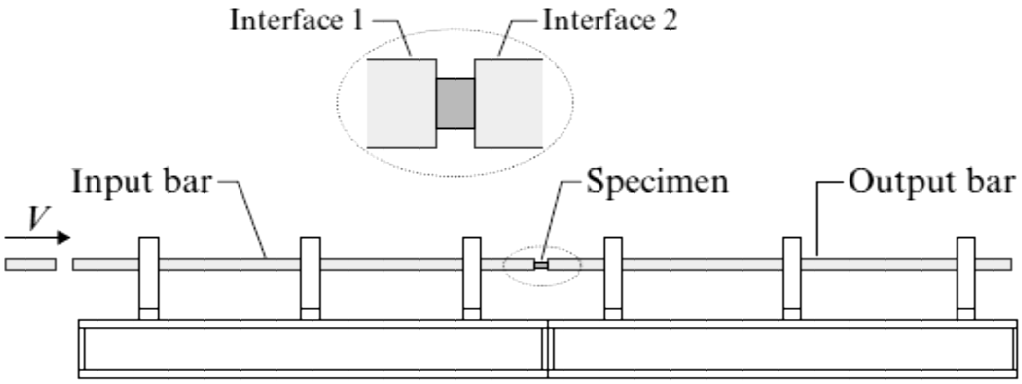

Figure 8: Schematic of the split Hopkinson pressure bar apparatus (Sharpe, 2008)

The striker bar impacts the input bar, generating a compressive longitudinal incident wave ε_I in the input bar. When the incident wave makes contact with the input bar-specimen interface, a reflected pulse $\varepsilon_R(t)$ and a transmitted pulse $\varepsilon_T(t)$ develops in the input bar and output bar respectively (Gary & Bailly, 1998; Sharpe, 2008).

By assuming stress equilibrium, uniform stress distribution in the specimen and one dimensional elastic stress wave propagation without dispersion in the bars, the strains induced in the input and output bars are used to determine the nominal compressive or tensile strain rate $\dot{\varepsilon}_s$, nominal strain ε_s and nominal stress σ_s in the specimen using (Sharpe, 2008; Yang & Shim, 2005):

$$\dot{\varepsilon}_s = -\frac{2c_0\varepsilon_R(t)}{L} \tag{2.9}$$

$$\varepsilon_s = \int_0^t \dot{\varepsilon}_s(\tau) d\,\tau \tag{2.10}$$

$$\dot{\sigma_s} = \frac{A_0 E_0 \varepsilon_T(t)}{A} \tag{2.11}$$

Where: A_0 – Cross-sectional area of input/output bar

E_0 – Young's modulus of input/output bar

c_0 – Wave speed of input/output bar

L – Length of specimen

A – Cross-sectional area of specimen

ε_R – Time-resolved axial strain of reflected wave in input bar

ε_T – Time-resolved axial strain in output bar

The negative sign in equation (2.9) relates to the direction of the reflected wave propagating in the opposite direction relative to the compressive incident wave. Thus, the strain rate in the specimen given by equation (2.9) is a positive compressive strain rate. (Sharpe, 2008). The stress–strain relationship of the specimen is determined from equation (2.9) and (2.11) by eliminating time as a variable.

2.3.1.3 Drop-weight impactor test method

The test apparatus consists of a drop tower equipped with a drop-weight. During the impact test, the drop-weight is allowed to fall from a pre-determined height to strike the test specimen. The equations of motion may be used to determine the contact velocity of the drop-weight. In most cases, the drop-weight is instrumented for the determination of the force-time history as shown in Figure 9. Impact energy is determined from the integration of the force-time signal. Furthermore, load cells may be installed at the supports of the specimen to measure reaction force.

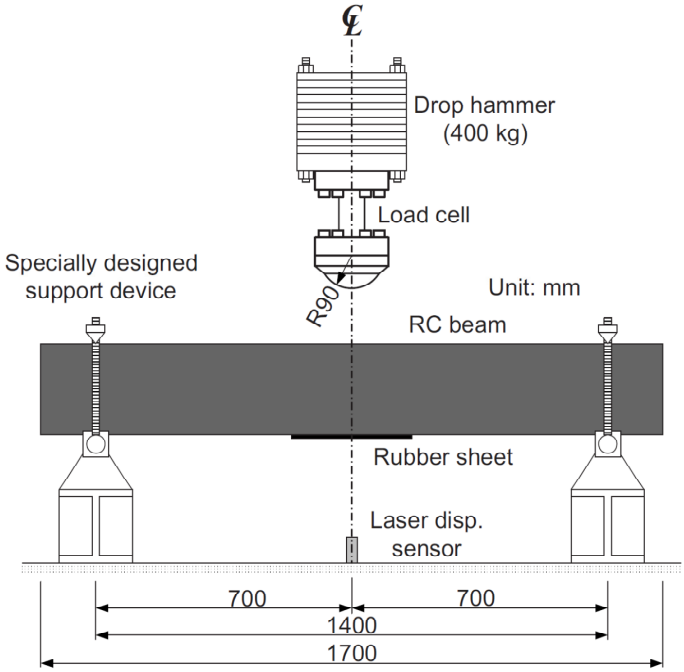

Figure 9: Drop-weight impact test setup by Fujikake (2009)

Other parameters recorded during the test include residual deflection, load-displacement history and energy-time history (Abrate, 2011; Cantwell and Morton, 1991).

2.3.2 Dynamic behaviour of concrete at high strain rates

The behaviour of concrete under dynamic loading differs from that associated with static loading. Concrete properties including stiffness, fracture energy, peak strain and compressive and tensile strength are highly dependent on the strain rate of applied loading (Barpi, 2004; Leppänen, 2002; Cusatis, 2011). Since the response of structures subjected to impact or blast loads is nonlinear, their design is generally based on a nonlinear analysis accounting for this strain rate effect (Mu *et al*, 2012). An understanding of the strain-rate dependent behaviour of concrete is therefore essential when developing analyses tools for the simulation of dynamic events.

Several authors have completed reviews of commonly published studies on the properties of concrete in both tension and compression under dynamic loading (Abu-Lebdeh *et al*, 2011; Fu *et al*, 1991; Malvar & Crawford, 1998a; Bischoff & Perry, 1991). The strength variation is typically reported as a dynamic increase factor (DIF),

defined as the ratio of dynamic to static strength (Mu *et al*, 2012). A summary of these reviews is presented in the sections that follow.

2.3.2.1 Strain rate effect on compressive strength

Bischoff and Perry (1991) conducted a comprehensive synthesis of experimental data on the rate dependent compressive behaviour of concrete, shown in Figure 10. The results indicate that the compressive strength increase with increasing strain rate. Furthermore, the authors identified two distinct modes of DIF development, each with a unique strain rate response. The first mode corresponds to the quasistatic strain rate range between 10^{-6} s^{-1} and 10 s^{-1}. The second mode corresponds to the intermediate strain rate range between 10 s^{-1} and 10^{3} s^{-1}.

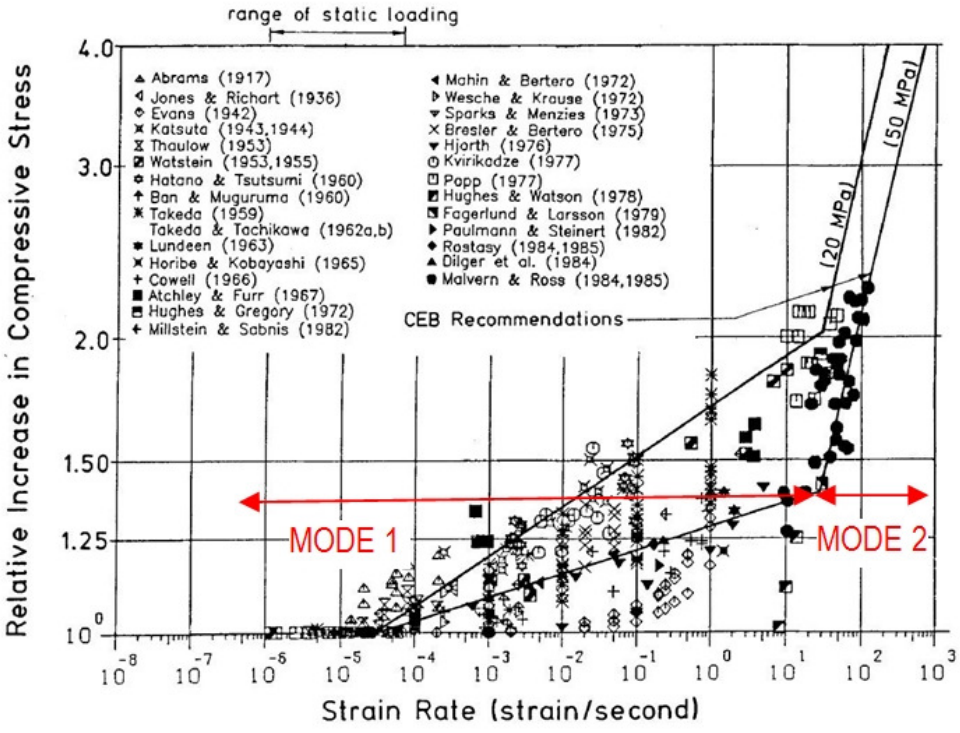

Figure 10: Compressive strength increase versus strain rate (Bischoff and Perry, 1991)

The first mode is attributable to the presence of free water in the micropores of the cement hydrate (Stéfan effect). Rossi (1997) idealised this mechanism as a thin film of viscous liquid trapped between two planar plates. The force F required to pull the plates apart at a velocity $\dot{h}$ is given by (Rossi, 1997):

$$F = \frac{3\eta V^2}{2\pi h^5} \cdot \dot{h} \tag{2.12}$$

Where: F – Separating force

η – Viscosity of liquid

h – Initial distance between the two plates

$\dot{h}$ – Velocity of separation of the two plates

V – Volume of liquid

In RC elements, the Stéfan effect is described by idealising the concrete matrix as a network of plates subjected to tensile strains. It may be approximated that the cohesive force between the plates in the presence of free water is proportional to the loading rate (Rossi, 1997; Zheng & Li, 2004).

The second mode is related to inertia effects which generate radial constraints acting as a confining pressure due to shielding of microcracks in the concrete (Ragueneau & Gatuingt, 2003; Georgin & Reynouard, 2003; Brara & Klepaczko, 2006). Inertial forces generated within the concrete are derived from the acceleration resulting from imposed loading and rapid microcrack development and propagation under dynamic loading. These inertial forces prevent the onset and propagation of further microcracks, thereby increasing levels of confinement within the concrete (Brara & Klepaczko, 2006; Rossi, 1997).

The results and parameters of existing experimental data on the compressive behaviour of concrete under high-rate loading are characterized by considerable scatter and variation (Cotsovos & Pavlovic, 2008). Cotsovos & Pavlovic (2008) evaluated the individual and combined effects of these parameters, using a finite element model, on the dynamic response of plain-concrete specimens. This was undertaken with the view to identifying the significance of their contribution to the overall scatter that characterises current experimental data. Parameters considered in this evaluation include the static uniaxial compressive strength of concrete f_c, the experimental techniques used for the tests, the shape and size content of the specimens, and the density and moisture content of the concrete. Results of the study

show that the individual effect of these parameters have a negligible influence on the scatter of experimental data. However, the combined effects, including an allowance for the variation in test method and strain definition employed in the past studies, explains the full extent of the scatter.

Furthermore, Bischoff and Perry (1991) concluded that although static compressive strength may have a significant effect on the compressive strain rate effect, the influence of mix proportion, aggregate type, cement content, age and curing conditions can be considered negligible or of uncertain importance.

For a given strain rate, the DIF for the parameters of the compressive stress-strain relation under high rates of loading may be estimated from recommendations by CEB Model Code 2010 (CEB-FIP, 2010) given by:

$$\frac{f'_{cd}}{f'_c} = \left(\frac{\dot{\varepsilon}_c}{30 \times 10^{-6}}\right)^{0.014} \tag{2.13}$$

$$\frac{E_{cd}}{E_c} = \left(\frac{\dot{\varepsilon}_c}{30 \times 10^{-6}}\right)^{0.026} \tag{2.14}$$

$$\frac{\varepsilon'_{cd}}{\varepsilon'_c} = \left(\frac{\dot{\varepsilon}_c}{30 \times 10^{-6}}\right)^{0.02} \tag{2.15}$$

where f'_{cd} is dynamic compressive strength, f'_c is compressive strength, E_c is initial elastic modulus, E_{cd} is dynamic elastic modulus, ε'_c is compressive strain at peak, and ε'_{cd} is the dynamic compressive strain at peak.

2.3.2.2 Strain rate effect on tensile strength

As with compressive behaviour, the response in tension may be defined in two distinct strain rate modes as shown in experimental review studies by Malvar and Crawford (1998a) presented in Figure 11.

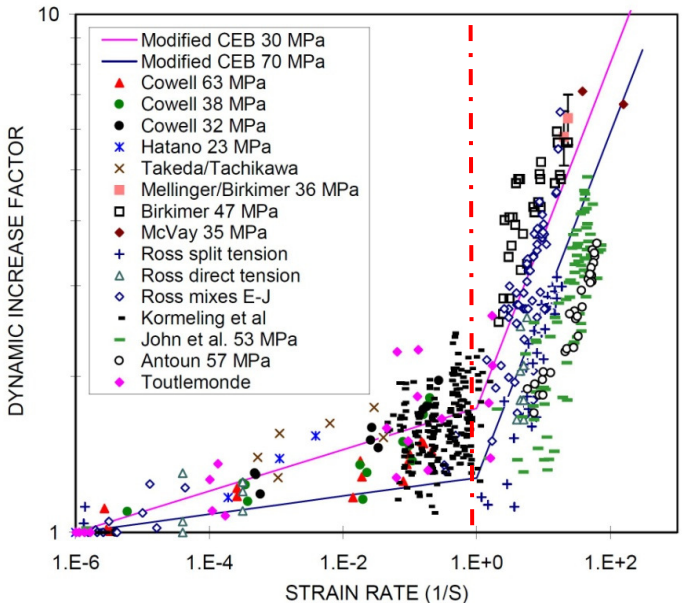

Figure 11: Tensile strength increase versus strain rate (Malvar and Crawford, 1998a)

However, the dynamic increase factors for both modes in tension are higher relative to the modes in compression. At the transition from quasistatic to intermediate strain rates at ~1 s^{-1} the DIF is about 2, whereas at higher strain rates of ~10^2 s^{-1} the DIF is about 100.

Although the first mode ($\dot{\varepsilon} < 1$ s^{-1}) may be attributable to the Stéfan effect, the mechanism describing the behaviour at higher strain rates remains unclear (Ragueneau & Gatuingt, 2003; Brara & Klepaczko, 2006). Brara and Klepaczko (2006) performed tension tests on several cylindrical specimens using a modified Split Hopkinson pressure bar at strain rates ranging from 10 s^{-1} to 120 s^{-1}. The results show that the strain rate effects above ~1 s^{-1} may be attributable to lateral inertial confinement and aggregate cleavage effects mobilised by the thermal vibration of atoms.

For a given strain rate, the DIF for the parameters of the tensile stress-strain relation under high rates of loading may be estimated from recommendations by CEB Model Code 2010 (CEB-FIP, 2010) given by:

$$\frac{f'_{td}}{f'_t} = \left(\frac{\dot{\varepsilon}_c}{1 \times 10^{-6}}\right)^{0.018} \tag{2.16}$$

$$\frac{E_{cd}}{E_c} = \left(\frac{\dot{\varepsilon}_c}{1 \times 10^{-6}}\right)^{0.026} \tag{2.17}$$

where f'_{td} is dynamic tensile strength and f'_c is tensile strength. Although there is no information in Model Code 2010 with regards the effect of strain rate on fracture energy and maximum crack opening displacement, these parameters may be assumed equal to the static values for strain rates up to 1 s^{-1} (Weerheijm & Van Doormaal, 2007). The dynamic response, due to strain rate effects, of FRP strengthened RC beams subjected to impact loading is discussed in the sections that follow.

2.3.3 Dynamic behaviour of FRP strengthened RC beams

The static behaviour of FRP strengthened RC elements, especially that of RC beams, has been the subject of extensive research owing to its increasing use in rehabilitating existing structures (Bonacci & Maalej, 2000; Teng & Smith, 2003). However, the dynamic behaviour of these elements remains unclear. Furthermore, almost all low-velocity impact research to date has focused on pure composite structures (Tang & Saadatmanesh, 2003). Limited experimental studies are available that are focused on the high-strain rate response of RC beams strengthened with FRP on the tension face.

Jerome (1996) compared the static and dynamic response of lightweight plain concrete beams strengthened with CFRP. The specimens were tested using the drop weight impact test method with dynamic load amplitudes of up to 44.5kN. Results show that the dynamic fracture energies, given by the area under the dynamic load-displacement curves, and peak displacements of the CFRP strengthened beams were consistently less than the static values. However, peak bending load increases ranging from 200% to 300% were observed when compared to the corresponding static values. The author postulated that this shows that a beam has a fixed energy absorption capacity for a given load rate, governed by the peak bending load and limited by displacement. The observed failure mechanism for all the CFRP strengthened beams intitiated by combined flexure and shear failure in the concrete with intermediate crack (IC) induced interfacial debonding of the FRP.

Erki & Meier (1999) studied the dynamic behaviour of two 8 m reinforced concrete beams strengthened for flexure with CFRP. Impulse loading was induced by raising one end of the beam and dropping it on a damping unit consisting of a shock absorber. The strain rate of the impulse load ranged from an average of 0.057 s^{-1} to a maximum of over 0.8 s^{-1}. A comparison was made with test data for beams with identical geometry strengthened with steel plates. Erki & Meier (1999) concluded that although the CFRP strengthened beams performed well under impact, the energy absorption capacity of the steel plated beams could not be replicated. The failure of the FRP in the beams occurred by IC debonding and tensile rupture.

White et al (2001) investigated the effects of strain rate on the behaviour of CFRP strengthened RC beams. The RC beams were tested in four-point bending under four different loading schemes, with stroke rates ranging from 0.0167mm/s (slow) to 36mm/s (fast). The slow and fast stroke rates induced maximum strain rates of 10^{-6} s^{-1} and 10^{-3} s^{-1}, respectively.

Based on the review of the experimental data, White *et al* (2001) concluded that:

(i) Strengthening with CFRP will increase the flexural capacity and stiffness of the RC beam, but will result in a reduction in energy absorption capacity and ductility.

(ii) The magnitude of these changes is dependent on the amount of CFRP reinforcement, steel reinforcement, and the mode of failure.

(iii) For CFRP strengthened beams with similar failure modes, rapidly strained beams (10^{-3} s^{-1}) show a 5% increase in flexural capacity, stiffness, and energy absorption over similar beams loaded slowly (10^{-6} s^{-1}).

Tang (2002) investigated the dynamic response of plain and reinforced concrete beams strengthened with FRP. Beams, strengthened with either AFRP or CFRP, were subjected to low velocity impact with the application of the drop-weight impact test method. Two loading schemes were employed in the study. For the first scheme, the drop height was maintained for each test. In the second scheme, the drop height was varied for each test. Results show that although the post-impact residual stiffness of the strengthened beam was two to three times that of the unstrengthened beam, the

maximum deflection decreased by as much as 40%. Furthermore, a comparison with the static load test results showed that the post-impact ultimate deflection and crack widths of the FRP strengthened beam were lower. However, the maximum reaction force was found to be three to four times larger than the static load case. Observed failure modes included FRP rupture and shear failure of the concrete depending on the type of FRP composite.

Tang & Saadatmanesh (2003) examined the impact effects on RC beams strengthened with FRP. Two types of composite laminates were considered in the experimental study, namely carbon and Kevlar. The laminates were bonded on the top and bottom surfaces of the beam specimens. Five beams were tested using the drop weight impact test method. The drop weight was repeatedly dropped from heights varying from 1.52m to 3.96m. Results show that the reaction force of the beam varied with the thickness and weight of the laminate for the same impact energy. Furthermore, it was shown that FRP laminates increases shear strength, reduces crack widths and deflections. The observed failure mechanism for all the FRP strengthened beams was generally shear failure accompanied by crushing of concrete on the top of the beam with intermediate crack (IC) induced interfacial debonding of the FRP.

2.4 Modelling techniques for impact response

Abrate (1991, 1994, 1997, 1998) presented a number of comprehensive literature reviews on the dynamic response of structures under impact loading. Abrate has shown that various modelling techniques are available for investigating impact dynamics. These include energy-balance models, spring-mass models and complete models. Current research on analytical tools to model the dynamic response of RC beams strengthened with FRP, based on the spring-mass and complete models, is shown in Table 1. This section presents a review of the various models and an assessment of their performance.

Table 1: Summary of analysis tools developed for impact on FRP strengthened RC beams

Reference	Spring-mass models	Complete models	
		Analytical Models	Finite Element Models
Jerome (1996)	•		•
Erki & Meier (1999)		•	
White et al (2001)		•	
Tang (2002)	•		
Hamed & Rabinovitch (2005, 2007)		•	
Mohammed (2011)			•

2.4.1 Spring-mass models

Spring-mass models provide a simple means for the accurate prediction of the dynamic response and contact force histories for certain impact types encountered during tests on small size specimens (Abrate, 1998). The spring-mass model assumes that the structure behaves quasi-statically. The two-degree-of freedom (TDOF) model, as shown in Figure 12, is the most complete spring mass model for impacts on composite plates and beams since it accounts for the mass of the target and local indentation in the contact zone (Abrate, 2011). The TDOF model consists of three springs, representing the linear stiffness of the structure K_{bs}, the nonlinear membrane stiffness K_m, and the nonlinear contact stiffness k. The effective mass of the structure is given by M_2, and the mass of the projectile by M_1. The equations of motion for the two-mass system derived from force equilibrium are given by (Abrate, 1998):

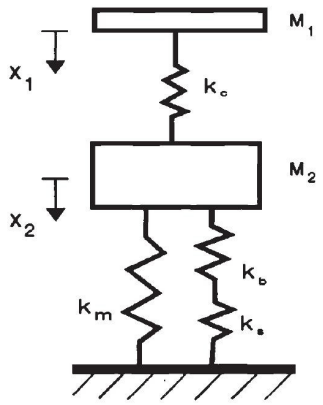

Figure 12: Two-degree-of-freedom model (Abrate, 1998)

$$M_1\ddot{x}_1 + P = 0 \tag{2.18}$$

$$M_2\ddot{x}_2 + K_{bs}x_2 + K_m x_2^3 - P = 0 \qquad (2.19)$$

where P is the nonlinear contact force governed by the indentation $x_1 - x_2$. Spring-mass models developed by Jerome (1996) and Tang (2002) for the dynamic response of FRP strengthened beams under impact are discussed below.

Jerome (1996) idealised the FRP strengthened beam as a single-degree-of-freedom (SDOF) system. The drop-weight impactor used in the author's experimental study was idealised as half-sine impulses. This approach was used to describe the displacement-time response for the FRP strengthened beam under impact. The dynamic response for the half-sine impulse comprises two phases as shown in Figure 13. The first corresponds to the forced-vibration phase in the interval during which the load acts.

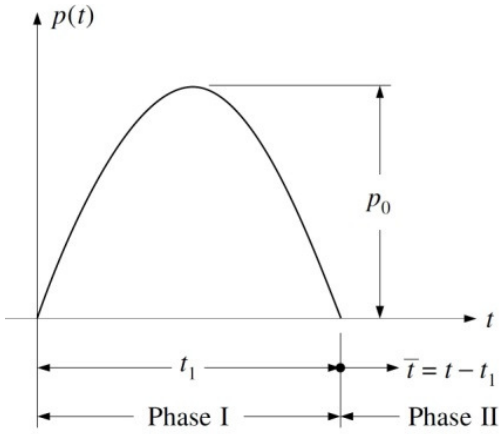

Figure 13: Half-sine-wave impulse (Clough & Penzien, 2003)

This is followed by the second phase corresponding to the free-vibration. For Phase I, the general solution for the transient and steady state terms under simple harmonic loading is given by (Jerome, 1996):

$$x(t) = \frac{p_0}{k_e}\left(\frac{1}{1-\beta^2}\right)[\sin\bar{\omega}t - \beta\sin\omega t] \qquad (2.20)$$

with the free-vibration response of Phase II given by:

$$x(\bar{t}) = -\frac{p_0}{k_e}\left(\frac{\beta}{1-\beta^2}\right)\left[\sin\frac{\pi}{\beta}\cos\omega\,\bar{t} + \left(1+\cos\frac{\pi}{\beta}\right)\sin\omega\bar{t}\right] \qquad (2.21)$$

where p_0 is the amplitude of the half-sine pulse, ω is the natural frequency, $\overline{\omega}$ is the applied loading frequency, k_e is the equivalent stiffness of the system, and β is the ratio of the applied loading frequency to natural frequency.

Although the model yielded comparable results up to beam failure when compared to the drop-weight test data, the displacements after the peak load amplitude in Phase I failure where generally overpredicted. This may be related to inherent limitations of the analytical model. There is no provision in the model for the strain-rate effect, internal damping and post-cracking dynamic stiffness in the RC beam. Furthermore, the viscoelastic characteristics of the FRP adhesive were not considered.

Tang (2002) used a TDOF model as shown in Figure 14 in a semi-empirical approach to predict the force history of the FRP strengthened beam under impact. The contact force F and the contact duration T_c is derived as follows (Tang, 2002):

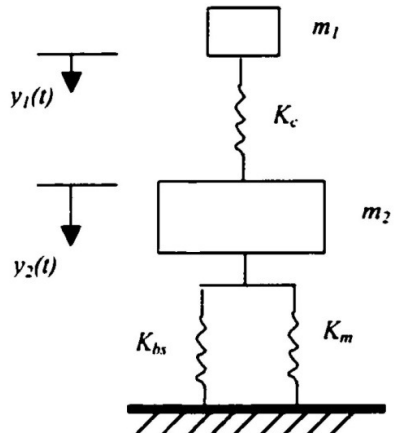

Figure 14: Two-degree-of-freedom model for FRP strengthened beam under impact (Tang, 2002)

$$m_1 \frac{d^2 y_1}{dt^2} + F = 0 \tag{2.22}$$

$$m_2 \frac{d^2 y_1}{dt^2} + K_{bs} y_2 + K_m y_2^3 - F = 0 \tag{2.23}$$

The initial conditions expressed at $t = 0$ (before contact) are

$$\frac{dy_1}{dt}(0) = V; \quad y_1(0) = y_2(0) = 0 \tag{2.24}$$

where V is the initial velocity of the impactor before the onset of impact. If the impactor indentation and geometrical nonlinearity of the system are negligible, the model may be simplified to a single-degree-of-freedom system with the following equation of motion

$$m_1 \frac{d^2 y_1}{dt^2} + K_{bs} y_2 = 0 \tag{2.25}$$

Further simplification is introduced, by neglecting the effective mass of the structure and assuming that structure and impactor move together on contact, to derive the general solution for equation (2.25).

$$y = \frac{V}{\omega} \sin \omega t \tag{2.26}$$

$$where\ \omega = \sqrt{\frac{K_{bs}}{m_1}} \tag{2.27}$$

Because the contact force F is equal to the force in the linear spring K_{bs}, the contact force history can be expressed as

$$F = K_{bs} y = V\sqrt{K_{bs} m_1} \sin(\omega t) \tag{2.28}$$

for $\omega t < \pi$. Contact separation occurs between the beam and the impactor for $\omega t = \pi$. From equation (2.30), the contact duration T_c is given by

$$T_c = \pi \sqrt{\frac{m_1}{K_{bs}}} \tag{2.29}$$

Parameters m_1 and m_2 are the masses of the impactor and beam, respectively; y_1 and y_2 are the displacements of the impactor and beam, respectively; F is the contact force between impactor and beam; K_{bs} is the bending-shear stiffness of the beam; and

K_m is the membrane stiffness. Equation (2.28) is based on the assumption that the stiffness of the RC beam remains constant during the impact effect. The actual beam response is given by stiffness reduction as cracks propagate under impact. Tang (2002) modified Equation (2.28) with a constant γ, based on drop-weight test results, to account for the effects of reduced stiffness. Equation (2.28) may be rewritten as:

$$F = K_{bs}y = \frac{V\sqrt{K_{bs}m_1}}{\gamma}\sin(\omega t) \tag{2.30}$$

where γ was calculated as the average ratio of the measured first impact force for the test beams and the impact force given by equation (2.28). Although the model does not account for the internal damping of the RC beam and the viscoelastic characteristics of the FRP adhesive, equation (2.30) yielded results consistent with the test data for the first impact event. The mean value for the ratio of impact force determined from equation (2.30) to measured beam reaction force was 1.002 with a standard deviation of 0.005.

2.4.2 Complete models

In the complete model, the dynamic behaviour of the entire structure is described accurately as opposed to the preceding model (Abrate, 1998). The structure is modelled using either beam, plate, or shell theory depending on the structural system. Once an appropriate theory is selected, and depending on the geometry and boundary conditions of the structural system, the transient response is determined using analytical models in the form of either a closed form solution or a variational approximation method. Alternatively, a finite element approach may be used (Abrate, 2011).

The differential equations for the equations of motion in matrix form is given by (Abrate, 2011):

$$[M]\{\ddot{X}\} + [K]\{X\} = \{F\} \tag{2.31}$$

where $\{F\}$ is an external force vector with components that are nonlinear functions of the displacements, $\{X\}$ is a vector with n degrees of freedom, and $[M]$ and $[K]$ are n x n matrices. Complete models developed by Jerome (1996), Erki & Meier (1999), White et al (2001), Hamed & Rabinovitch (2005), Hamed & Rabinovitch (2007), and Mohammed (2011) for the dynamic response of FRP strengthened beams under impact are discussed below.

In addition to spring-mass models, Jerome (1996) also employed the finite element approach using the Automatic, Dynamic, Incremental, Nonlinear Analysis (ADINA) code to study the dynamic behaviour of the FRP strengthened beams. Two finite element models were developed and analysed. A simply supported plain concrete beam tested with a midspan impact drop height of 50.8mm was simulated in one analysis. The other analysis simulated a midspan impact drop height of 457.2mm to a simply supported plain concrete beam strengthened with FRP on the tension face. Symmetry allowed one half of each beam to be modelled as shown in Figure 15.

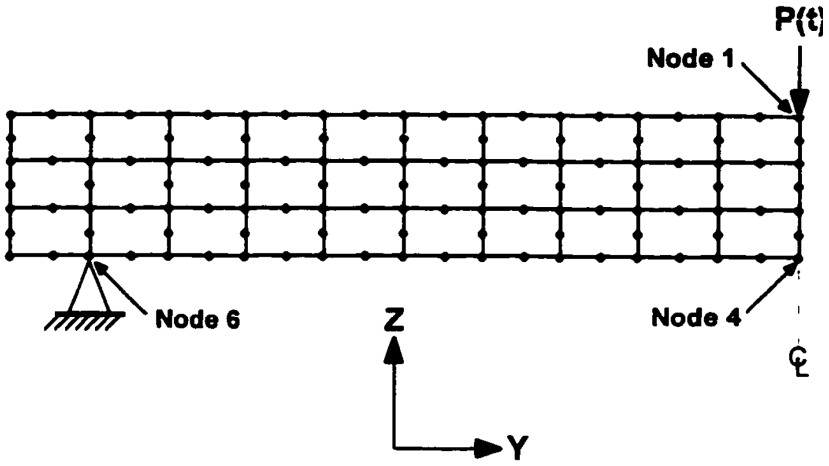

Figure 15: FEM discretization for one-half of test beam (Jerome, 1996)

Concrete was modelled using 30 two dimensional elements. Each isoparametric displacement-based finite element comprised an eight node configuration. At the midpoint plane of symmetry, displacement of nodes were constrained in the direction perpendicular to the plane. Displacement of the node at the simple support was constrained in the vertical direction. All other nodes were considered free in both vertical and horizontal directions. FRP on the tension face of the beam was modelled using 10 three-node truss elements

A linear elastic material model was employed for the FRP. Perfect bond was assumed between the FRP and concrete surface as the epoxy adhesive was not considered in the model. A hypo-elastic material model was used to model the behaviour of the concrete beam. This model incorporates three aspects, namely:

i) Non-linear stress-strain relation with strain softening
ii) Failure envelopes defining tensile cracking and crushing in compression
iii) Post-cracking and crushing behaviour of the concrete

The results for the FRP strengthened beam showed that the ADINA pre and post failure displacement-time behaviour compared favourably with the experimental data as shown in Figure 16. Furthermore, the predicted initiation and location of flexural and shear cracks compared well to the experimental results. However, the FRP failure behaviour was not captured owing to the absence of the FRP bond interface definition in the model.

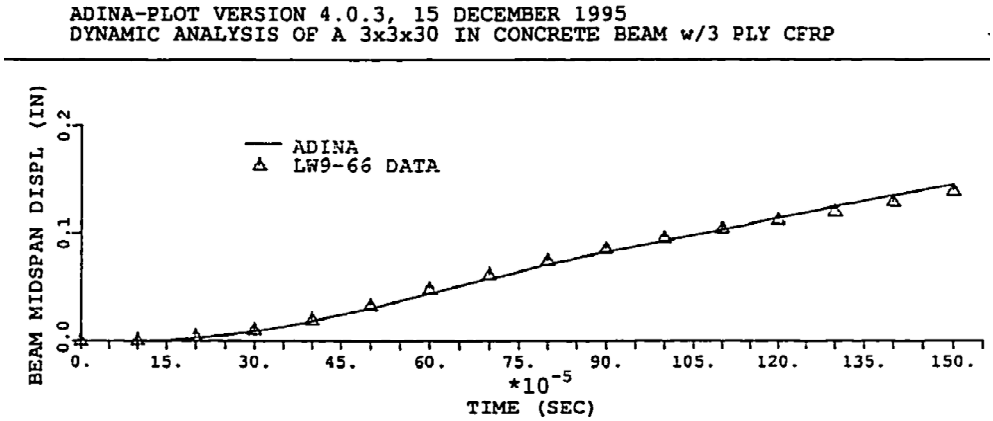

Figure 16: Comparison of experimental and ADINA displacement-time behaviour for FRP strengthened beam (Jerome, 1996)

Erki & Meier (1999) used an equivalent beam approach in formulating the equation of motion for beam flexure to describe the dynamic behaviour of FRP strengthened beams under impact. This approach was selected to replicate the test method used by the authors in the experimental phase of the study where the test beams were raised up one end of the beams and dropped on the support. The displacement equation for the dynamic response of a prismatic beam is given by (Erki & Meier, 1999):

$$v(x,t) = \frac{2\dot{v}_{l0}}{\pi}\left(\frac{1}{w_1}\sin\frac{\pi x}{L}\sin w_1 t - \frac{1}{2w_2}\sin\frac{2\pi x}{L}\sin w_2 t + \cdots\frac{1}{nw_n}\sin\frac{n\pi x}{L}\right) \quad (2.32)$$

where x is the location from the pinned end along the beam length at time t, $\dot{v}_{l0}$ is the velocity of the tip of the beam at time of impact, and w_n is the vibrational frequency for the nth mode. The model does not account for damping of the system, nor for post-cracking stiffness of the RC beam that varies with time and location. Furthermore, the deformability and viscoelastic characteristics of the FRP adhesive were not considered.

White et al (2001) employed an finite element model using a layered finite element technique to predict the moment-curvature response of FRP strengthened RC beams. These beams were tested in four-point bending under stroke rates inducing strain rates of 10^{-6} s^{-1} and 10^{-3} s^{-1}, as previously discussed in section 2.3.3. The use of strain rate dependent constitutive material models was limited to two aspects, namely confined concrete in compression and steel reinforcement in tension. These include a non-linear concrete material model with strain softening and bilinear material properties for the steel reinforcement. The author postulated that the material models for FRP in tension, concrete in tension and steel reinforcement in compression were linear and not dependent on induced strain rate. To simplify the calculations, some assumptions were made. These include perfect bond between elements, linear strain distribution, small deformations, and negligible section mass. Furthermore, the FRP adhesive layer was not considered in the model.

The components of the FRP strengthened beams were modelled as discrete elements. The concrete section was divided into several layers whereas the steel reinforcement and FRP was assigned one layer each. Having determined the section properties and forces of each layer, using the appropriate material model, the moment-curvature response for each test beam was determined using an iterative approach.

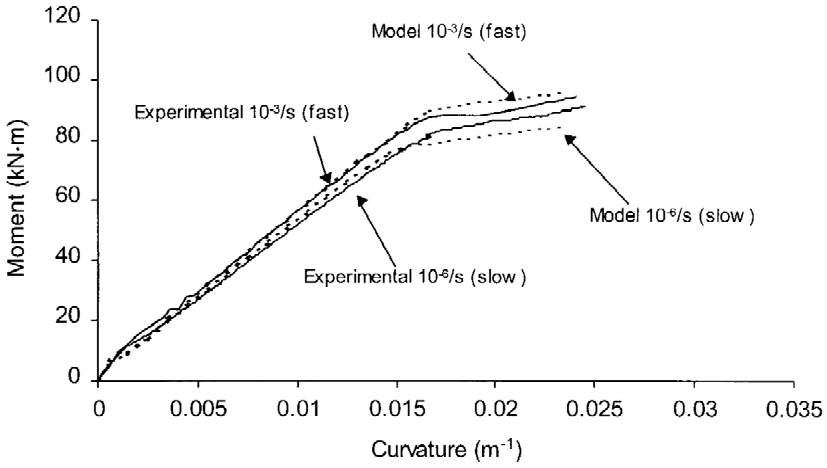

Figure 17: Comparison of experimental and model moment-curvature behaviour for FRP strengthened beam (White et al, 2001)

The results for the FRP strengthened beam showed that the model moment-curvature behaviour compared favourably with the experimental data as shown in Figure 17.

Hamed & Rabinovitch (2005) addressed the limitations of the aforesaid approaches in the development of a closed-form high order analytical solution for the analysis of RC beam strengthened with FRP. The model accounts for the shear and vertical deformability of the FRP adhesive layer and its influence on the dynamic beaviour of the beam.

The model employs dynamic equilibrium and compatibility requirements between the structural components, i.e. RC beam, FRP laminate and the adhesive layer. The material model for the RC beam element was described using Bernoulli-Euler beam theory with small deformations. Lamination theory was used to model the FRP laminate. A two-dimensional linear elastic continuum with negligible in-plane longitudinal stiffness was assumed for the adhesive layer.

The equations of motion and the dynamic boundary and continuity conditions were derived using Hamilton's variational principle given by (Hamed & Rabinovitch, 2005):

$$\delta \int_{t_0}^{t_1} (T - \Pi) dt = 0 \tag{2.33}$$

where T is the kinetic energy; $\Pi = U + V$ is the total potential energy, which includes the strain energy U, and the potential of the external loads V; δ is the variational operator, and t is time. The resulting coupled partial differential equations were converted into a set of ordinary differential equations which are solved in every time step by the direct application of the Newmark time integration method. As an example of this approach, the vertical acceleration and velocity fields of the RC beam at the jth time step ($t = t_{j)}$ is given by (Hamed & Rabinovitch, 2005):

$$\ddot{w}_c(x)_j = \frac{w_c(x)_j - w_c(x)_{j-1} - \Delta t \dot{w}_c(x)_{j-1} - \frac{1}{2}\Delta t^2 \ddot{w}_c(x)_{j-1} + \beta \Delta t^2 \ddot{w}_c(x)_{j-1}}{\beta \Delta t^2} \tag{2.34}$$

$$\dot{w}_c(x)_j = \frac{(\beta \Delta t - \gamma)\dot{w}_c(x)_{j-1} + \gamma[w_c(x)_j - w_c(x)_{j-1}] + \left(\beta \Delta t^2 - \frac{1}{2}\gamma \Delta t^2\right)\ddot{w}_c(x)_{j-1}}{\beta \Delta t} \tag{2.35}$$

where $\ddot{w}_c(x)_j$, $\dot{w}_c(x)_j$ and $w_c(x)_j$ are the acceleration, velocity, and displacement fields of the RC beam, respectively, at the jth time step; β and γ are parameters that control the stability and accuracy of the algorithm.

Although this theoretical approach included the shear and vertical deformability of the FRP adhesive layer, the damping characteristics of the strengthened beam and the viscoelastic behaviour of the adhesive material was not accounted for.

In later studies by Hamed & Rabinovitch (2007), this limitation was addressed in updating the model by adopting the Kelvin-Voigt approach to describe the viscoelastic constitutive relations of the adhesive by (Hamed & Rabinovitch, 2007):

$$\sigma_{zz}^a(x, z_a, t) = E_a[\varepsilon_{zz}^a(x, z_a, t) + a_{1\sigma}^a \dot{\varepsilon}_{zz}^a(x, z_a, t)] \tag{2.36}$$

$$\tau_{xz}^a(x, z_a, t) = G_a[\gamma_{xz}^a(x, z_a, t) + a_{1\tau}^a \dot{\gamma}_{xz}^a(x, z_a, t)] \tag{2.37}$$

where E_a and G_a are the modulus of elasticity and shear modulus of the adhesive, respectively; $\dot{\varepsilon}_{zz}^a$ and $\dot{\gamma}_{xz}^a$ are the vertical normal strain rate and the shear angle rate,

respectively; and $a_{1\sigma}^{a}$ and $a_{1\tau}^{a}$ are viscous constants that represent the material loss factors.

Similarly, the Kelvin-Voigt approach was used to model the internal damping of the RC beam in formulating the stress-strain constitutive relation of the concrete material given by (Hamed & Rabinovitch, 2007):

$$\sigma_{zz}^{c}(x, z_c, t) = E_c[\varepsilon_{xx}^{c}(x, z_c, t) + a_1^{c}(t)\dot{\varepsilon}_{xx}^{c}(x, z_c, t)] \tag{2.38}$$

where E_c is the modulus of elasticity of the concrete, $\dot{\varepsilon}_{xx}^{c}$ is the strain rate, and $a_1^{c}(t)$ is the proportionality constant.

Mohammed (2011) developed a finite element model to analyse the dynamic response of FRP strengthned RC beams under impact loading. ANSYS, a nonlinear finite element programme, was used as to generate the mesh and geometry of the beams. LS-PrePost software programme was employed to define the material models. With all input parameters defined, the LS-DYNA finite element software was used to execute the nonlinear explicit finite element analysis. The model was developed and validated based on experimental studies conducted by other researchers.

Impact loading for each beam was applied at midspan using a 400kg drop weight released from heights of 600mm and 1200mm. Three beams, with varying compressive and tensile steel reinforcement ratios, were selected for modelling. The FRP layout, steel reinforcement and beam geometry of the beams is shown Figure 18.

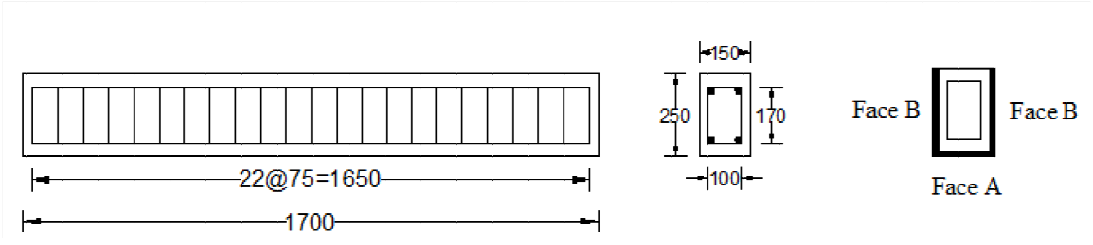

Figure 18: Geometry, FRP layout and steel reinforcement for FE beam models (Mohammed, 2011)

The concrete section and drop weight hammer was modelled as three dimensional eight-node brick elements. Steel reinforcement bars and FRP was modelled as three dimensional spar elements and four-node membrane elements, respectively. Nodes for all elements had three degrees of freedom. The FRP adhesive layer was not considered in the model.

A visco-plasticity material model was used to model the strain rate dependent plasticity behaviour of the concrete beam. The behaviour of steel reinforcement was represented using an elasto-plastic material model integrating both strain rate effects and kinematic hardening rules. An orthotropic material model, based on a brittle failure mode criterion, was used to model the FRP. The model was validated based on experimental studies by Fujikake et al (2009) on the impact response of RC beams. The results for the non-FRP strengthened beams showed that the model peak impact force response compared favourably with the experimental data as shown in Figure 19.

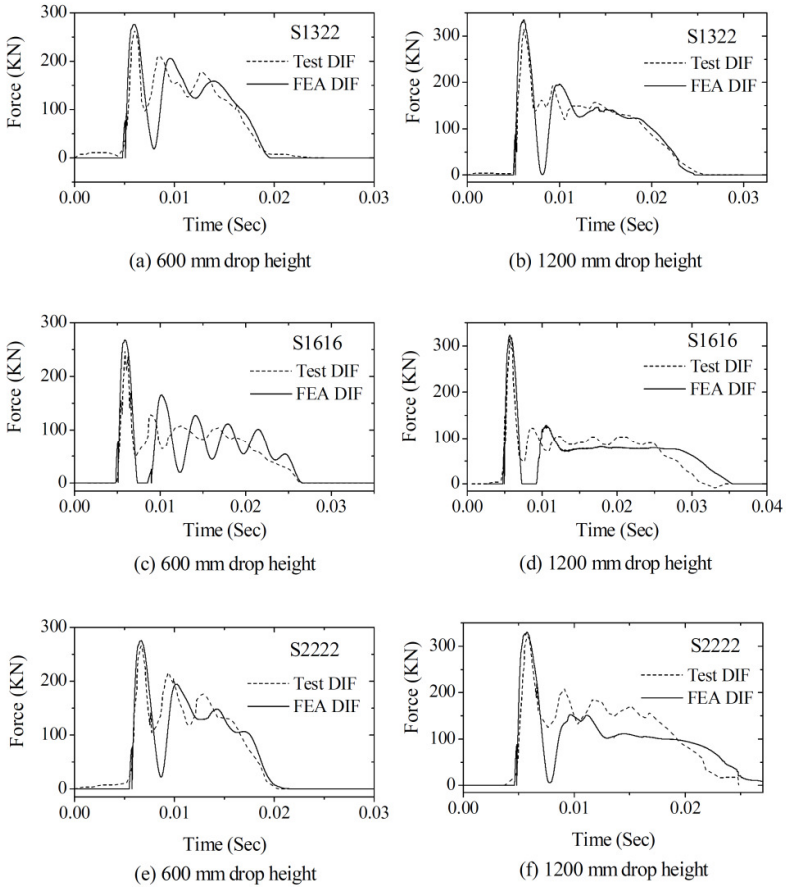

Figure 19: Impact force vs. time history for various RC beams (Mohammed, 2011)

The results of the finite element analysis of the FRP U-wrapped RC beams illustrated the non-linear relationship between FRP energy absorption capacity and drop weight height as shown in Figure 20.

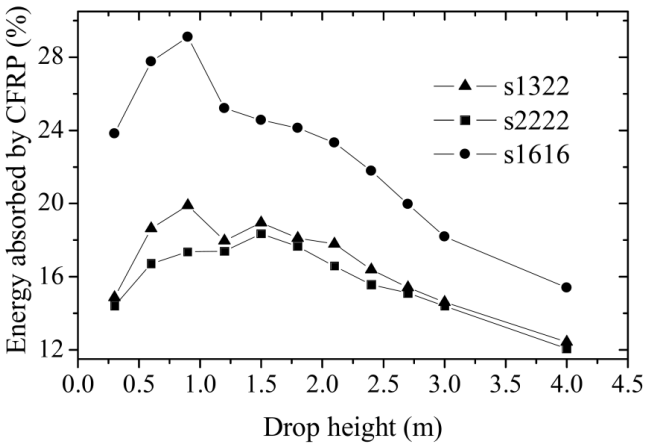

Figure 20: Drop weight height vs. FRP energy absorption (Mohammed, 2011)

The steel reinforcement ratio for beam S1161 was 1.26%, whereas the ratio for beam S1322 and S2222 was 2.46%. Therefore, it was shown that the energy absorption capacity of the FRP was governed by the tensile steel reinforcement ratio. Furthermore, the results showed that FRP strengthening using the U-wrap technique increased the beam stiffness, confined the development of flexural cracks, and changed the overall beam failure mode from flexure to local concrete crushing in the impact zone.

This study shows that the use of a finite element analysis to model the dynamic response of FRP strengthened beams under impact loading is viable. However, since the FRP bond interface was not defined in the model, the FRP failure behaviour was not captured in full.

2.5 Summary

The static behaviour of FRP strengthened RC beams has been the subject of extensive research. Furthermore, almost all low-velocity impact studies to date has focused on pure composite structures (Tang & Saadatmanesh, 2003). However, the dynamic

behaviour of FRP strengthened RC beam elements remains unclear. Limited experimental studies are available that are focused on the response of FRP strengthened RC beams subjected to low velocity impact events. Furthermore, many of the tools developed in these studies yielded results that were inconsistent with the test data.

Experimental impact studies on FRP strengthened beams by Jerome (1996) and Erki & Meier (1999) has shown that the predominant failure mode is combined shear and flexure with IC dedonding of the FRP. Therefore the integration of suitable FRP bond interface models is essential to capture the full-spectrum response of the system. The models developed by Jerome (1996), Erki & Meier (1999), White et al (2001) and Mohammed (2011) assume a perfect bond between FRP and concrete. These models were therefore unable to model the FRP IC debonding failure mechanism and the contribution of the FRP bond interface to the overall response of the strengthened beam.

In dynamic analyses involving impact, the rate dependent behaviour of the constituent materials at high strain rates is an important consideration as this may differ substantially when compared to static loading conditions. Of the aforementioned models, only Mohammed (2011) incorporated load rate effects in the concrete material model.

In an attempt to address the limitations of existing models reported in the literature, this study will focus on the development of a FE model capable of simulating the dynamic response of FRP strengthened beams under low velocity impacts, based on:

a) appropriate load-rate dependent constitutive material models for concrete; and
b) a FRP interfacial bond behaviour model.

In Chapter 3, the theoretical framework for the development of the FE model is presented. Structural dynamic theories, constitutive material models, and FRP bond interface models considered for model implementation are described in this chapter.

3 FE MODELLING OF DYNAMIC RESPONSE OF REINFORCED CONCRETE

In this study, the dynamic response of FRP strengthened RC beams subjected to impact loading has been simulated in the finite element program Abaqus/Explicit version 6.10. The finite element method (FEM) is a numerical technique used to obtain approximate solutions to a wide range of boundary value engineering problems that are to complex and time intensive to resolve using classical continuum methods (Cook et al, 1989; Hutton, 2004). The boundary value problem is one in which a solution is sought within the domain of the body where the dependent variables must satisfy a differential equation throughout a known domain of independent variables and satisfy boundary conditions of the domain (Hutton, 2004).

Boundary value problems, for which the finite element method is well suited, can be classified into three major categories. These categories are equilibrium problems, eigenvalue problems and propagation problems. Equilibrium problems, such as the static analysis of bridges, are related to the determination of steady-state displacements or stress distributions of static systems. The eigenvalue problem is an extension of the equilibrium problem whereby critical values of certain parameters, such as natural frequencies and modes, are also sought. In contrast, propagation problems are associated with time-dependent transient problems where the response of a body under a time-varying force is determined. A typical example of the propagation problem is the dynamic analysis of the FRP strengthened beam under impact loading (Rao, 2005).

This chapter provides an overview of the salient features of the dynamic analysis algorithm employed in Abaqus/Explicit. Furthermore, an overview of available material models in Abaqus/Explicit for concrete, steel reinforcement and FRP bond interface is presented. The theoretical framework of selected material models for concrete, considered for implementation in the FE model, to define the material behaviour in the Abaqus/Explicit material model is also discussed.

3.1 Explicit direct-integration finite element analysis

The dynamic response of a given structural system can be obtained by solving the second order differential equations for the equations of motion in matrix form given by (Abrate, 2011):

$$M\ddot{u} + C\dot{u} + Ku = F \tag{3.1}$$

where F is a general (non-harmonic) forcing function; $\ddot{u}$ is a acceleration vector, $\dot{u}$ is a velocity vector, u is a displacement vector; and M, C and K are n x n matrices for mass, damping and stiffness respectively. The direct integration method is a widely used method to solve the governing equation (3.1) for structural systems subjected to transient excitations. Direct integration employs the finite difference method for time stepping to solve the governing equation using either the implicit or explicit integration operator. Explicit direct-integration methods are computationally efficient techniques able to simulate a wide variety of dynamic systems involving blast and impact (Liu & Quek, 2003). Therefore, this method is of interest in the current study.

Implicit direct-integration methods are computationally expensive that requires the formation and inversion of global stiffness and mass matrices. Furthermore, nonlinear equilibrium equations must be solved at each time increment. Conversely, global stiffness and mass matrices need not be formed in the case of explicit direct-integration methods since. The computation cost is therefore considerably less compared to implicit methods. However, the method is conditionally stable as the size of the time step has to be less than a certain critical time step related to the time required for a stress wave to cross the smallest element dimension in the model. Explicit methods are well suited for modelling nonlinear and contact events, such as impact loading to FRP strengthened beams (Petyt, 2010; Liu & Quek, 2003; Abaqus user's manual, 2010).

Abaqus/Explicit uses the central difference algorithm, characteristic of explicit methods in general, for the direct integration of the governing equations of motion. The solution is determined based on historical displacement, velocity and acceleration quantities that are known at the beginning of the time increment.

3.2 Time increment and stability limit

The central difference algorithm employed in explicit dynamic analysis is conditionally stable. The stability limit of the algorithm is expressed in terms of the maximum frequency of the system by (Abaqus, 2010):

$$\Delta t = \frac{2}{\omega_{max}} \tag{3.2}$$

Abaqus/Explicit employs two methods to determine the maximum frequency, namely the global and element-by-element estimation algorithm. The global estimation algorithm is used to define the maximum frequency of the entire system. In cases where material damping and nonisotropic elastic materials are included in the model, the maximum frequency is instead determined using the element-by-element algorithm. The stability limit is then determined based on the shortest time interval required for dilatational wave front to pass through the mesh:

$$\Delta t = min\left(\frac{L_e}{\mathrm{c}_d}\right) \tag{3.3}$$

where L_e is the characteristic element dimension and c_d is the effective dilatational wave speed of the material. The definition of the effective dilatational wave speed is based on effective hypoelastic material moduli from the material's constitutive behaviour:

$$\mathrm{c}_d = \sqrt{\frac{\hat{\lambda} + 2\hat{\mu}}{\rho}} \tag{3.4}$$

where $2\hat{\mu}$ and $\hat{\lambda}$ are the effective Lamé's constants, and ρ is the material density.

One of the methods available in Abaqus/Explicit to improve computational efficiency when the time increment size in an FE model is governed by very small elements is mass scaling.

3.2.1 Mass scaling

Dynamic models are generally complex containing a few very small elements. From Equation (3.3), this results in Abaqus/Explicit using a small time increment to integrate the entire model. In this case, computational efficiency may be improved by using the mass scaling technique available in Abaqus/Explicit. The stable time increment (stability limit) is increased significantly by scaling the masses of these controlling elements.

3.3 Modelling of constituent materials in Abaqus/Explicit

In this study, the analysis of the dynamic behaviour of FRP strengthened beams under impact loading will be undertaken using the Abaqus finite element software programme. Details of available material models for concrete and steel reinforcement, as well as FRP bond interface models considered for implementation in the Abaqus FE model is presented in the following sections.

3.3.1 Plain concrete

Three concrete constitutive material models are available in Abaqus. These are the brittle cracking, inelastic smeared crack, and damaged plasticity models (Abaqus, 2010):

The brittle cracking model is only available in Abaqus/Explicit. It is intended for cases where the material behaviour is governed by tensile cracking and compression behaviour is considered linear elastic. Post-cracked tension softening behaviour is defined using a fracture energy criterion and brittle behaviour is simulated using a smeared crack model.

This model is appropriate for scenarios where the concrete element is subjected to monotonic loadings under fairly low confining pressures. Associated flow and an isotropic hardening yield surface is used when the stress is dominantly compressive, whereas a crack detection plasticity surface is used to determine the onset of cracking

when the stress is predominantly tensile. A damaged elasticity approach is then used to simulate the post-cracking behaviour of the concrete.

The damaged plasticity model is available in both Abaqus/Explicit and Abaqus/Implicit. The model is intended for the analysis of concrete elements under dynamic or cyclic loading. Therefore, this model is of interest in the current study.

Concrete Damaged Plasticity model

The concrete damaged plasticity (CDP) model simulates the effects of irreversible damage related to the failure mechanisms associated with concrete under low confining pressures. These effects are (Abaqus, 2010):

i) Rate dependency, especially an increase in peak strength with strain rate
ii) Different yield strengths in tension and compression
iii) Softening behaviour in tension
iv) Different degradation of elastic stiffness in tension and compression
v) Stiffness recovery effects during cyclic loading

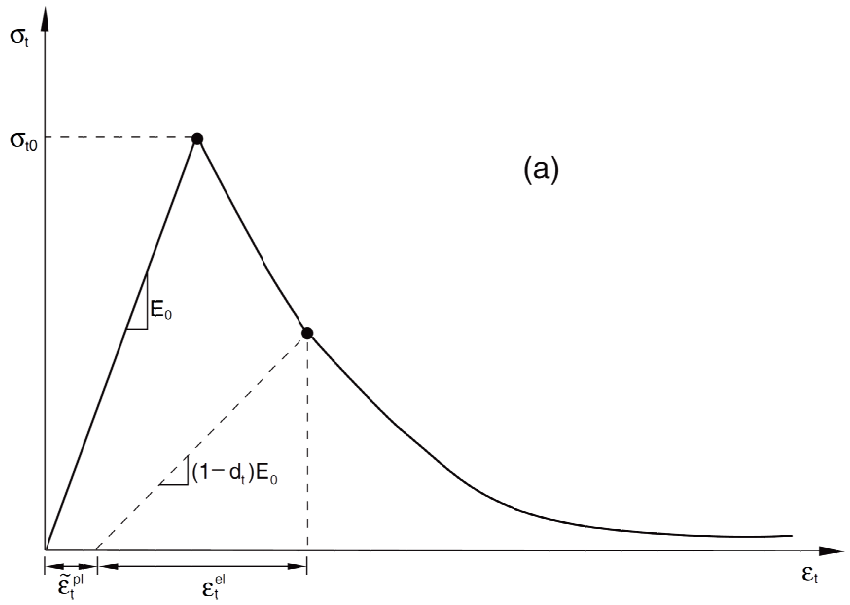

Figure 21: Stress-strain response of concrete under uniaxial tension (Abaqus User's Manual, 2010)

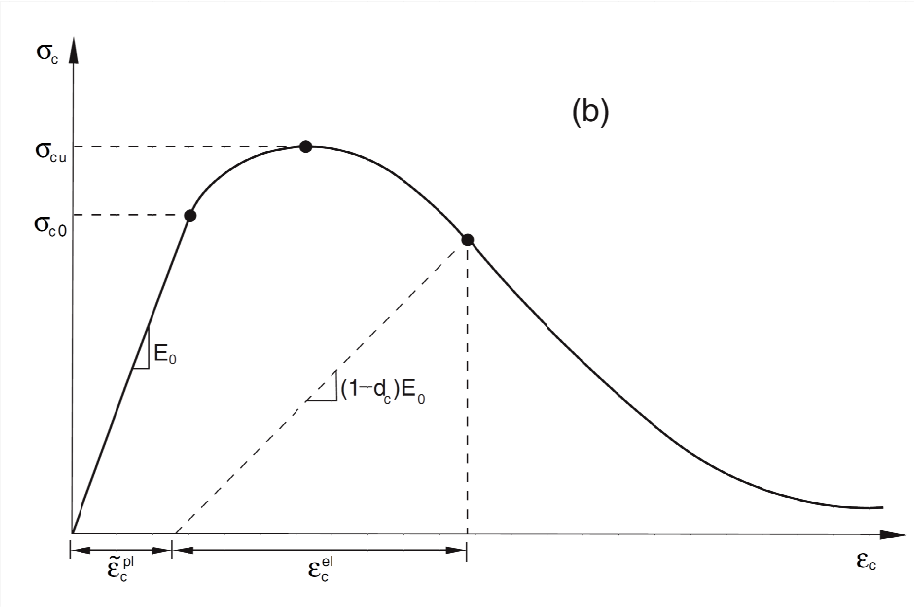

Figure 22: Stress-strain response of concrete under uniaxial compression (Abaqus User's Manual, 2010)

The differing damage and stiffness degradation of concrete for uniaxial loading in tension and compression is shown in Figures 21 and 22 respectively. The uniaxial tension response is linear elastic until the failure stress of σ_{t0} is attained. Thereafter, the degradation is governed by the microcracks formation leading to a softening stress-strain response. On the other hand, the uniaxial compression plastic response beyond the ultimate stress σ_{cu} is characterized by stress hardening followed by strain softening.

The uniaxial stress-strain curves are converted into stress versus plastic strain curves expressed as

$$\sigma_t = \sigma_t\left(\tilde{\varepsilon}_t^{pl}, \dot{\tilde{\varepsilon}}_t^{pl}, \theta, f_i\right) \tag{3.5}$$

$$\sigma_c = \sigma_c\left(\tilde{\varepsilon}_c^{pl}, \dot{\tilde{\varepsilon}}_c^{pl}, \theta, f_i\right) \tag{3.6}$$

Where the subscript t and c refer to tension and compression, respectively; $\dot{\tilde{\varepsilon}}_t^{pl}$ and $\dot{\tilde{\varepsilon}}_c^{pl}$ are the equivalent plastic strain rates, $\tilde{\varepsilon}_t^{pl}$ and $\tilde{\varepsilon}_c^{pl}$ are the equivalent plastic strains, θ is the temperature, and f_i the predefined field variable. The two independent damage variables, d_t and d_c, are given by

$$d_t = d_t\left(\tilde{\varepsilon}_t^{pl}, \dot{\tilde{\varepsilon}}_t^{pl}, \theta, f_i\right), \quad (0 \le d_t \le 1) \tag{3.7}$$

$$d_c = d_c\left(\tilde{\varepsilon}_c^{pl}, \dot{\tilde{\varepsilon}}_c^{pl}, \theta, f_i\right), \quad (0 \le d_c \le 1) \tag{3.8}$$

The damage variables describe the state of material damage where a value of zero and one represents the undamaged and damaged material respectively. With an initial (undamaged) elastic stiffness of the material E_0, the stress-strain behaviour under uniaxial tension and compression loading are, respectively

$$\sigma_t = (1 - d_t)\, E_0\left(1 - \tilde{\varepsilon}_t^{pl}\right) \tag{3.9}$$

$$\sigma_c = (1 - d_c)\, E_0\left(1 - \tilde{\varepsilon}_c^{pl}\right) \tag{3.10}$$

The damaged plasticity models use a non-associated plastic flow rule where the flow potential G is the Drucker-Prager hyperbolic function given by

$$G = \sqrt{(\varepsilon \sigma_{t0}\, tan\, \psi)^2 + \bar{q}^2} - \tilde{p} \tan \psi \tag{3.11}$$

where ψ is the dilation angle measured in the $p - q$ plane high confining pressures, σ_{t0} is the uniaxial tensile failure stress, and ε is a parameter relating to the eccentricity that defines the rate at which the function approaches the asymptote (the flow potential tends to a straight line as the eccentricity tends to zero).

3.3.2 Steel reinforcement

A network of elements is generally used to define the concrete and steel reinforcement components of a reinforced concrete structure in a finite element model. Tavarez (2001) identified three alternative techniques currently employed to model steel reinforcement in RC beams in finite element models; these are the discrete model, the embedded model, and the smeared model as shown in Figure 23.

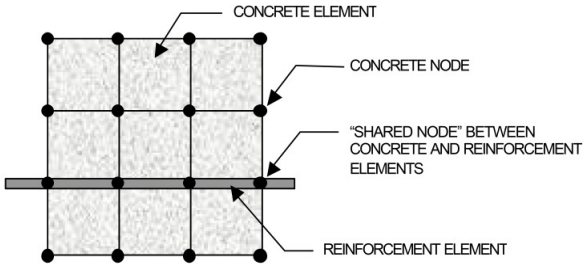

(a) Discrete model

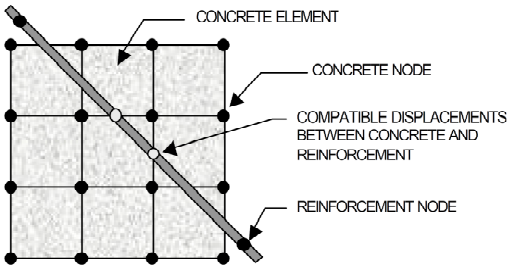

(b) Embedded model

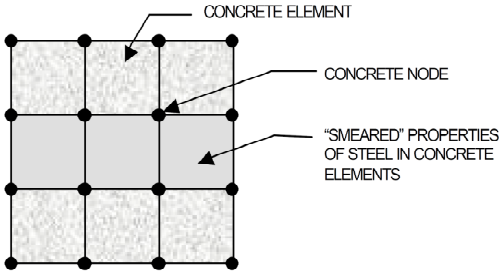

(c) Smeared model

Figure 23: Steel reinforcement models for RC beams (Tavarez, 2001)

The discrete model employs bar or beam elements for the reinforcement that are linked to the concrete mesh nodes as shown in Figure 23(a). Thus, the reinforcement and concrete mesh nodes are shared and co-exist in the spatial position in the model. The limitation of the discrete model is that the location of the reinforcement restricts the concrete mesh layout. Furthermore, only the mechanical characteristics of the reinforcement is represented, as the physical dimensions of these types of elements are not considered.

The concrete mesh restriction is negated in the embedded model, shown in Figure 23(b), as the concrete and steel reinforcement elements are evaluated separately.

However, the model is structured in a way that maintains displacement compatibility between the steel reinforcement and surrounding concrete elements. This model is ideal for simulating complex steel reinforcement layouts. However, computational time and cost increases owing to the increased number of nodes and degrees of freedom.

The smeared model shown in Figure 23(c) simulates the steel reinforcement as uniformly distributed throughout a defined region within the concrete element mesh. This approach is well suited for large-scale structural models where the overall response of the structure is not governed by steel reinforcement ratios.

Plasticity models for steel reinforcement

The uniaxial static behaviour of steel reinforcement is defined with the classic metal plasticity model in Abaqus (2010). Since steel reinforcement exhibits ductile behaviour at stress levels that are orders of magnitude less than the elastic modulus (E), the relevant stresses and strains are "true" stress (σ_{true}) and logarithmic plastic strain (ε_{ln}^{pl}), respectively. Nominal stress (σ_{nom}) and strain (ε_{nom}) data from a uniaxial test is converted to true stress and logarithmic plastic strain by the following expressions (Abaqus, 2010).

$$\sigma_{true} = \sigma_{nom}(1 + \varepsilon_{nom}) \tag{3.12}$$

$$\varepsilon_{ln}^{pl} = \ln(1 + \varepsilon_{nom}) - \frac{\sigma_{true}}{E} \tag{3.13}$$

The rate dependent nonlinear behaviour of steel reinforcement has been modelled with the Johnson-Cook plasticity model. This model is ideal for high strain rate applications and uses a Mises yield surface with associated flow. The rate dependent yield stress is expressed as:

$$\bar{\sigma} = [A + B(\bar{\varepsilon}^{pl})^n]\left[1 + C\ln\left(\frac{\dot{\bar{\varepsilon}}^{pl}}{\dot{\varepsilon}_0}\right)\right](1 - \hat{\theta}^m) \tag{3.14}$$

where $\bar{\sigma}$ is the yield stress at non-zero strain rate, $\dot{\bar{\varepsilon}}^{pl}$is the equivalent plastic strain rate, $\bar{\varepsilon}^{pl}$ is the plastic strain rate and A, B, n, m are material parameters. $\hat{\theta}^m$ is the non-dimensional temperature and set to zero since temperature independent steel behaviour has been assumed in this study. The only parameters that have to be defined for the Johnson-Cook model are $\dot{\varepsilon}_0$ and C. In the present study, $\dot{\varepsilon}_0$ was set as 10^{-4} s^{-1} and C was approximated based on the Mavlar & Crawford (1998b) proposed DIF expression for steel reinforcement (Kamali, 2012):

$$C = \frac{\left(\frac{\dot{\bar{\varepsilon}}^{pl}}{\dot{\varepsilon}_0}\right)^{(0.074-0.04\frac{f_y}{414})} - 1}{\ln\left(\frac{\dot{\bar{\varepsilon}}^{pl}}{\dot{\varepsilon}_0}\right)} \tag{3.15}$$

3.3.3 Fibre reinforced polymer

In Abaqus (2010), the post failure response of FRP is captured in the framework of an anisotropic damage model where four different modes of failure are considered, namely:

i) Fibre rupture in tension;
ii) Fibre buckling and kinking in compression;
iii) Matrix cracking under transverse tension and shearing; and
iv) Matrix crushing under transverse compression and shearing

The postfailure damage response of the FRP is obtained from

$$\sigma = \boldsymbol{C_d}\varepsilon \tag{3.16}$$

where ε is the strain and $\boldsymbol{C_d}$ is the elasticity matrix. The elasticity matrix has the form

$$\boldsymbol{C_d} = \frac{1}{D}\begin{bmatrix} (1-d_f)E_1 & (1-d_f)(1-d_m)v_{21}E_1 & 0 \\ (1-d_f)(1-d_m)v_{12}E_2 & (1-d_m)E_2 & 0 \\ 0 & 0 & (1-d_s)GD \end{bmatrix} \tag{3.17}$$

$$D = 1 - (1 - d_f)(1 - d_m)v_{12}v_{21} \tag{3.18}$$

where d_f reflects the current state of fibre damage, d_m reflects the current state of matrix damage, d_s reflects the current state of shear damage, E_1 is the elastic modulus in the fibre direction, E_2 is the elastic modulus perpendicular to the fibres, G is the shear modulus, and v_{12} and v_{21} are Poisson's ratios.

User defined mechanical properties for the FRP are required for this model in order to define damage initiation and evolution. These include tensile, compressive and shear strengths in both the longitudinal and transverse directions relative to the fibre orientation. Fracture energies for the various FRP components are also required.

3.3.4 FRP-concrete bond interface

Results of experimental studies has shown that the predominant failure mode of FRP plated RC beams subjected to low velocity impact is combined flexure and shear failure with IC debonding of FRP. In the present study, IC debonding is dealt with explicitly based on the FE modelling approach developed by Chen & Teng (2011).

Chen & Teng (2011) developed a FE model in Abaqus to accurately model IC debonding. This was achieved by accurate modelling of localised flexural cracking. In order to predict the formation of localised cracks accurately, the FE model proposed by the authors included three elements, namely:

i) An accurate constitutive model for modelling cracked concrete based on the smeared crack approach taking into account the postcracking behaviour of concrete;
ii) An accurate bond interface model for the bond behaviour between FRP and concrete; and
iii) An accurate bond interface model for the bond behaviour between steel reinforcement and concrete.

In the model developed by Chen & Teng (2011), the bond behaviour between FRP and concrete is represented using interfacial elements. The properties of the interfacial elements normal to the interface are assumed to behave linear-elastically with a stiffness of the adhesive layer. This assumption is based on results of analytical and experimental studies by others showing that the interaction between shear and normal directions is negligible. Furthermore, these studies show that interfacial normal stress in the FRP-concrete bond line away from plate ends is insignificant compared to the interfacial shear stress, implying that the contribution of normal stress on IC debonding is negligible (Chen & Teng, 2011).

Following Chen & Teng (2011), the simplified FRP bond-slip (traction-separation) model developed by Lu et al (2005) is used to define the properties of the interfacial elements parallel to the interface. This model is a semi-empirical approach based on the predictions of a meso-scale FE model, with appropriate modification to match the experimental results of key parameters (Lu et al, 2005).

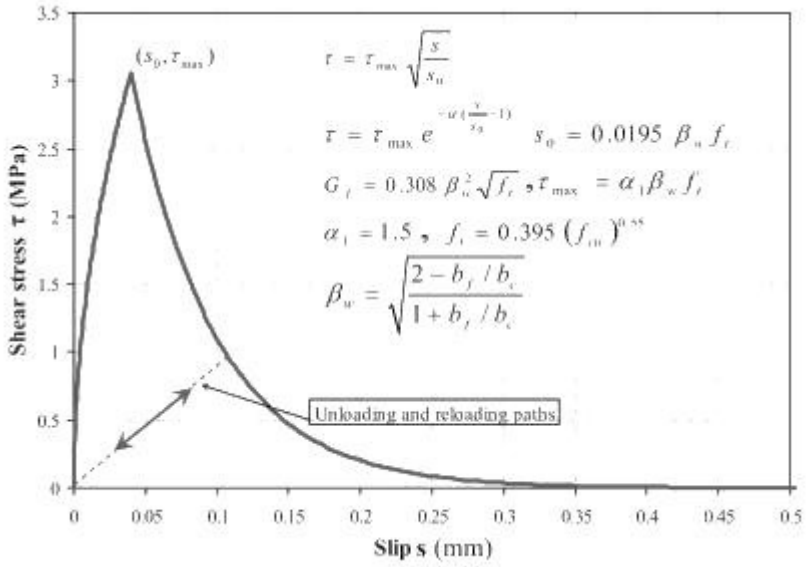

Figure 24: FRP-concrete bond slip curve by Lu et al (2005) For f_c'=30MPa and b_f/b_c=1 (Chen & Teng, 2011)

The bond-slip curve developed by Lu et al (2005) is shown in Figure 24 where τ (MPa) is the local bond (shear) stress; s (mm) is the local slip; τ_{max} (MPa) is the local bond strength (i.e. the maximum bond/shear stress experienced by the interface); s_0 (mm) is the slip when the bond stress reaches τ_{max}; β_w is the width ratio factor; b_c

(mm) is the width of the RC beam specimen; b_f (mm) is the width of the FRP strip; f_t (MPa) is concrete tensile strength; f_c (MPa) is the concrete cylinder compressive strength; and f_{cu} (MPa) is the concrete cube compressive strength. The local bond shear stress τ as defined in this model is equivalent to the bond stress t defined in Abaqus.

In Abaqus, the elastic properties of the adhesive material is defined using uncoupled traction-separation behaviour where t_n^0, t_s^0, and t_t^0 represents the peak values of the nominal stress when the deformation is either purely normal to the interface, or purely in the first or the second shear direction, respectively. The adhesive thickness is set to 1mm thereby ensuring that the nominal strain is equal to separation.

Damage initiation and evolution is defined in the proposed FE model to represent the interfacial stiffness degradation of the adhesive based on the Lu et al (2005) bond-slip model discussed above. The quadratic nominal stress failure criterion is chosen for damage initiation in the cohesive elements. On this basis, damage is assumed to initiate when the nominal stress ratio reaches a value of one as defined in the expression below (Abaqus, 2010):

$$max\left\{\frac{t_n}{t_n^0}, \frac{t_s}{t_s^0}, \frac{t_t}{t_t^0}\right\} = 1 \tag{3.19}$$

In Abaqus, the damage evolution law describes the rate of stiffness degradation once the damage criterion is reached. The scalar damage variable, D, represents the overall material damage, evolving from an initial value of 0 when the damage criterion is reached, to 1 when the maximum displacement during the loading history is attained. Stress components in the traction-separation material model are modified by damage based on the following expressions (Abaqus, 2010):

$$t_n = \begin{cases} (1-D)\bar{t}_n, & \bar{t}_n \\ \bar{t}_n & \text{(no damage to compressive stiffness)} \end{cases} \tag{3.20}$$

$$t_s = (1-D)\bar{t}_s \tag{3.21}$$

$$t_t = (1-D)\bar{t}_t \tag{3.22}$$

where $\bar{t}_n$, $\bar{t}_s$and $\bar{t}_t$ are the stress components predicted by the elastic traction-separation behaviour for the current strains without damage. Damage evolution under a combination of normal and shear deformation across the interface is defined as a function of effective displacement given by:

$$\delta_m = \sqrt{\langle\delta_n\rangle^2 + (\delta_s)^2 + (\delta_t)^2} \tag{3.23}$$

The damage model described above is implemented by defining an initial undamaged elastic modulus and the damage variable (D). The initial elastic modulus, expressed as initial elastic stiffness K_0, is estimated by the following expression (Lu et al, 2005):

$$K_0 = K_a K_c/(K_a + K_c) \tag{3.24}$$

where $K_a = G_a/t_a$ and $K_c = G_c/t_c$ is the elastic stiffness of the adhesive and concrete, respectively. G_a and t_a is the elastic shear modulus and effective thickness of the adhesive, respectively. G_c is the elastic shear modulus of concrete and t_c is the effective thickness of the concrete whose deformation forms part of the interfacial slip. Lu et al (2005) found that $t_c = 5mm$ leads to a close approximation of the initial stiffness of the bond-slip curve in Figure 24, and is therefore adopted in the present study. The damage variable is then defined according to equation (3.20) to (3.22) for each point on the bond-slip curve in the Abaqus Property Module, based on the undamaged initial elastic modulus.

3.4 Constitutive models for plain concrete

During the past 10 years, finite element analysis software has been used extensively in simulating the dynamic response off RC structures under impact loading (Jiang *et al*, 2012). However, the development of appropriate concrete constitutive material models in this field remains an area of further research owing to complex concrete behavioural aspects in high-strain rate applications. These include nonlinear stress-strain response, tension cracking, biaxial stiffening, strain softening phenomena, post-fracturing behaviour and stiffness degradation (Tavarez, 2001).

Numerous concrete material models of varying sophistication have been developed. Strain-rate dependency, as well as strain hardening and pressure hardening are basic aspects common in these models (Tu & Lu, 2009). In the analysis of concrete dynamic behaviour, the simulation of the strain-rate dependent strength enhancement of concrete is considered one of the key components (Hentz *et al*, 2004). The strain rate dependent response of RC structures is associated with three different effects. These are (Ozbolt & Sharma, 2011):

i) Rate dependency of growing microcracks (effect of inertia at microcrack level)
ii) Viscous behaviour of the bulk material between the cracks (viscosity or concrete creep due to water content)
iii) Influence of structural inertia forces

The first two effects are related to relatively low and medium strain rates for RC elements, which exhibit both cracking and damage phenomena, whereas the third effect governs for higher strain rates such as that associated with impact.

Owing to the complexity of concrete models and the importance of the selection of appropriate model parameters in model performance, an adequate understanding of the modelling formulation is required (Tu & Lu, 2009). For this reason a brief overview of the underlying principles of selected concrete models for the nonlinear behaviour of concrete under dynamic loading are presented in the sections that follow.

3.4.1 General classification of models

According to Jiang *et al* (2012), concrete material models in most FE codes may be classified into three categories based on their method of determining plastic deformation. The first category deals with models where the associative flow rule of plasticity is used to calculate the plastic strain increment in order to capture the plastic volume expansion under shear loading at low confining pressure. In placticity theory, orientation of plastic strain vectors is governed by a flow rule based on the assumed existence of a plastic potential function, to which the incremental strain vectors are

orthogonal (Desai & Siriwardane, 1984). The plastic strain increment $d\epsilon_{ij}^{p}$ is expressed as (Desai & Siriwardane, 1984):

$$d\epsilon_{ij}^{p} = \lambda \frac{\partial Q}{\partial \sigma_{ij}} \tag{3.25}$$

which is referred to as the nonlinearity rule where Q is the plastic potential function, λ is a positive scalar factor of proportionality and σ_{ij} is the symmetric stress tensor. Where the plastic potential function Q and the yield criterion f are the same, the material is considered to follow the associative flow. Typical concrete models included in this category are the Mohr–Coulomb model, Drucker-Prager model, elasto-plastic cap model and elasto-plastic damage cap model (Jiang *et al*, 2012)

The second category involves the adaptation of the Prandtl-Reuss plastic flow theory, using von Mises as the plastic potential, to determine the plastic strain increment. The Prandtl-Reuss flow rule is expressed as (Krausz *et al*, 1990)

$$d\epsilon_{ij}^{p} = \lambda S_{ij} \tag{3.26}$$

where S_{ij} is deviatric stress tensor. Plastic volume strain is determined from the equations of state. Equations of state provide the means to link three inter-dependent thermodynamic parameters, namely the pressure p, density ρ, and internal energy e (Tu & Lu, 2009). Typical concrete models included in this category are Holmquist–Johnson–Cook model, Riedel–Thoma–Hiermer model and the Pseudo–Tensor model.
The third category relates to models where non-associated plastic flow theory is used to determine the plastic strain increment. In this case, the plastic potential function and the yield function differs. The plastic-damage model is a typical example.

3.4.2 Nonlinear behaviour of concrete under reversed cyclic loading

Realistic stress-strain material models are required to simulate the dynamic response of a concrete element when using computational analysis methods. Concrete elements subjected to impact exhibits a cyclic compression-tension response. The post-peak

behaviour of concrete subjected to unloading/reloading cycles is characterised by degradation of the elastic stiffness in tension and compression, and crack closure effects at the micro- and meso-scale (van Meier, 1997).

Although continuum damage and plasticity based constitutive models can simulate the real cyclic behaviour of concrete accurately, its application in engineering practice is limited due to the need to define a multitude of parameters that are difficult to define using conventional laboratory tests (Sima *et al*, 2008). For example, typical laboratory tests required to define the parameters of the concrete damage plasticity model in Abaqus includes (Jankowiak & Lodygowski, 2005):

i) Uniaxial compression tests
ii) Uniaxial tension tests
iii) Biaxial failure in plane state of stress
iv) Triaxial test of concrete (superposition of the hydrostatic state of stress and the uniaxial compression stress)

Therefore, only empirical models derived from the generalization of test results for concrete under variable loading histories are considered in this study. Models developed by Sinha et al (1964), Karsan and Jirsa (1969), Yankelevsky and Reinhardt (1987), Chang and Mander (1994), Bahn and Hsu (1998), Elmorsi et al (1998), Palermo and Vecchio (2003), Mansour and Hsu (2005), Sima et al (2008), and Aslani and Jowkarmeimandi (2012) are amongst some of the many empirical formulations documented in the literature.

Sinha et al (1964) undertook one of the first experimental investigations into the stress-strain response of plain concrete under cyclic loading. The experiment was performed in a series of 48 tests on concrete cylinders with compressive strengths ranging from 20 to 28 MPa subjected to cyclic axial. The aim of the study was to obtain information on the properties of the envelope curve and the unloading and reloading curves in order to derive analytical stress-strain relations for cyclic loading.

Karsan and Jirsa (1969) performed an experimental investigation on the behaviour of plain concrete subjected to repetitions of compressive stress under varying load

regimes. The experiment comprised 46 short rectangular columns with compressive strengths ranging from 24 to 35 MPa. Four different loading test regimes were considered in the study. These included:

i) Monotonic increasing loading to failure
ii) Cycles to envelope curve
iii) Cycles to envelope curve adding a specified strain increment during each cycle
iv) Cycles between maximum and minimum stress levels

The authors found that that the loading and unloading curves are not unique but depend on defining the peak stress-strain values of the previous loading cycle in order to estimate the response.

Palermo and Vecchio (2003) developed a constitutive model formulated in the context of a smeared rotating crack model, consistent with a compression field approach. The model considers the cyclic compression and tension behaviour. The unloading and reloading paths were linked to the envelope curve represented by the monotonic response curves. Unloading was modelled using a nonlinear Ramberg-Osgood formulation, whereas reloading was modelled as a linear curve with a degrading reloading stiffness.

Sima et al (2008) defined a constitutive model for the simulation of the cyclic response of concrete in both compression and tension. Some of the fundamental aspects of the model include the simulation of strength and stiffness degradation due to cyclic loading described by independent tension and compression damage parameters, the shape of the hysteric loops considering its dependency with damage accumulation in the concrete, and crack opening and closing.

Aslani and Jowkarmeimandi (2012) developed a constitutive model for the simulation of the response of unconfined concrete subjected to cyclic loadings in both compression and tension. The model can reproduce the complex behaviour of concrete under any cyclic loading history (full loading and partial loading) by incorporating similar features such as that described for the Sima et al (2008) model above. The model was verified based on the experimental results of others. The

proposed model showed satisfactory agreement with the experimental results. The model is user friendly and suitable for implementation into a finite element programme in that the input data required can be obtained through conventional monotonic compression and tension tests. In the absence of experimental data, the concrete parameters required for these models may be determined based on the expressions recommended in CEB Model Code 90 (CEB-FIP 1993, 1999) listed in Table 2.

Table 2: Recommended formulae for concrete material parameters: CEB-FIP Model Code 90

Compressive cylinder strength[(a)]	f_c'	(MPa)	$f_{ck} + 8$
Compressive strain at peak[(a)]	ε_c'	(mm/m)	$-0.0017 - 0.0010\left(\frac{f_c'}{70}\right)$
Tensile strength[(b)]	f_t'	(MPa)	$1.4\left(\frac{f_{ck}}{10}\right)^{\left(\frac{2}{3}\right)}$
Fracture energy[(a)]	G_f	(N/m)	$(0.0469d_a^2 - 0.5d_a + 26)\left(\frac{f_c'}{10}\right)^{(0.7)}$

Where:

[(a)]	From (CEB-FIP, 1999)
[(b)]	From (CEB-FIP, 1993)
f_{ck}	Specific characteristic compressive strength

The uniaxial compression and tension relations for describing selected material constitutive models are discussed in the sections that follow.

3.4.2.1 Uniaxial compression behaviour

It has been shown that the envelope curve for concrete subjected to axial cyclic compression can be approximated by the monotonic stress-strain curve. The monotonic curve used for this purpose should comprise some desirable characteristics.

According to (Sima *et al*, 2008) these curves should:

i) Denote the slope at the origin as equal to the initial elastic modulus;

ii) Provide an accurate representation of the ascending and descending post peak (softening) branch; and

iii) Permit the adjustment of the post peak behavior to experimental results.

Selected monotonic compression stress-strain curves for plain concrete is presented in Table 3.

Table 3: Monotonic compression stress-strain curves

Reference	**Ascending branch** $(0 < \varepsilon_c < \varepsilon_c')$	**Descending branch** $(\varepsilon_c' < \varepsilon_c < \varepsilon_{cu})$
Hognestad (1951)	$f_c = f_c'\left[1 - 0.15\left[\frac{\varepsilon_c - \varepsilon_c'}{\varepsilon_{cu} - \varepsilon_c'}\right]\right]$	$f_c = f_c'\left[\frac{2\varepsilon_c}{\varepsilon_c'} - \left[\frac{\varepsilon_c}{\varepsilon_c'}\right]^2\right]$
Smith & Young (1955)	$f_c = f_c'\left(\frac{\varepsilon_c}{\varepsilon_c'}\right)e^{\left(1-\frac{\varepsilon_c}{\varepsilon_c'}\right)}$	
Fujikake (2009)	$f_c = \frac{AX + (B-1)X^2}{1 + (A-2)X + BX^2} f_{cd}'$	
	$A = E_{cd}\varepsilon_{cd}'/f_{cd}'$ $B = (A-1)^2/0.55 \geq 1 - A$ $X = \varepsilon_c/\varepsilon_{cd}'$	$A = E_{0d}\varepsilon_{cd}'/f_{cd}'$ $B = 1$ $X = (\varepsilon_c/\varepsilon_{cd}')^m$, $m = 1.04 + 2 \times (f_{cd}'/100)^2$
Aslani and Jowkarmeimandi (2012)	$f_c = f_c'\left(\frac{n(\varepsilon_c/\varepsilon_c')}{n - 1 + (\varepsilon_c/\varepsilon_c')^n}\right)$	
	$n = n_1 = [1.02 - 1.17(E_{sec}/E_c)]^{-0.74}$	$n = n_2 = n_1 + (a + 28b)$ $a = 3.5(12.4 - 1.66 \times 10^{-2} f_c')^{-0.46}$ $b = 0.83e^{(-911/f_c')}$

Where:

ε_c'	*: strain at peak*	f_c'	*: stress at peak*
ε_{cd}'	*: dynamic strain at peak*	f_{cd}'	*: dynamic stress at peak*
ε_{cu}	*: ultimate strain*	E_c	*: initial elastic modulus*
ε_0	*: strain at elastic limit*	E_{cd}	*: initial dynamic elastic modulus*

The typical hysteric response of a concrete specimen under cyclic loading is shown in Figure 25. When the specimen is initially unloaded from the monotonic envelope curve to zero stress level, the unloading curve is concave from the unloading point. The stiffness degrades due to microcracking and the residual plastic strains are considerably reduced with successive load cycles. Upon reloading from zero stress upto the envelope curve, the reloading stiffness is less than the initial unloading stiffness for a given load cycle.

A brief description of the compression cyclic models considered for implementation in this study, namely by Palermo and Vecchio (2003), Sima *et al* (2008), and Aslani and Jowkarmeimandi (2012), is presented in the sections that follow.

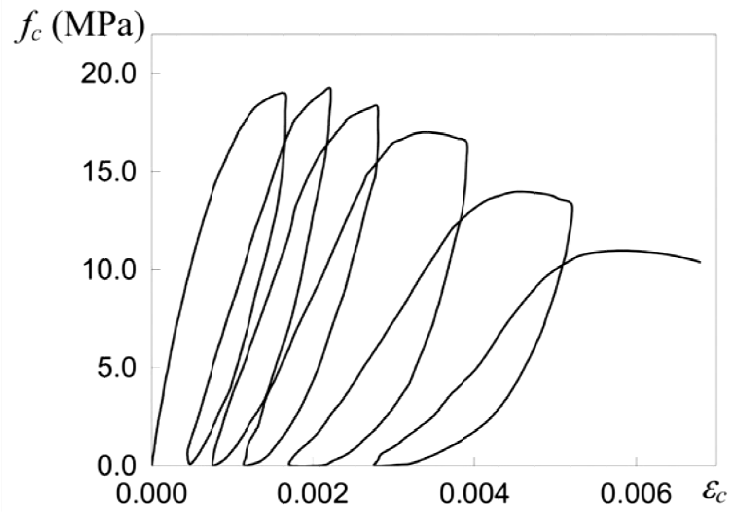

Figure 25: Typical stress-strain response for cyclic compression test (Karsan & Jirsa, 1969)

Cyclic compression model by Palermo and Vecchio (2003)

Palermo and Vecchio (2003) proposed a Ramberg-Osgood formulation for the unloading curve in Figure 26(a) by the equation:

$$\sigma_c(\Delta\varepsilon) = A + B\Delta\varepsilon + C\Delta\varepsilon^N \tag{3.27}$$

where σ_c is the stress in the concrete on the unloading curve, $\Delta\varepsilon$ is the strain increment measured from the instantaneous strain on the unloading path to the unloading strain, parameters A, B and C defined the general shape of the curve, and N is the Ramberg-Osgood power term.

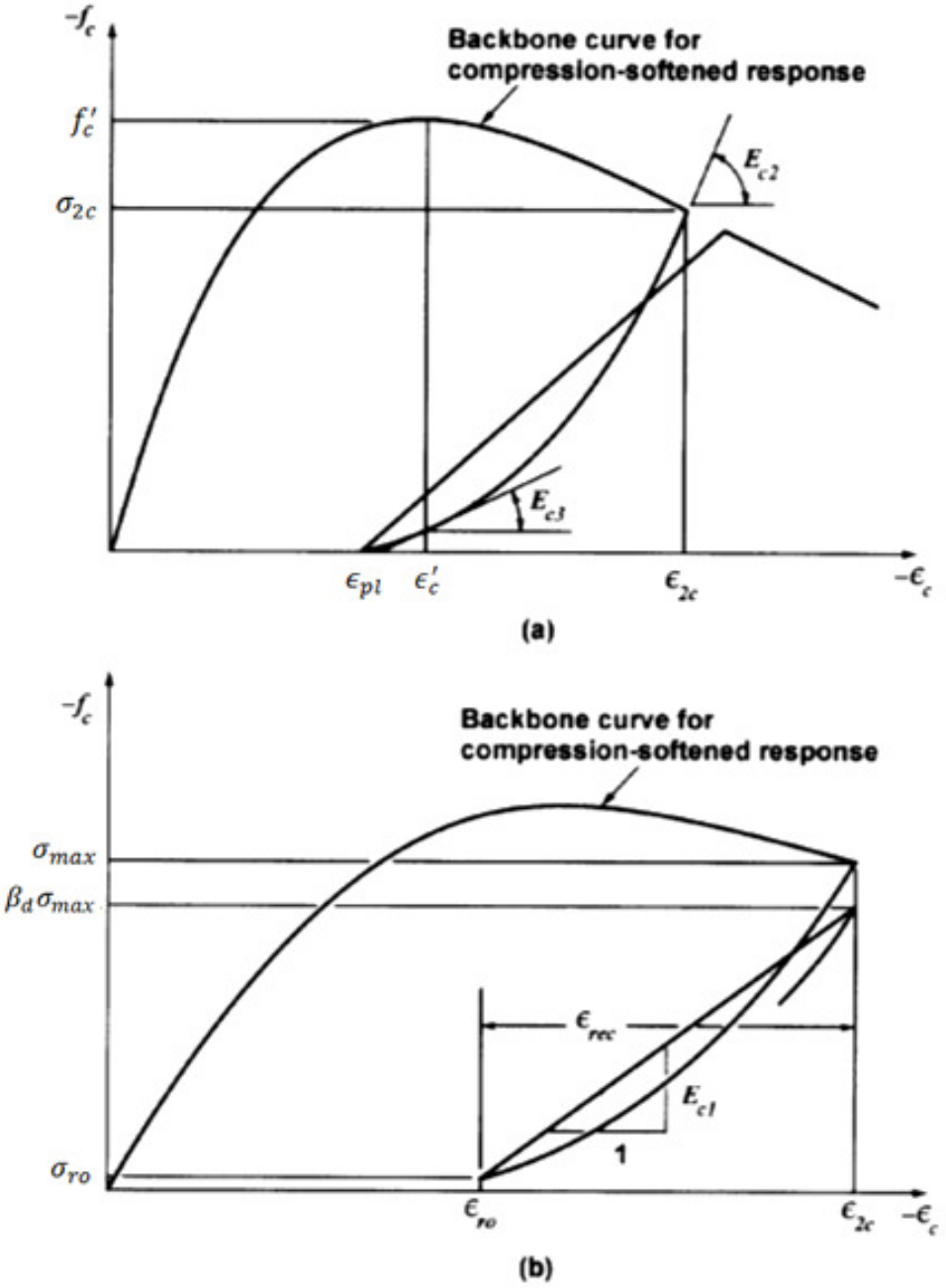

Figure 26: Complete (a) unloading and (b) reloading cycle in compression by Palermo and Vecchio (2003)

By simplifying and applying the boundary conditions in Figure 26, Eq. (3.27) yields:

$$\sigma_c(\Delta\varepsilon) = \sigma_{2c} + E_{c2}(\Delta\varepsilon) + \left[\frac{(E_{c3} - E_{c2})\Delta\varepsilon^N}{n(\varepsilon_{pl} - \varepsilon_{2c})^{N-1}}\right] \tag{3.28}$$

and

$$\Delta\varepsilon = \varepsilon - \varepsilon_{2c} \tag{3.29}$$

$$N = \frac{(E_{c2} - E_{c3})(\varepsilon_{pl} - \varepsilon_{2c})}{\sigma_{2c} + E_{c2}(\varepsilon_{pl} - \varepsilon_{2c})} \tag{3.30}$$

$$\varepsilon_{pl} = \varepsilon_c' \left[0.166 \left(\frac{\varepsilon_{2c}}{\varepsilon_c'} \right)^2 + 0.132 \left(\frac{\varepsilon_{2c}}{\varepsilon_c'} \right) \right] \tag{3.31}$$

Where ε_{pl} is the plastic strain offset, ε_{2c} is the strain at the onset of loading from the envelope (backbone) curve, ε is the instantaneous strain in the concrete. The initial unloading stiffness E_{c2} is set equal to the initial tangent stiffness E_c.The unloading stiffness E_{c3} defining the stiffness at the end of the unloading phase is defined as $0.071E_c$.

Reloading as shown in Figure 26(b) was modelled as linear with a degrading stiffness response, defined as a function of the previous unloading stress and the stress at load reversal given by:

$$\sigma_c = \sigma_{ro} + E_{c1}(\varepsilon_c - \varepsilon_{ro}) \tag{3.32}$$

where σ_c and ε_c are the stress and strain on the reloading curve respectively, σ_{ro} is the sress at reloading reversal and corresponds to a strain of ε_{ro}. E_{c1} is the reloading stiffnesss given by:

$$E_{c1} = (\beta_d \sigma_{max} - \sigma_{ro})/(\varepsilon_{2c} - \varepsilon_{ro}) \tag{3.33}$$

where

$$\beta_d = \frac{1}{1 + 0.10(\varepsilon_{rec}/\varepsilon_c')^{\ 0.5}} \qquad for\ |\varepsilon_c| < |\varepsilon_{pl}| \tag{3.34}$$

and

$$\beta_d = \frac{1}{1 + 0.175(\varepsilon_{rec}/\varepsilon_c')^{\ 0.6}} \qquad for\ |\varepsilon_c| > |\varepsilon_{pl}| \quad (3.35)$$

and

$$\varepsilon_{rec} = \varepsilon_{max} - \varepsilon_{min} \quad (3.36)$$

β_d is the damage parameter, σ_{max} is the maximum stress for the current unloading loop, ε_{rec} is the amount of strain recovered in the unloading process and is the difference between the maximum strain ε_{max} and minimum strain ε_{min} for the current loop.

Cyclic compression model by Sima et al (2008)

(Sima *et al*, 2008) proposed the unloading curve in Figure 27 by the equation:

$$\sigma_c = D^1 e^{D^2\left(1-\frac{\varepsilon_c-\varepsilon_{pl}}{\varepsilon_{un}-\varepsilon_{pl}}\right)} E_0\left(\varepsilon_c - \varepsilon_{pl}\right) \quad (3.37)$$

where

$$D^1 = \frac{r(1-\delta_{un})}{(r-1)} \quad (3.38)$$

$$D^2 = Ln\left[\frac{R(1-\delta_{un})(r-1)}{r}\right] \quad (3.39)$$

with $r = \varepsilon_{un}/\varepsilon_{pl}$, $R = E_{pl}/E_0$, σ_c is the compressive stress in concrete, ε_{pl} is the plastic strain at zero stress, E_{pl} is the tangent stiffness at ε_{pl}, δ_{un} is the compressive damage δ^- at the unloading point.

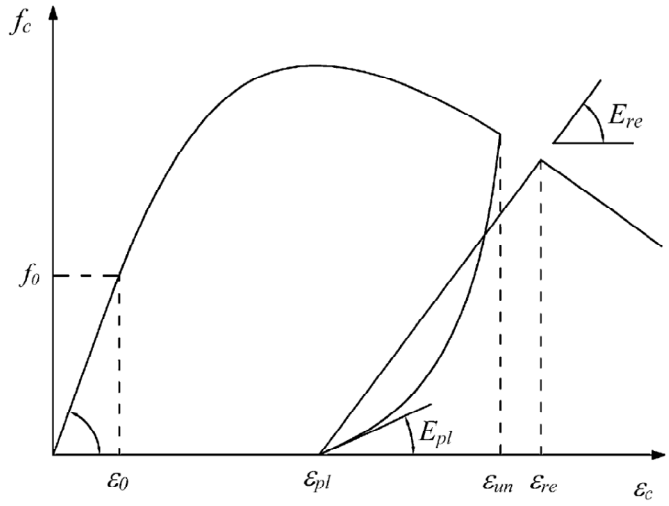

Figure 27: Complete unloading-reloading cycle in compression by Sima et al (2008)

The reloading path is modelled as linear based on a linear relationship between the reloading compression damage δ_{re}, defined as the compressive damage δ^- at the reloading strain ε_{re}, given by:

$$\delta^- = \delta_{un} + \frac{(\delta_{re} - \delta_{un})}{(\varepsilon_{pl} - \varepsilon_{un})} \tag{3.40}$$

for the unloading path, and

$$\delta^- = \delta_{re} \tag{3.41}$$

for the reloading path.

Cyclic compression model by Aslani and Jowkarmeimandi (2012)

Aslani and Jowkarmeimandi (2012) developed a power-type equation for the unloading curve and a linear equation for the reloading curve:

Unloading curve:

$$\sigma_c = \sigma_{un}\left(\frac{1-[(\varepsilon_c-\varepsilon_{un})/(\varepsilon_{pl}-\varepsilon_{un})]}{1+1.2[(\varepsilon_c-\varepsilon_{un})/(\varepsilon_{pl}-\varepsilon_{un})]}\right)^{1.2} \quad (3.42)$$

$$\varepsilon_{pl} = \varepsilon_{un} - \sigma_{un}/E_r \quad (3.43)$$

$$E_r = E_c\left(\frac{(\sigma_{un}/E_c\varepsilon_c')+0.57}{(\varepsilon_c/\varepsilon_c')+0.57}\right) \quad (3.44)$$

Reloading curve:

$$\sigma_c = \sigma_{ro} + E_{c1} - \sigma_{un}(\varepsilon_c - \varepsilon_{ro}) \quad (3.45)$$

$$E_{c1} = \frac{\sigma_{ro}-\sigma_{new}}{\varepsilon_{ro}-\varepsilon_{un}} \quad (3.46)$$

$$\sigma_{new} = \sigma_{un}[1-0.09(\varepsilon_{un}/\varepsilon_{ro})^{0.5}] \quad (3.47)$$

Where σ_{ro} is the stress in the concrete reloading reversal and corresponds to a strain of ε_{ro}, E_{c1} is the reloading stiffness, E_r is the stiffness from the unloading stress σ_{un} to the plastic strain ε_{pl}, σ_{new} is the peak stress on the reloading curve.

3.4.2.2 Uniaxial tension behaviour

The tension behaviour of a concrete specimen strained in uniaxial tension is shown in Figure 28. The ascending branch shows a near linear load-deformation response upto the peak load. Before the peak load is reached, some microcracking occurs. Since the microcracking is uniformly distributed over the specimen at the macro-level, the load deformation relation can therefore be replaced by a stress-strain relation for the concrete. After peak load, strains localise more and more within a crack band width of h, defining shape of the descending branch (tension stiffening) (CEB, 1996).

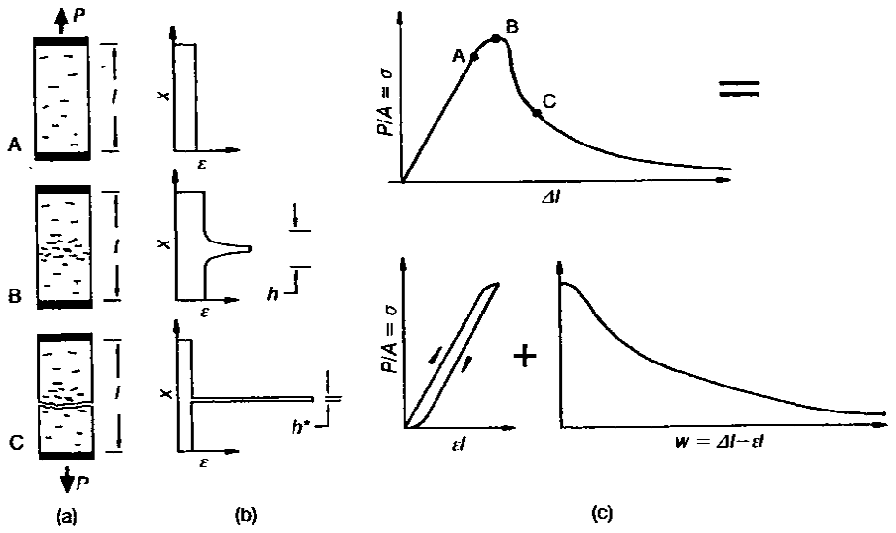

Figure 28: Tensile behaviour of concrete (CEB, 1996)

Since the post-peak behaviour is characterised by crack opening, it is not feasible to use a stress-strain relation for the descending branch (Hordijk, 1991). Furthermore, in instances where little or no reinforcement is present in the concrete as is the case in the present study, the specification of a post-peak stress-strain relation in a FE model introduces mesh sensitivity in the results. The finite element predictions do not converge on a unique solution with mesh refinement due to narrower crack bands (Abaqus, 2010).

The tensile behaviour of concrete can be split into a stress-strain relation outside of the crack band (ascending branch) and a stress-crack opening relation within the crack band (descending branch). The stress-crack opening relation is based on the fictitious crack model by Hillerborg et al (1976), where he collected the deformation of the crack band into the crack width w of a single fictitious crack. (Hordijk, 1991; CEB, 1996)

Studies on the tension behaviour of concrete under monotonic loading is well documented, whereas research relating to cyclic models for tension is rather limited (CEB, 1996). Cyclic models by Gylltoft (1984), Rots et al (1985), Reinhardt (1986) and Yankelevsky & Reinhardt (1989) is shown in Figure 29.

.

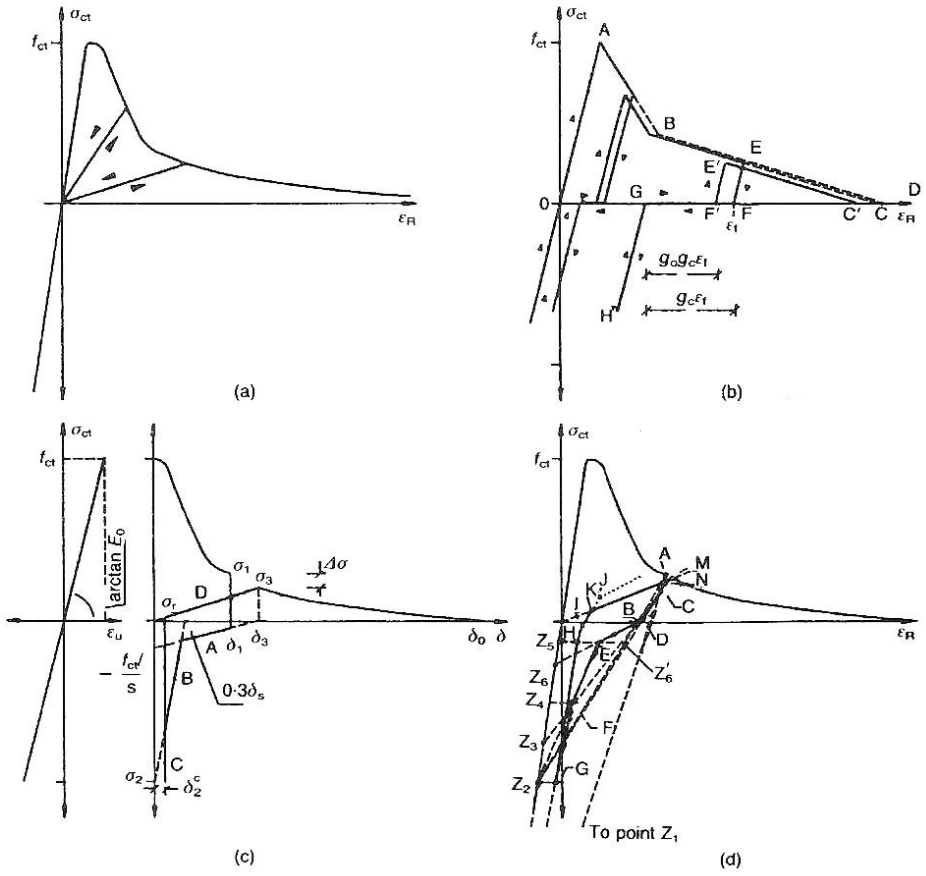

Figure 29: Models for tension under cycling loading: (a) Rots et al; (b) Gylltoft; (c) Reinhardt et al; (d) Yankelesky and Reinhardt (CEB, 1996)

The selection of an appropriate cyclic tension model for concrete is an important consideration in FE modelling of dynamic events. More tensioning stiffening makes it less problematic to obtain numerical solutions. Conversely, insufficient tension stiffening introduces temporarily unstable behaviour in the overall response of the model due to local cracking failure in the concrete (Abaqus, 2010). Furthermore, the cyclic model should include a reasonable representation of the unloading and reloading curves to ensure that the FE model is capable of capturing the real cyclic behaviour. Therefore, considering the above, aspects of the cyclic models presented in Figure 29 that may affect the accuracy of the proposed FE model in this study is listed below (CEB, 1996):

(i) **Gylltoft (1984):**

The envelope line EC shifts to E'C'. This contradicts experimental results.

(ii) **Rots et al (1985):**

This simple model considers the unloading and reloading paths passing through the origin in a straight line. There are no curvilinear unloading-reloading paths (hysteresis loop).

(iii) **Reinhardt (1986):**

This model requires the definition of the stress drop $\Delta\sigma$ at the beginning of the unloading curve at a given stress-deformation state that depends on the lower stress. This model is not appropriate for implementation in FE analysis, since it is not possible to define the lower stress that will be reached at the beginning of a given hysteresis loop.

(iv) **Yankelevsky & Reinhardt (1989):**

The focal-point model requires the definition of several focal, auxiliary and intersection points to define the unloading and reloading curves. Although this model represents the real concrete behaviour well, the model is complex due to the large number of points required. Therefore, this model is difficult to implement in FE analysis.

The model developed by Hordijk (1991) addresses many of these shortcoming since:

(i) Tension behaviour defined with this model compare favourably with experimental results, therefore providing an accurate representaion of the real response.

(ii) Hysteresis loops are defined by fewer characteristic points compared with the focal point model and is therefore easier to implement in a FE analysis.

Therefore, the model by Hordijk (1991) is adapted in the present study. A brief overview thereof is presented below.

Continuous-function model by Hordijk (1991)

The model proposed by Hordijk (1991) describes the post-peak tension behaviour in terms of a stress-crack opening relation whereby crack opening is defined in terms of the fictitious crack model by Hillerborg et al (1976). It comprises of a series of continuous functions, hence it is termed the continuous function model.

The model comprises three empirical expressions for the unloading curve (I), the gap in the envelope curve (II), and the reloading curve (III) as shown in Figure 30.

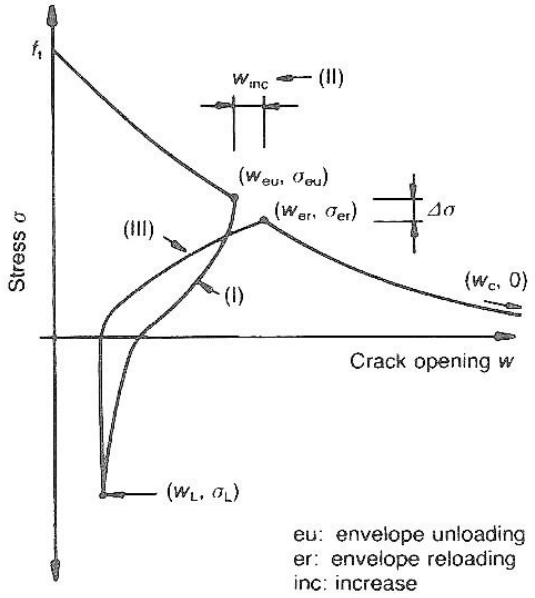

Figure 30: Continuous function model by Hordijk (1991) (CEB, 1996)

The envelope curve is given by Hordijk (1991):

$$\frac{\sigma_t}{f_t} = \left[1 + \left(c_1 \frac{w}{w_c}\right)^3\right] exp\left(-c_2 \frac{w}{w_c}\right) - \frac{w}{w_c}\,(1 + c_1^3)\exp(-c_2) \quad (3.48)$$

where f_t is the tensile strength of the concrete, coefficients c_1 and c_2 are 3 and 6.93, respectively, w is the crack opening, and w_c is the crack opening where stress can no longer be transferred across the crack and is defined as $5.14G_f/f_t$ where G_f is the fracture energy.

The starting point of the unloading curve is defined by the co-ordinate (w_{eu}, σ_{eu}). The unloading curve (I) is given by:

$$\frac{\sigma_t}{f_t} = \frac{\sigma_{eu}}{f_t} + \left(\frac{1}{3\left(\frac{w_{eu}}{w_c}\right) + 0.4}\right)\left\{0.014\left[\ln\left(\frac{w}{w_{eu}}\right)\right]^5 - 0.57\sqrt{\left(1 - \frac{w}{w_{eu}}\right)}\right\} \quad (3.49)$$

For reloading initiating from a lower stress level σ_L, the gap in the envelope curve (II) is given by:

$$\frac{w_{inc}}{w_c} = 0.1\frac{w_{eu}}{w_c}\left[\ln\left(1 + 3\frac{\sigma_{eu} - \sigma_L}{f_t}\right)\right] \quad (3.50)$$

From the co-ordinate (w_L, σ_L) up to (w_{er}, σ_{er}) on the envelope curve, the reloading curve (III) is given by:

$$\frac{\sigma_t}{\sigma_L} = 1 + \left\{\frac{1}{c_3}\left(\frac{w - w_L}{w_{er} - w_L}\right)^{0.2c_3} + \left[1 - \left(1 - \left(\frac{w - w_L}{w_{er} - w_L}\right)^2\right)\right]^{c_4}\right\} \frac{c_3}{c_3 + 1}\left(\frac{\sigma_{er}}{\sigma_L} - 1\right) \quad (3.51)$$

With the coefficients c_3 and c_4 given by:

$$c_3 = 1 + 3\left(\frac{f_t - \sigma_L}{f_t}\right)^{-1-0.5\frac{w_{eu}}{w_c}}\left[1 - \left(\frac{w}{w_c}\right)^{\frac{0.71f_t}{f_t - \sigma_L}}\right] \quad (3.52)$$

$$c_4 = \left[2\left(3\frac{f_t - \sigma_L}{f_t}\right)^3 + 0.5\right]^{-1} \quad (3.53)$$

The above expressions describe the cyclic behaviour for the complete unloading-reloading loops originating from and terminating at the envelope curve. For partial unloading-reloading within these loops, the response is shown in Figure 31. A counter i is used to describe these inner loops.

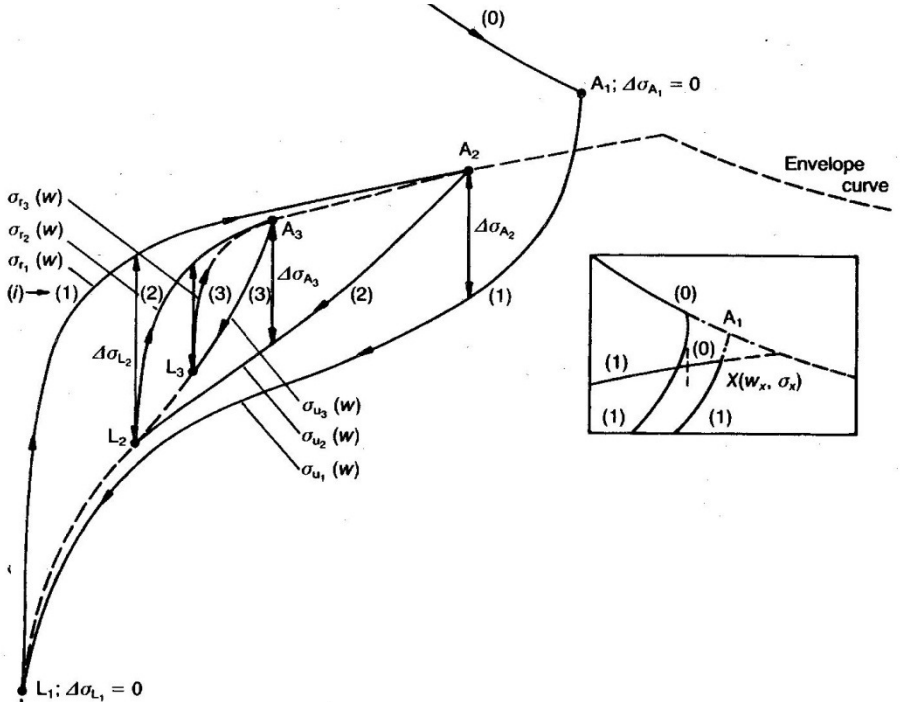

Figure 31: *Procedure for partial unloading-reloading inner loops in CFM (Hordijk, 1991)*

For the envelope curve, this counter is taken as zero and is increased by 1 each time there is a reversal in crack opening direction before the crack opening at the previous reversal has been reached. The basis for the inner loop behaviour is that they return to the same point of origin. In other words, the damaging effect due to load cycling within a loop is not taken into account. A_i denotes a point where the direction changes from an opening crack into a closing crack and L_i denotes the opposite reversal in the crack opening direction. w and $\sigma_{r_i}(w)$ denote the stress as a function of crack opening for unloading and reloading curves, respectively.

The unloading curves for the inner loops are given by:

$$\Delta\sigma_{A_i} = \sigma_{A_i} - \sigma_{u_1}(w_{A_i}) - \sum_{n=3}^{i} \left(\frac{w_{A_i} - w_{L_{n-2}}}{w_{A_{n-1}} - w_{L_{n-2}}} \right)^2 \Delta\sigma_{A_{n-1}} \qquad (3.54)$$

$$\sigma_{u_i}(w) = \sigma_{u_1}(w) + \sum_{n=2}^{i} \left(\frac{w - w_{L_{n-1}}}{w_{A_n} - w_{L_{n-1}}} \right)^2 \Delta\sigma_{A_n} \tag{3.55}$$

The reloading curves for the inner loops are given by:

$$\Delta\sigma_{L_i} = \sigma_{r_i}(w_{L_i}) - \sigma_{L_1} - \sum_{n=3}^{i} \left(\frac{w_{L_i} - w_{A_{n-1}}}{w_{L_{n-1}} - w_{A_{n-1}}} \right)^8 \Delta\sigma_{L_{n-1}} \tag{3.56}$$

$$\sigma_{r_i}(w) = \sigma_{r_1}(w) - \sum_{n=2}^{i} \left(\frac{w - w_{A_n}}{w_{L_n} - w_{A_n}} \right)^8 \Delta\sigma_{L_n} \tag{3.57}$$

3.5 Summary

This chapter dealt with the salient features of the dynamic analysis algorithm employed in this study. Furthermore, it dealt with the selection of concrete, steel reinforcement and FRP bond interface models. The following material and FRP bond interface models were adapted for implementation in the FE model of the present study:

(i) The discrete model was selected to define the steel reinforcement bars. The uniaxial static behaviour of steel reinforcement was defined with the classic metal plasticity model. Nominal stress and strain data from the uniaxial tests provided in the literature used for FE model verification purposes was converted to true stress and logarithmic plastic strain. The Johnson-Cook plasticity model was selected to define the rate dependent nonlinear behaviour.

(ii) FRP was modeled as linear elastic-brittle. Insufficient material data was provided in the literature used to verify the FE model, in order to define the anisotropic damage model for FRP described in section 3.3.3.

(iii) The FRP bond interface was modelled using the approach developed by Chen & Teng (2011) to capture the effects of shear and flexural crack formation of concrete on the interface. Following Chen & Teng (2011), the simplified FRP bond-slip (traction-separation) model developed by Lu et al (2005) was used to

define the properties of the interfacial elements parallel to the interface in Abaqus/Explicit.

(iv) For concrete, the CDP model was selected since it is capable of defining features of material behaviour associated with the cyclic response anticipated for the FRP strengthened RC beam under impact. These features include the ability to define softening behaviour in tension, different yield strengths in tension and compression, and degradation and recovery of elastic stiffness in tension and compression during cyclic loading.

The CPD model for concrete adapted in the Abaqus/Explicit FE model provides the analytical framework to define the material behaviour. Several constitutive models were considered to describe the theoretical framework of the CPD model. Owing to the advantages compared with other models considered, the constitutive material models by Aslani and Jowkarmeimandi (2012) and Hordijk (1991) was adapted for implementation in the CDP framework of the proposed FE model to define the nonlinear behaviour of concrete under reversed cyclic loading.

For compression behaviour, the stress-strain envelope curve and hysteresis for concrete in the FE model was defined using the model by Aslani and Jowkarmeimandi (2012). This model was selected since:

i) It can reproduce the complex behaviour of concrete under any cyclic loading history (full loading and partial loading).
ii) The model was verified based on the experimental results of others. The proposed model showed satisfactory agreement with the experimental results.
iii) The model is user friendly and suitable for implementation in a FE model since all the required input data can be obtained through conventional monotonic compression and tension tests.

For tension behaviour, the post-peak stress-crack opening relation and cyclic unloading-reloading for concrete in the FE model was defined using the continuous function model by Hordijk (1991). The model developed by Hordijk (1991) addresses many of the shortcoming of the other models considered as:

(i) Tension behaviour defined with this model compares favourably with experimental results, therefore providing an accurate representation of the real response.

(ii) Hysteresis loops are defined by fewer characteristic points compared with the other models and is therefore easier to implement in a FE model.

The next chapter discusses the development process of the proposed FE model in the present study to simulate the dynamic response of FRP strengthened beams under impact loading, by incorporating the selected material constitutive models outlined above.

4 METHODOLOGY: FINITE ELEMENT MODELLING OF IMPACT

4.1 Introduction

This chapter provides a detailed description of the parameters and system geometry considered in this research in order to develop a finite element model capable of simulating the dynamic response of FRP strengthened beams under low velocity impacts, including the material constitutive models selected in Chapter 3.

4.2 Research design

The behaviour of concrete under dynamic loading differs from that associated with static loading. Concrete properties including ultimate strength, stiffness, fracture energy and peak strain are highly dependent on the strain rate of applied loading (Barpi, 2004; Leppänen, 2002; Cusatis, 2011). Experimental impact studies on FRP strengthened beams by Jerome (1996), Erki & Meier (1999) and Tang & Saadatmanesh (2003) has shown that the predominant failure mode is combined shear and flexure with IC debonding of the FRP. Therefore, appropriate rate-dependent material models and means to simulate IC debonding of FRP are important considerations in developing FE models capable of providing accurate predictions for the dynamic response of CFRP strengthened beams under low velocity impacts.

Limited studies are available that are focused on the response of FRP strengthened RC beams subjected to low velocity impact events. None of the analytical models reported in the literature considered appropriate rate-dependent material models as well as parameters to simulate IC debonding of the FRP since perfect bond was assumed between FRP and concrete in all cases.

The aim of this study is the development of a FE model based on rate dependent material and IC debonding models, eliminating the deficiencies identified in existing FE models. The development process of the FE model is described below:

(i) The finite element program Abaqus/Explicit version 6.10 was used to simulate the dynamic response of FRP strengthened RC beams subjected to impact loading.

(i) The nonlinear behaviour of the concrete beam under reversed cyclic loading due to impact was defined based on the tension and compression constitutive models by Aslani and Jowkarmeimandi (2012) and Hordijk (1991), respectively. In the absence of experimental data, the concrete parameters required for these models were determined based on the expressions listed in Table 2.

(ii) Strain rate dependent material behaviour was accounted for by updating the parameters of the monotonic compression and tension stress-strain relations derived from the constitutive models. This was achieved by using the recommendations for dynamic increase factors in CEB Model Code 2010 (CEB-FIP, 2010) described in Chapter 2. The constitutive models were then implemented in the CPD framework of the FE model.

(iii) FRP interfacial bond behaviour was modelled using the approach developed by Chen & Teng (2011. Following Chen & Teng (2011), the simplified FRP traction-separation model developed by Lu et al (2005) was used to define the properties of the interfacial elements parallel to the bond interface. FRP was modeled as linear elastic-brittle owing to insufficient material data in the literature in order to define the anisotropic damage model for FRP described in Chapter 3.

(iv) Steel reinforcement was modelled as discrete elements. The uniaxial static behaviour of steel reinforcement was defined with the classic metal plasticity model, whereas the rate dependent nonlinear behaviour was modelled using the Johnson-Cook plasticity model.

(v) With the material models defined, the drop-weight test setup was discretised in a three-dimensional mesh. Computational efficiency was improved by employing mass scaling, by modelling the drop-weight as a rigid body, and by assigning the drop-height specific freefall velocity to the drop weight with a separation of 1mm between contact surfaces.

(vi) The capability and accuracy of the proposed FE model was demonstrated through comparisons of its predictions with selected test results of experimental impact studies by Tang (2002) and Tang & Saadatmanesh (2003).

(vii) To this end, the results of the FE model are compared with the measured mid span displacement and support reaction force time histories as well as crack pattern obtained from the impact tests. The experiments are defined in detail in the section that follows.

4.3 Experimental RC beam impact studies by Tang (2002) and Tang & Saadatmanesh (2002, 2003)

Tang (2002) examined the impact effects on plain and RC beams strengthened with FRP. The experimental investigation comprised of a series of 25 rectangular beam specimens tested with impact load induced by a steel cylinder falling drop weight. In a subsequent study, Tang & Saadatmanesh (2003) undertook a similar experimental study on 5 RC rectangular beam specimens Two types of composite laminates were considered in both experimental studies, namely carbon and Kevlar. The test apparatus used in the studies is shown in Figure 32.

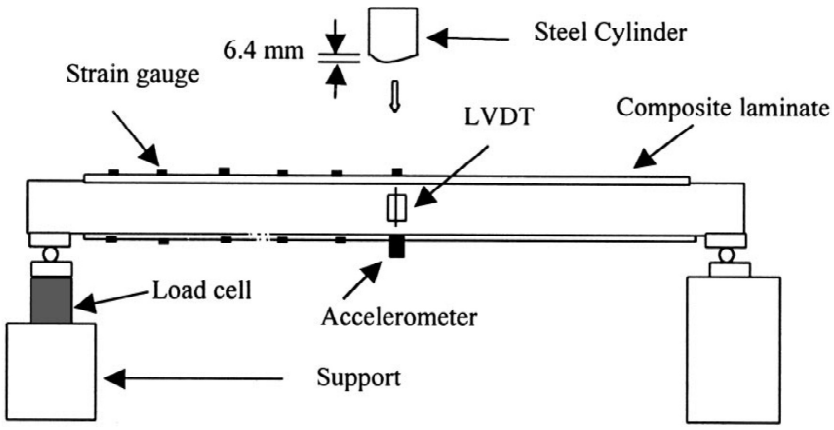

Figure 32: Drop-weight impact test apparatus by Tang & Saadatmanesh (2003)

Impact loading was generated by freely dropping a steel cylinder of mass 222N and 127mm in diameter on the top surface of the RC beam at midspan from either repeated fixed or repeated varying heights. The bottom surface of the steel cylinder had a machined curved surface which was 6.4mm high at the crown. Each end of the beam specimens were supported on two steel plates that enclosed a steel pin to allow for rotation. The ends of the beams were tied to the supports by 12.7mm diameter wire to prevent the beam from rebounding after impact. RC beam failure modes, midspan deflection, support reactions and maximum impact force was measured for each impact test. Details of the test specimens selected for modelling in the present study are listed in Table 4. Laminates were applied to both top and bottom surfaces of the beams.

Table 4: Selected beam specimens for present study

Reference	Identification	Drop Height (m)	Composite laminate	
			Type	Weight (g/m^2)
Tang (2002)	6TB4R	1.370	Kevlar	85
	6TB5R	1.370	Kevlar	307
Tang & Saadatmanesh (2003)	TB1	1.524	Kevlar	307
	TB2	1.524	Carbon	599

The geometry and reinforcement details of the RC beam specimens are presented in Figure 33. Each RC beam specimen was reinforced with two 9.8mm diameter longitudinal steel bars.

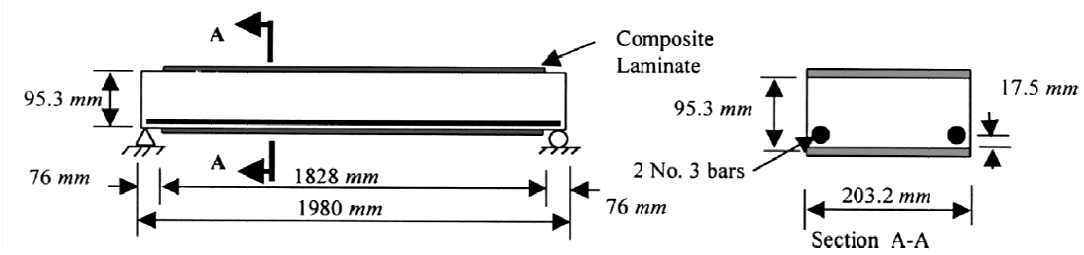

Figure 33: RC beam specimen geometry and reinforcement details (Tang & Saadatmanesh, 2003)

4.4 FE Model Development and Verification

The model was developed in the Abaqus/Explicit version 6.10. In this study, the explicit central difference algorithm available in Abaqus/Explicit was used for the integration of the equations of motion at discrete time intervals Δt. To account sufficiently for the effects of inertia and the nonlinear behaviour of concrete and steel, a three-dimensional analysis was adopted. The description of modelling includes boundary conditions, application of loads, and relevant material models and element types.

4.4.1 Mesh and boundary conditions

A mesh seed of 10mm was used throughout the model shown in Figure 34. The resulting mesh was sufficiently small to achieve solution convergence and reasonable crack visualisation. Concrete was modelled using 19800 three-dimensional eight-node brick elements (C3D8R) as it is well suited for nonlinear analyses involving contact, plasticity and large deformations. Reduced integration and enhanced hourglass control were used for the solid elements. Each steel reinforcement bar was discretised into 99 three-dimensional two-node truss elements (T3D2) with common nodes with the concrete elements. Each FRP bond interface was modelled using a 1820 three-dimensional eight-node cohesive elements (COH3D8) with an assumed thickness of 1 mm. FRP layers were discretised using 1820 three-dimensional eight-node brick elements (C3D8R) with default section controls and the actual ply thickness taken into account. The drop weight was modelled using 3775 three-dimensional eight-node brick elements (C3D8R) with a height and radius of 260.5 mm and 60 mm, respectively.

Boundary conditions are defined in the analysis step module of Abaqus/Explicit and are classed into type format and direct format. The use of type format boundary definition is restricted to stress/displacement analyses. Direct format must be used for all other analysis types. Available boundary conditions, with associated degrees of freedom, in the type format includes

(i) XSYMM Symmetry about a plane X=constant
(degrees of freedom 1,5,6 =0);

(ii) YSYMM Symmetry about a plane Y= constant
(degrees of freedom 2, 4, 6=0);

(iii) ZSYMM Symmetry about a plane Z=constant
(degrees of freedom 3,4,5=0);

(iv) ENCASTRE Fully built-in
(*degrees of freedom 1,2,3,4,5,6=0); and*

(v) PINNED
(degrees of freedom 1,2,3=0).

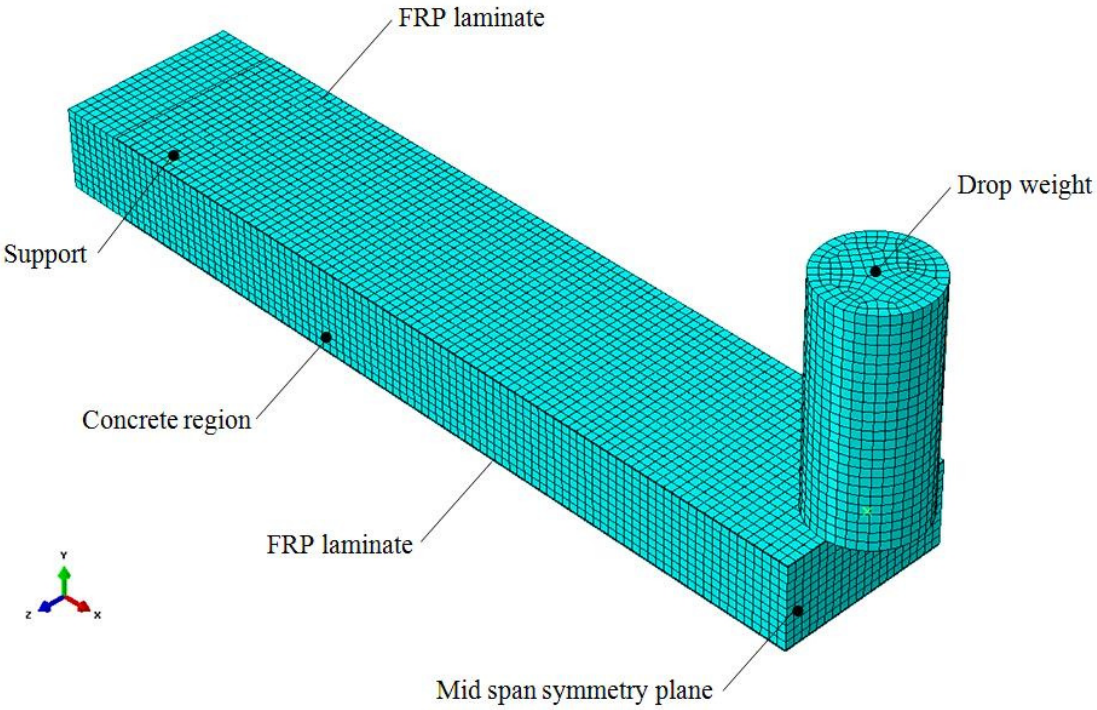

Figure 34: FE model of FRP strengthened RC beam under impact loading

In this study, symmetry about the midspan location was exploited by considering one half of the beam, with the nodes in the plane of symmetry assigned the XSYMM boundary condition.

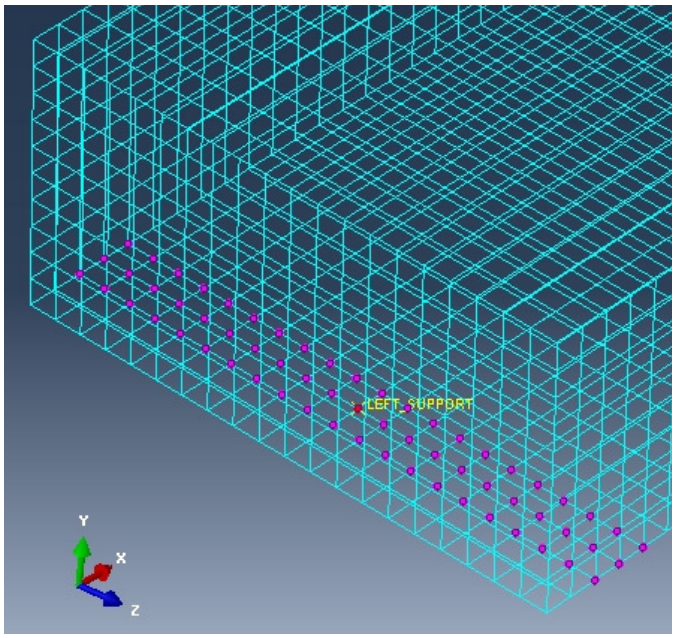

Figure 35: Simplified beam support conditions using tie constraints

Replicating the support conditions of the tests in the FE model proved to be impractical owing to the lack of detailed information on the support setup as used in the experiments. Therefore, the supports were approximated by constraining vertical displacement at single reference node, labelled "LEFT SUPPORT" in Figure 34, at the beam ends. Tie constraints were used to tie two adjacent rows of nodes to the reference node to limit stress concentrations and unrealistic nodal deformations at the supports when a beam rebounds after impact. The tied nodes and reference node are shown as purple and red, respectively, in Figure 35.

4.4.2 Material models

Plain concrete

The properties for concrete material model used in the FE model are presented in Table 6. The tabled values were sourced from the experimental studies by Tang (2002) and Tang & Saadatmanesh (2003). In the absence of experimental data, the values were determined from the expressions in Table 2.

The Concrete Damaged Plasticity (CDP) material model was selected for this study since it is able to capture essential features of concrete behaviour under low velocity

impact. These include dilatency before and after peak strength, pre-peak hardening, post-peak softening and stiffness degradation. Furthermore, the CDP model predicts the post cracking behaviour essential for the accurate modelling of local flexural cracks as adapted in the IC debonding FE model by Chen & Teng (2011). The default parameters of the CDP in Abaqus/Expicit as used in the FE model is presented in Table 5.

Table 5: Plasticity parameters of CDP for FE model

Dilation Angle	Eccentricity	fb0/fc0	K	Viscosity Parameter
30	0.1	1.16	0.666	0

The nonlinear behaviour of the concrete beam was defined based on the tension and compression constitutive models by Aslani and Jowkarmeimandi (2012) and Hordijk (1991), respectively, within the framework of the CPD. Strain rate dependent material behaviour was accounted for by updating the parameters of the monotonic compression and tension stress-strain relations derived from the constitutive models, based on the dynamic increase factors in CEB Model Code 2010 (CEB-FIP, 2010).

Only the full unloading-reloading cyclic responses were included in the CDP framework. By default, the CPD model in Abaqus/Explicit does not allow for stiffness degradation under partial unloading-reloading conditions and the definition of crack closing models. The development of a user subroutine VUMAT in Abaqus/Explicit, a FORTRAN code based utility, to define these aspects in Abaqus/Explicit is outside the scope of the present study.

Table 6: Static and dynamic material properties of concrete for FE Model

			TB-series		6TB-series	
			Static	**Dynamic**	**Static**	**Dynamic**[(b)]
Compressive cylinder strength	f_c'	(MPa)	27.60	31.93	36.10	41.77
Compressive strain at peak	ε_c'	(mm/m)	2.09	2.58	2.22	2.73
Tensile strength	f_t'	(MPa)	2.19	2.81	2.79	3.57
Fracture energy	G_f	(N/m)	56		67	
Max. crack opening displacement	w_c	(µm)	131		124	
Initial elastic modulus	E_c	(GPa)	24.90	34.15[(a)]	28.56	39.17[(a)]
Poisson´s ratio			0.2			
Density	ρ	(kg/m^3)	2400			

Where:

(a) Average of E_c in tension and compression
(b) Assumed strain rate of 1/s based on experimental data

The stress-strain envelope curve and hysteresis for concrete in the FE model was defined using the model proposed by Aslani and Jowkarmeimandi (2012).

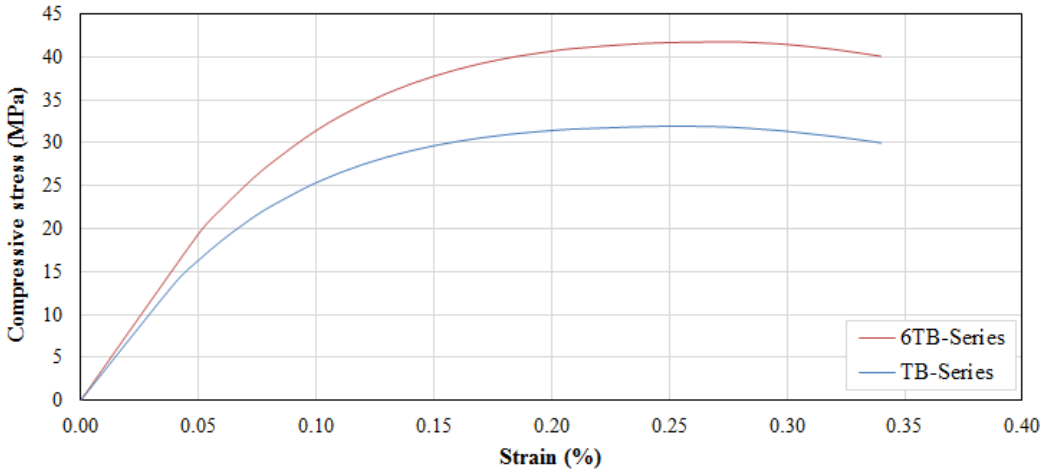

Figure 36: Dynamic compressive stress-strain relation for FE model

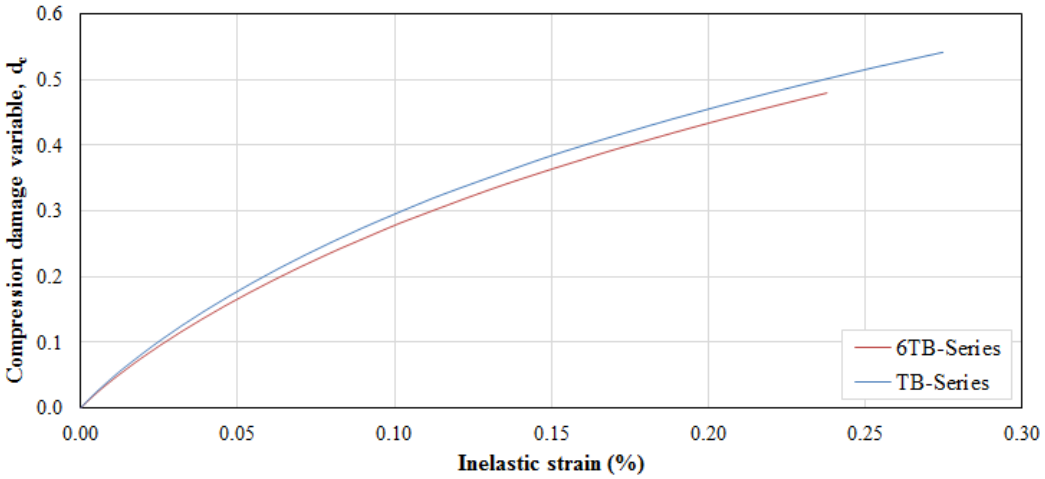

Figure 37: Evolution of concrete compression damage for FE model

The envelope curve for the dynamic compression stress-strain relation is shown in Figure 36. Concrete compression damage evolution is presented in Figure 37. For tension behaviour, the post-peak stress-crack opening relation and cyclic unloading-reloading for concrete in the FE model was defined using the model proposed by Hordijk (1991). The envelope curve for the dynamic tension stress-crack opening relation is shown in Figure 38. Concrete tension damage evolution is presented in Figure 39.

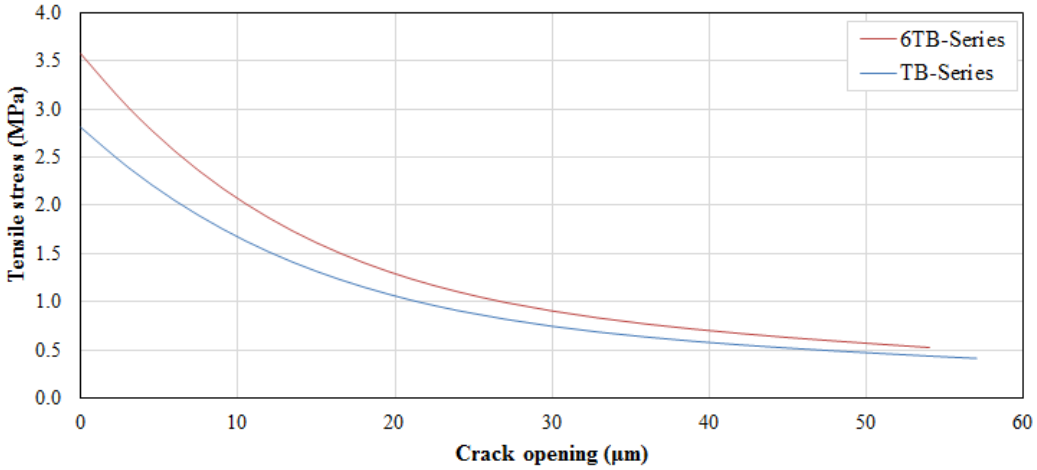

Figure 38: Dynamic tensile stress-strain relation for FE model

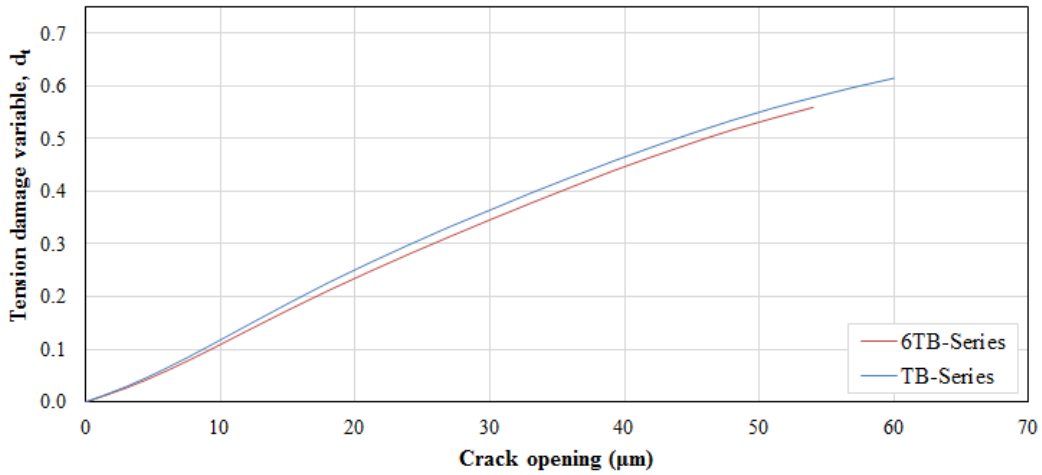

Figure 39: Evolution of concrete tension damage for FE model

A strain rate of 1/s was assumed when applying the expressions for the dynamic increase factors presented in Chapter 2 to the concrete material parameters. In the impact studies by Tang & Saadatmanesh (2003), it was found that the measured strain rates ranged from 0.8 to 1.4/s. Thus, the assumed strain rate used in the present study is a reasonable approximation.

However, the rate dependent behaviour is not considered automatically in the CPD and requires user-defined tension stiffening curves as a tabular function of cracking strain (or displacement) rate, and several compression hardening curves as a tabular function of inelastic strain rate. This complex approach is impractical and may result in convergence problems depending on the number of strain rate data ranges implemented in the model. Therefore, a simplified approach was adopted in the proposed FE model. Dynamic increase factors for a constant strain rate equal to that of the mid span section was assigned to all concrete elements for the duration of the analysis by updating the monotonic compression and tension stress-strain relations of the constitutive models.

Steel reinforcement

The Johnson and Cook rate-dependent yield plasticity model was used for reinforcement to account for the increase in yield stress with increasing strain rate. The material models for steel reinforcement used in the FE model are presented in Table 7.

Table 7: Material properties of steel reinforcement for FE Model

Diameter		(mm)	9.5
Yield strength	f_y	(MPa)	388
Strain at yield	ε_{sy}	(mm/m)	1.99
Ultimate strength	f_u	(MPa)	578.5
Strain at ultimate	ε_{su}	(mm/m)	187.8
Elastic modulus	E_s	(GPa)	193.4
Poisson´s ratio			0.3
Density	ρ	(kg/m^3)	7850
Johnson & Cook strain rate factor			0.0432

FRP-concrete bond interface

Contact between the bond interface and adjacent components was modelled with surface based tie constraints. Traction-separation behaviour of the interface is defined in terms of the model developed by Chen & Teng (2011), see section 3.3.4. The properties of the interfacial elements normal to the interface is assumed to behave linear-elastically with a stiffness of the adhesive layer. Following Chen & Teng (2011), the simplified FRP bond-slip (traction-separation) model developed by Lu et al (2005) was used to define the properties of the interfacial elements parallel to the interface. The traction-separation relation and damage evolution is presented in Figure 40 and 41, respectively.

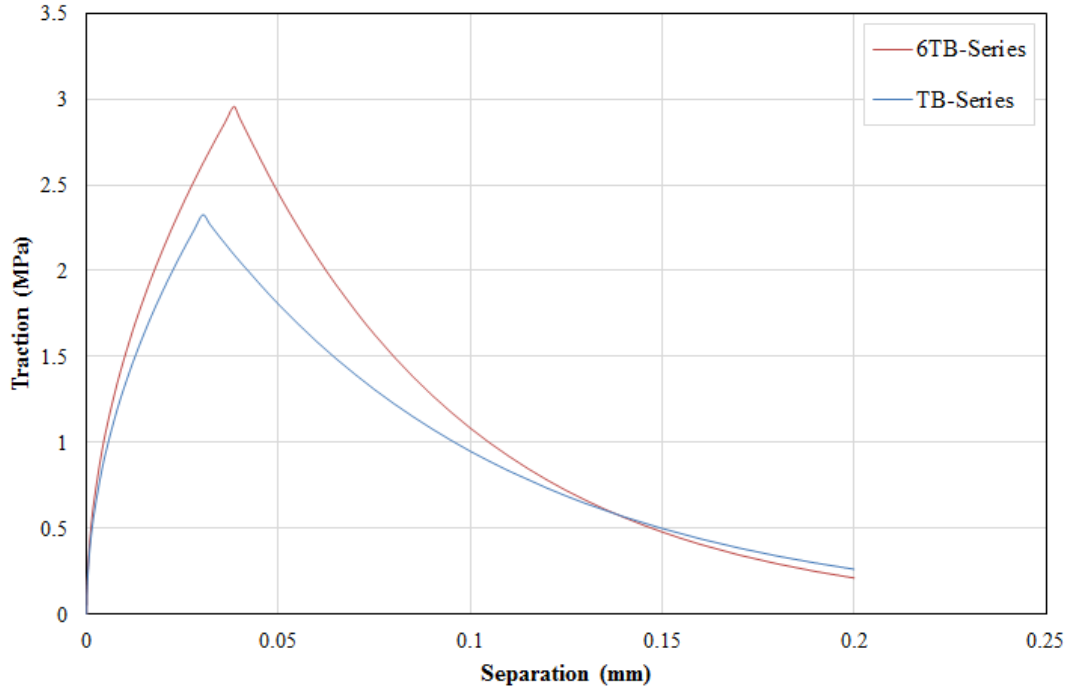

Figure 40: Traction-separation relation of FRP bond interface for FE model

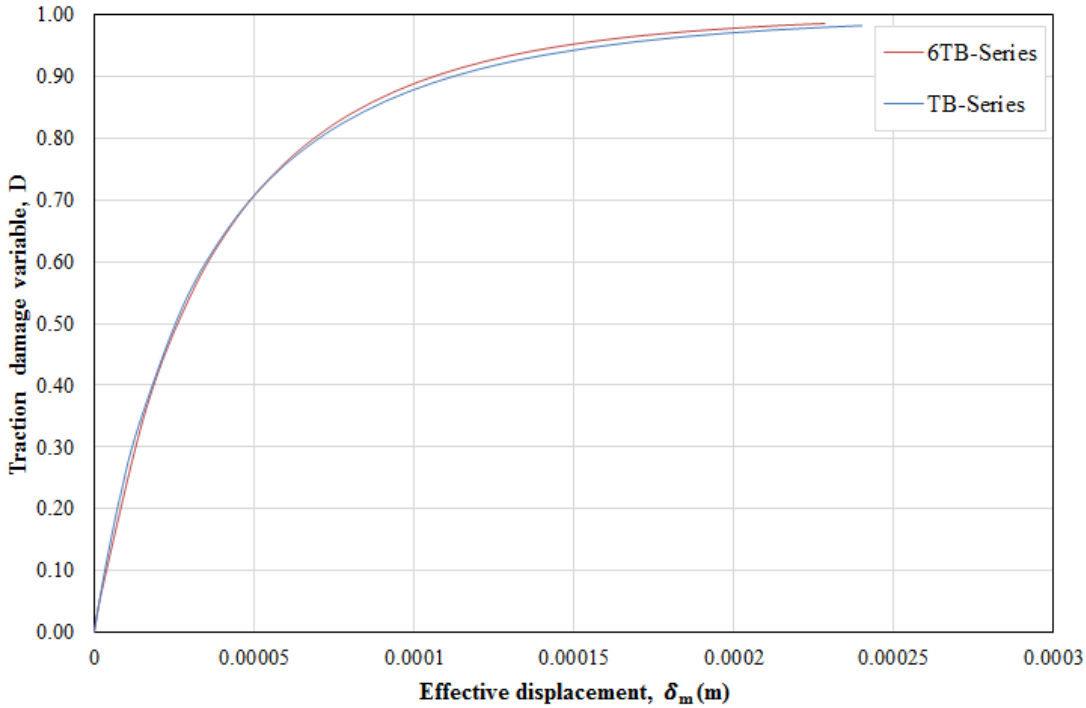

Figure 41: Evolution of traction damage of FRP bond interface for FE model

FRP

Material behaviour for the FRP was assumed linear-elastic with brittle failure at ultimate strain. Contact between the FRP and bond interface was modelled with surface based tie constraints. The material models for FRP used in the FE model are presented in Table 8.

Table 8: Material properties of FRP for FE Model

Beam identification	Composite	Weight (g/m^2)	Thickness (mm)	Ultimate strain	Tensile strength (MPa)	Tensile modulus (GPa)
6TB4R	Kevlar	85	0.13	0.021	288	13.2
6TB5R	Kevlar	307	0.43	0.019	388	19.2
TB1	Kevlar	307	0.43	0.014	1035	85.7
TB2	Carbon	599	0.67	0.017	460	37.6

Drop weight

Only a single impact event was considered in the FE model. Owing to the higher stiffness of steel compared to that of concrete, the steel drop weight is modelled as a rigid body. In Abaqus/Explicit, a rigid body is a collection of nodes and elements whose motion is governed by the motion of a single reference node. The rigid body definition is ideal for the modelling of very stiff components, as is the case with the drop weight in the present study, to improve computational efficiency. Rigid bodies do not affect the stability limit and element-level calculations are not performed for elements forming part of a rigid body definition, thereby resulting in faster analysis run times.

Translational degrees of freedom were set as free for the reference node, whereas all rotational degrees of freedom were constrained. Since only half of the beam specimen was modelled, only half of the total drop weight mass of 22.6 kg was assigned to the reference node. The material behaviour of the steel drop weight was assumed linear with an elastic modulus E_s of 200 GPa. The drop weight motion is governed by the velocity assigned to the reference node.

In order to save computational run-time, the initial velocity associated with each drop height was determined using the free-fall formula given by

$$v = \sqrt{2gh} \tag{4.1}$$

where h is the drop height. The corresponding contact velocities are 1.37 m/s and 1.52 m/s for the 6TB- and TB-series, respectively. The initial separation distance between the tip of the drop weight and the top surface of the RC beam was set at 1mm. The contact between the drop weight and the beam is modelled as a "hard" contact relationship, which is ideal in analyses involving large plastic deformations such as impact. The contact formulation is given by the surface-to-surface contact algorithm with the contact constraint enforcement provided by the penalty method.

4.4.3 Mass scaling

The stable time increment of the central difference algorithm employed in Abaqus/Explicit is governed by the relatively small element size of the FRP and FRP bond interface. To improve computational, the stable time increment (stability limit) was increased significantly by scaling the masses of these controlling elements. This was implemented by first computing the stable time increment of the TB-and 6TB-series beams without FRP strengthening applied; 1.28 x 10^{-6} seconds and 1.19 x 10^{-6} seconds respectively. Semi-automatic mass scaling was then implemented in the FE model by fixing the stable time increment of the element set containing the FRP and FRP bond interface elements to the aforementioned values.

4.5 Summary

This chapter dealt with the development of a FE model to simulate the dynamic response of FRP strengthened RC beams subjected to impact loading. An important step in this research was the incorporation of strain rate depended constitutive material models and FRP bond interface models.

The nonlinear behaviour of the concrete beam under reversed cyclic loading due to impact was defined based on the constitutive models by Aslani and Jowkarmeimandi (2012) and Hordijk (1991). Strain rate dependent material behaviour was accounted for by updating the parameters of the monotonic compression and tension stress-strain relations derived from the constitutive models, based on the dynamic increase factors presented in CEB Model Code 2010 (CEB-FIP, 2010). FRP interfacial bond behaviour was modelled using the the simplified FRP traction-separation model developed by Lu et al (2005). The FE model developed was verified by applying it to selected test specimens in the experimental impact studies by Tang (2002) and Tang & Saadatmanesh (2003).

The next chapter discusses the results of the FE analysis and its comparison with the observed results by Tang (2002) and Tang & Saadatmanesh (2003). Key parameters used for comparison purposes include mid span displacement and support reaction force time histories, as well as concrete crack patterns.

5 RESULTS AND DISCUSSION

This chapter presents the results of the proposed FE model outlined Chapter 4, as well as the analysis and discussion thereof. The capability and accuracy of the proposed FE model is demonstrated through comparisons of its predictions with test results of experimental impact studies by Tang (2002) and Tang & Saadatmanesh (2003). Measured displacement and reaction force time histories as well as crack patterns obtained from the impact tests are compared with the results of the FE model.

5.1 Mid span displacement time history

The following figures present the comparison of mid span displacements, as observed from impact tests by Tang (2002) and Tang & Saadatmanesh (2003), and computed with the proposed FE model. Comparison of peak displacements are summarised in Table 9. Frequencies for the first and second deflection cycle are presented in Table 10.

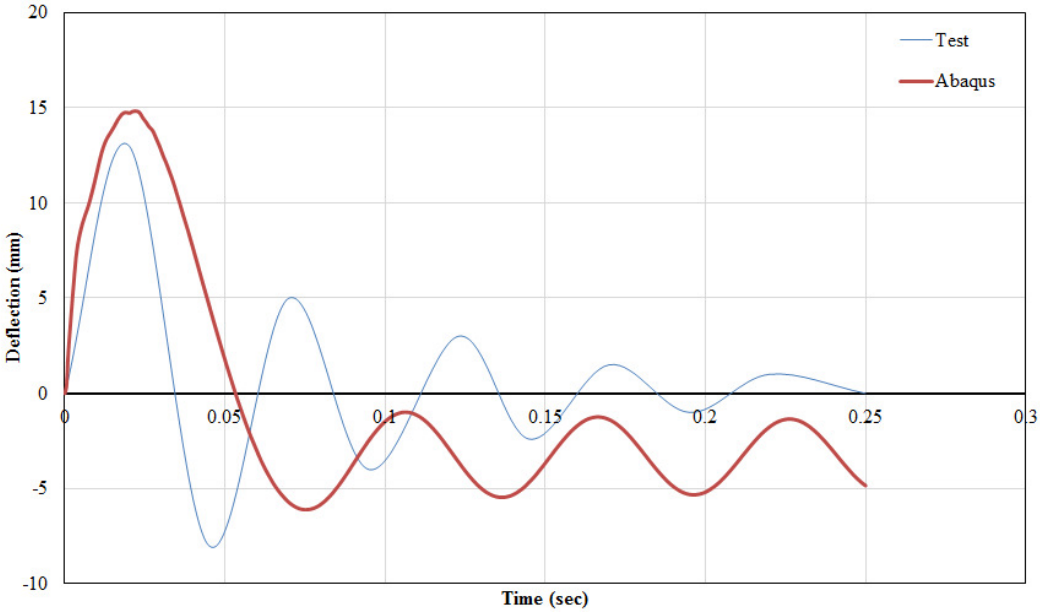

Figure 42: Comparison of mid span displacement time history of TB1 beam

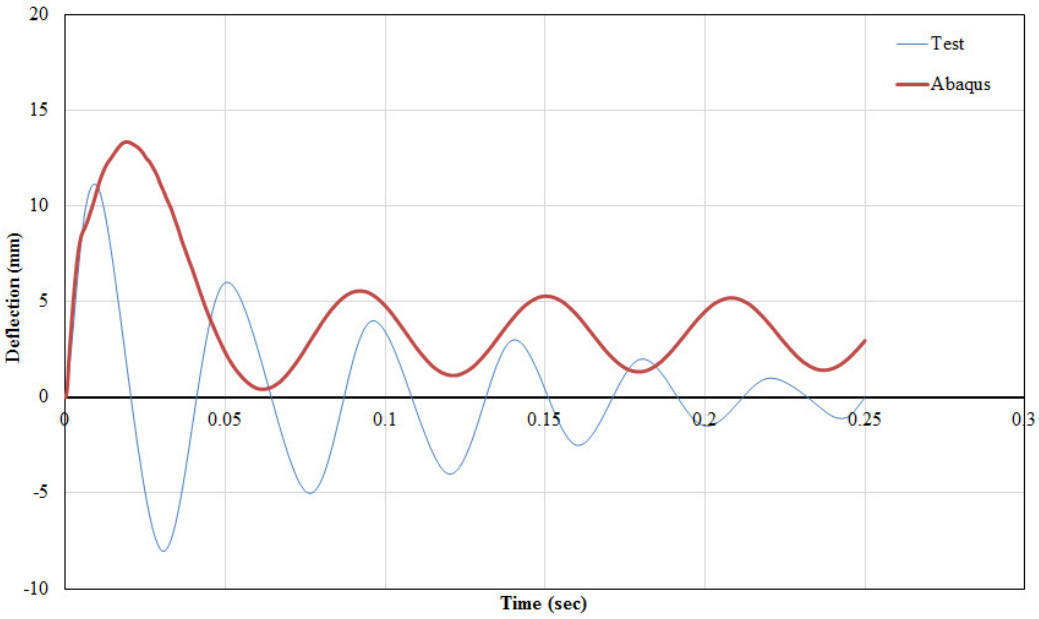

Figure 43: Comparison of mid span displacement time history of TB2 beam

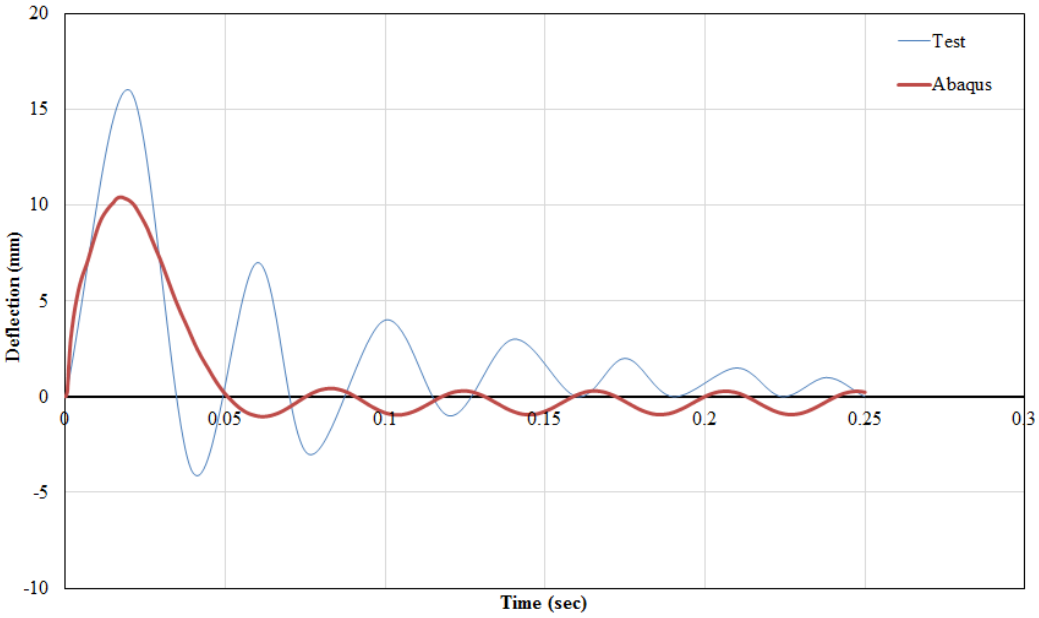

Figure 44: Comparison of mid span displacement time history of 6TB4r beam

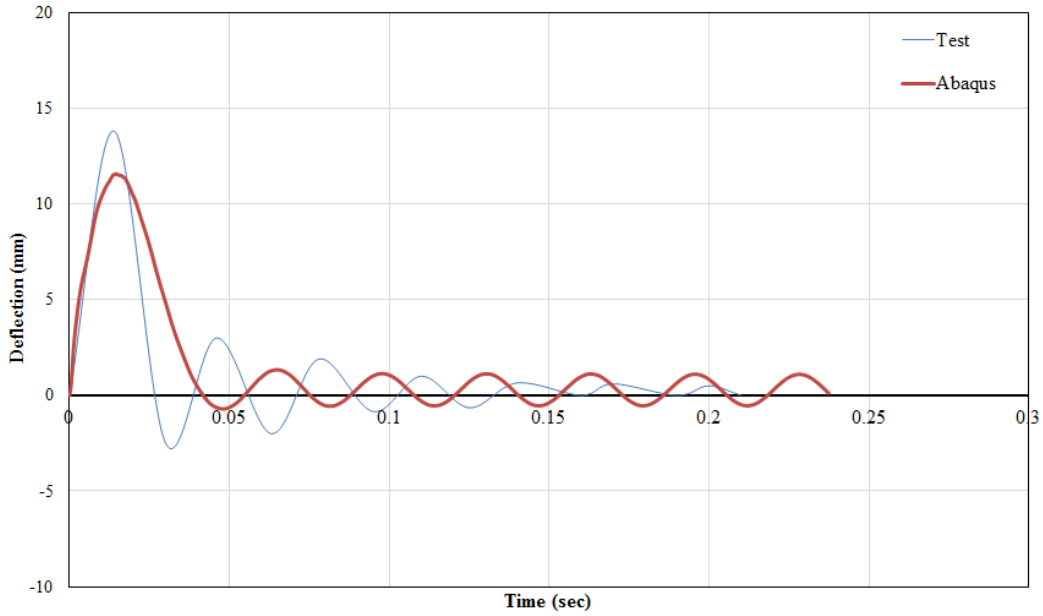

Figure 45: Comparison of mid span displacement time history of 6TB5r beam

Table 9: Summary of peak displacements as obtained from tests and FE Model

Beam identification	Peak displacements (mm)		Error (%)
	Test	FE Model	
TB1	13.1	14.8	13
TB2	11.2	13.3	19
6TB4R	16.1	10.4	35
6TB5R	13.8	11.6	16

Table 10: Frequencies for 1st and 2nd deflection cycle as obtained from tests and FE Model

Beam identification	*1st cyclic frequency (Hz)*		Error (%)	*2nd cyclic frequency (Hz)*		Error (%)
	Test	FE Model		Test	FE Model	
TB1	17	11	36%	19	16	13%
TB2	25	13	49%	22	18	19%
6TB4R	19	14	27%	25	24	2%
6TB5R	25	18	29%	32	29	9%

Figures 42 to 45 show the observed and computed deflection time histories for beams TB1, TB2, 6TB4r and 6TB5r, respectively. In comparing these figures, it is shown that for the FE model the maximum deflections of the TB-series are larger than that of the 6TB-series, whereas the vibration frequencies of the 6TB-series are higher than those of the TB-series. These differences are attributable to the higher impact height used for the TB-series beams.

The vibration frequencies for beams TB2 and 6TB5r is higher by as much as 40% than that of beams TB1 and 6TB4r, respectively. For a given drop height, beam specimens strengthened with the stiffer laminate exhibits a less ductile response.

From the preceding figures, it is noted that some discrepancies exists between the FE model and the impact test results. The FE model overestimated the peak displacements for the TB-series specimens, whereas peak displacements for the 6TB-series specimens were underestimated. The maximum discrepancy was 19% for the TB-series, whilst a maximum error of 35% was recorded for the 6TB-series. However, the error reported for beam 6TB4r falls outside the error range of 13% to 19% for the results of the other beams. This is indicative of discrepancies in the experimental study.

Furthermore, the post-peak displacement time history also showed discrepancies. Typically, the FE model underestimated the frequencies of the first deflection cycle in all tests. However, for subsequent deflection cycles, the FE model response showed a closer correlation with observed deflections cycles. For instance, for the predicted frequencies of the second deflection cycle, the maximum discrepancy was 9% and 19% for the TB-series and TB-series, respectively.

The peak dynamic response depends on stress wave propagation during a short period after impact (Fujikake et al, 2009). Therefore, discrepancies in the peak response are attributable to the idealisation of the test apparatus in the FE model. Since the FE model is an idealisation of the real test apparatus, it is not possible, nor practical, to replicate inherent irregularities in the real system relating to variations in support stiffness, variations in contact properties between drop weight and beam, uneven contact of drop weight, and uneven contact of the support rollers with the test

specimen. Furthermore, as is the case in the present study, assumptions required in developing the FE model in the absence of detailed information on the test setup introduces further simplification of the real test apparatus. In this context, with the exception of beam 6TB4r, discrepancies in the peak response are negligible considering that the maximum absolute difference between observed and computed peak deflection is 2.2 mm for the remaining beams. Thus, the reported discrepancies are within an acceptable range.

The post-peak dynamic response depends on the elastic-plastic dynamic behaviour of constituent materials and the loading rate effect (Fujikake et al, 2009). Therefore, discrepancies in the post-peak response are attributable to the idealisation of concrete hysteresis models, accounting for strain rate effects, used in the FE model. Realistic concrete hysteresis models are critical in the effective computational analyses of the cyclic response of concrete elements. However, most concrete hysteresis models, such as the model used in the present study, were developed under quasistatic cyclic loading conditions. Therefore, in the case of high strain rates such as impact, it is expected that the use of these models would generate some errors in the FE analyses. Also, the concrete hysteresis model used in the proposed FE model only accounts for full unloading-reloading responses in the CDP framework. By default, the CPD model in Abaqus/Explicit does not allow for stiffness degradation under partial unloading-reloading conditions and the definition of crack closing models. The development of a user subroutine VUMAT in Abaqus/Explicit, a FORTRAN code based utility, to define these aspects in Abaqus/Explicit is outside the scope of the present study.

Furthermore, assumptions in formulating the strain rate effects in the FE model also affect the accuracy of the simulation. In the FE model, dynamic increase factors for a constant strain rate equal to that of the mid span section was assigned to all concrete elements for the duration of the analysis in light of the limitations of the Abaqus/Explicit CDP model, discussed in section 4.4.2. However, strain rates changes rapidly throughout the length of the specimen during an impact-induced vibration (Saatci, 2007).

5.2 Reaction force time history

The following figures present the comparison of support reaction forces, as observed from impact tests and computed with the proposed FE model. Comparison of reaction force are summarised in Table 11. Frequencies for the first and second force cycle are presented in Table 12 for the TB-series only since detailed reaction time history for the 6TB-series was not captured in the impact experiments.

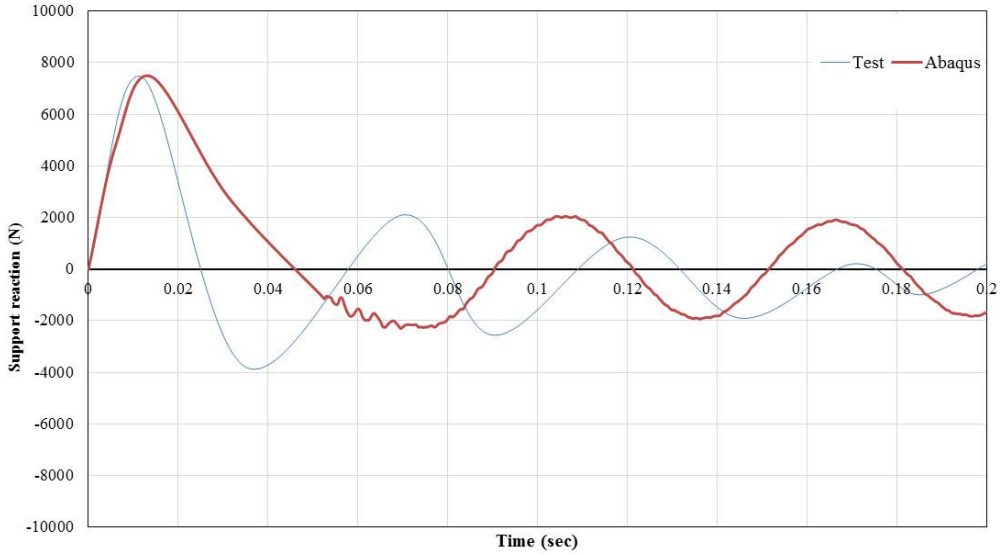

Figure 46: Comparison of reaction force time history of TB1 beam

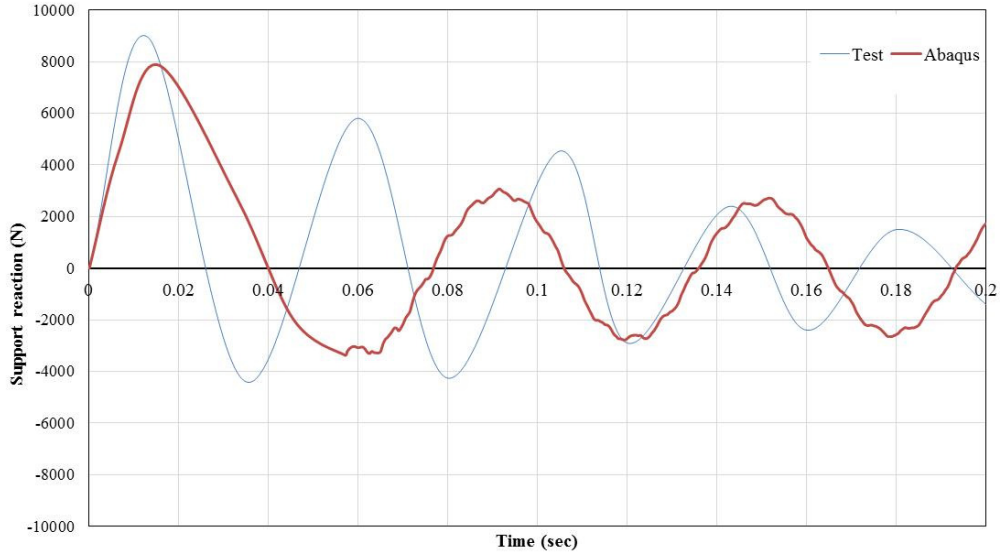

Figure 47: Comparison of reaction force time history of TB2 beam

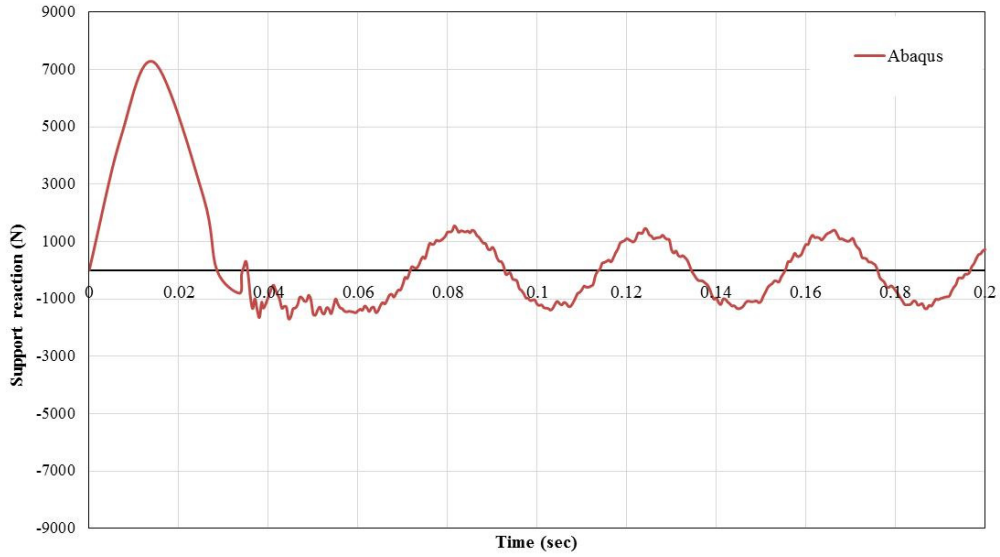

Figure 48: Reaction force time history of 6TB4r beam

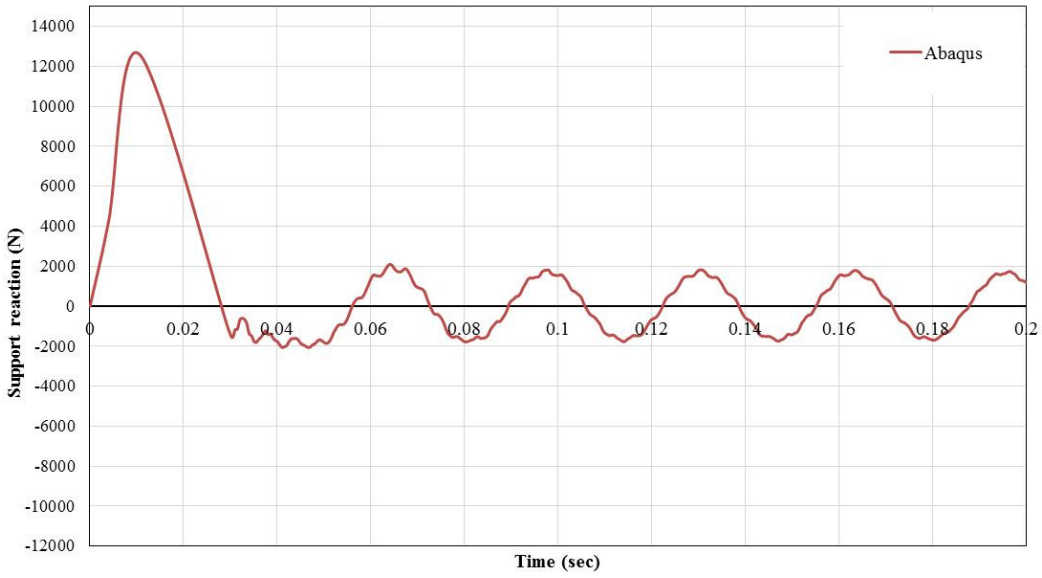

Figure 49: Reaction force time history of 6TB5r beam

Table 11: Summary of support reactions as obtained from tests and FE Model

Beam identification	Support reactions (N)		Error (%)
	Test	FE Model	
TB1	7427	7244	2%
TB2	9346	7861	16%
6TB4R	14283	7344	49%
6TB5R	14953	12657	15%

Table 12: Frequencies for 1st and 2nd reaction force cycle for TB-series as obtained from tests and FE Model

Beam identification	*1st cyclic frequency (Hz)*		Error (%)	*2nd cyclic frequency (Hz)*		Error (%)
	Test	FE Model		Test	FE Model	
TB1	18	11	40%	19	16	16%
TB2	22	14	30%	20	17	15%

Figures 46 to 49 show the observed and computed reaction force time histories for beams TB1, TB2, 6TB4r and 6TB5r, respectively. With the exception of outlier beam 6TB4r, the maximum reaction force of the FE models compared favourably with observed values. For the same drop height, the observed reaction force and frequency for beam TB2 is greater than that of beam TB1 since the Kevlar FRP used in TB2 is stiffer than the Carbon FRP used in TB1.

From the preceding figures, it is noted that some discrepancies exists between the FE model and the impact test results. In general, the FE model underestimated the peak reaction force. The maximum discrepancy was 16% for the TB-series, whilst a maximum error of 49% was noted for the 6TB-series. The error reported for beam 6TB4r falls outside the error range of 2% to 16% for the results of the other beams. This is indicative of discrepancies in the experimental study.

Furthermore, the post-peak reaction force time history also showed discrepancies. As with the earlier comparison with deflections, the FE model underestimated the frequencies of the first reaction cycle in all tests. However, for subsequent reaction cycles, the FE model response compared favourably with observed post-peak cycles. For instance, for the predicted frequencies of the second reaction cycle, the maximum discrepancy was 16% for the TB-series.

Discrepancies in the overall reaction force response are more likely to be attributable to the idealisation of the test apparatus in the FE model rather than material constitutive relations. In the test setup, the supports were configured to allow support rotation whilst preventing beam uplift after rebound. Available data of this support layout is inadequate to allow for its detailed representation in the FE model. In the absence of sufficient data, the support was modelled as a simple support with vertical displacements constrained. Although this simplification provides uplift restraint, it does not consider the complex friction interface between the roller pins, supporting plates and beam specimen that provides some horizontal restraint during impact response cycles. Hence, the absence of this clamp restraint in the supports defined in the FE model results in a more ductile global response thereby softening the reaction force time history.

5.3 Damage evolution and crack patterns

The following figures present the distribution of the damage variable in the FRP interface and the concrete beam for a single impact event. The literature used for comparison only provides images of the beam crack patterns at failure following several impact events. Therefore, it was not reported in this study. However, comparisons were drawn between the observed and computed crack patterns based on descriptions provided in the reference text of the experimental impact studies by Tang (2002) and Tang & Saadatmanesh (2003).

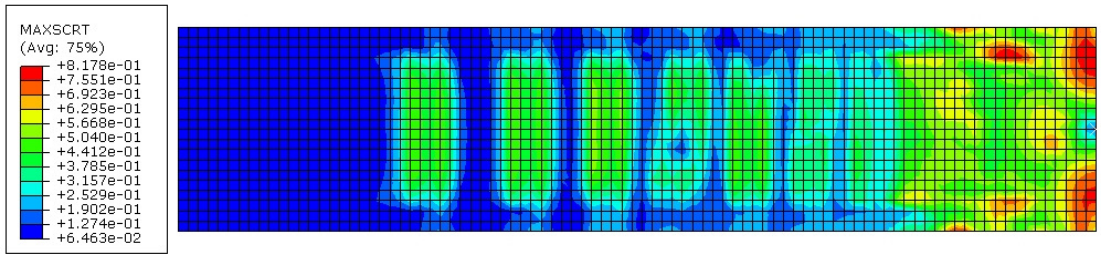

(a)

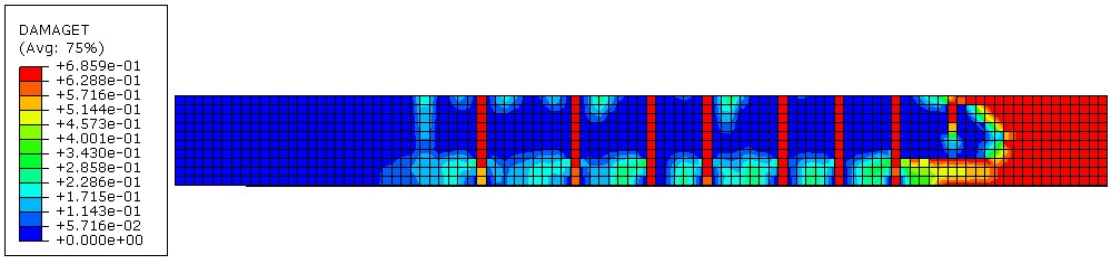

(b)

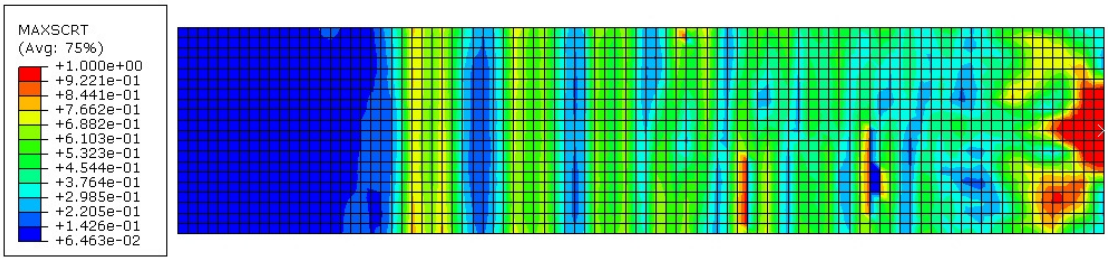

(c)

Figure 50: Damage evolution of (a) Bottom bond interface (plan view);(b) Concrete (side view); and (c) Top bond interface (plan view) of TB1 beam

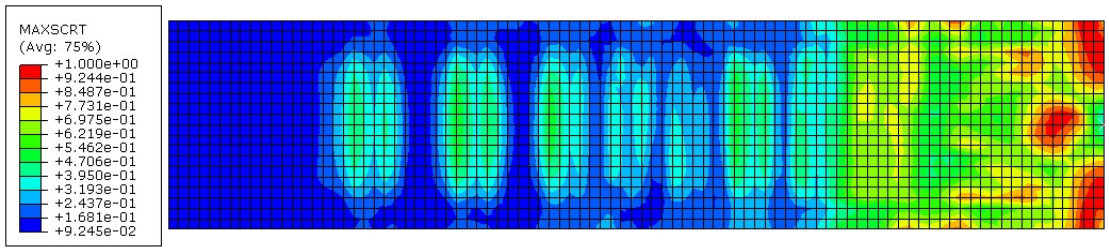

(a)

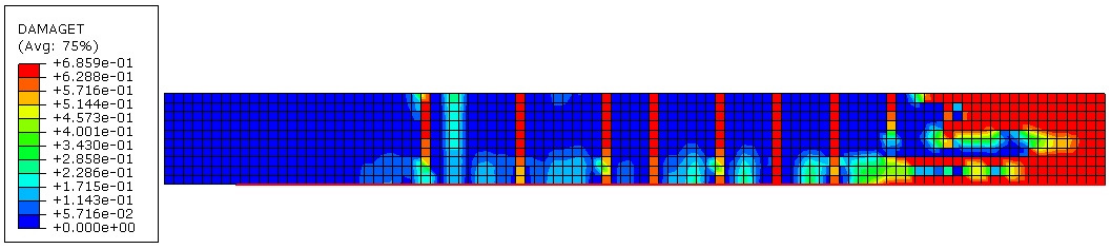

(b)

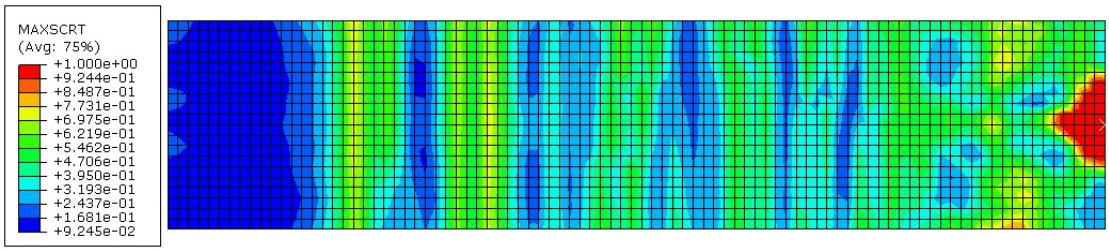

(c)

Figure 51: Damage evolution of (a) Bottom bond interface (plan view);(b) Concrete (side view); and (c) Top bond interface (plan view) of TB2 beam

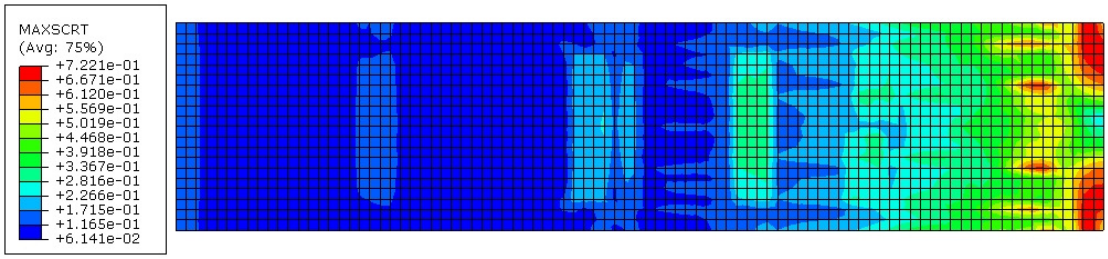

(a)

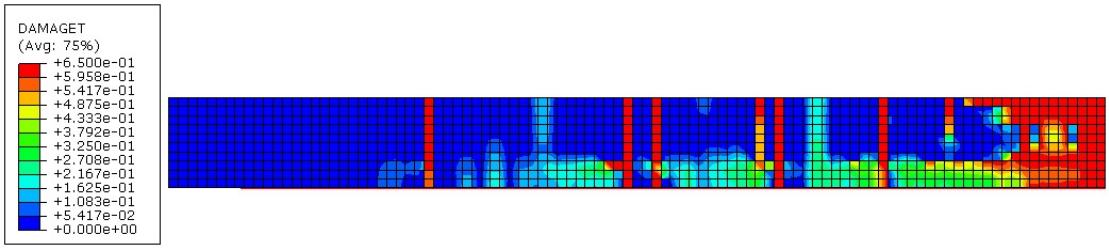

(b)

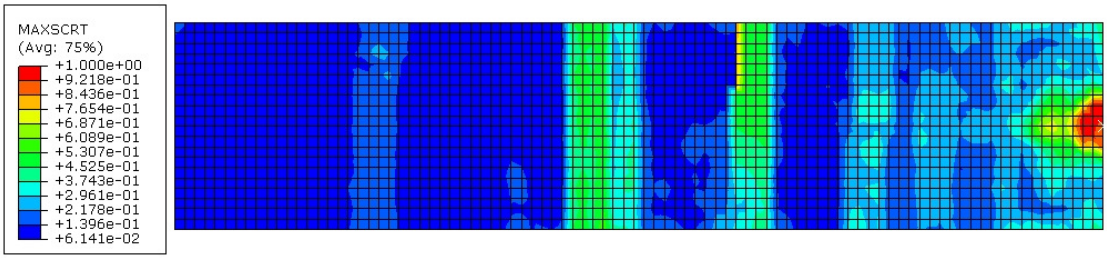

(c)

Figure 52: Damage evolution of (a) Bottom bond interface (plan view);(b) Concrete (side view); and (c) Top bond interface (plan view) of 6TB4R beam

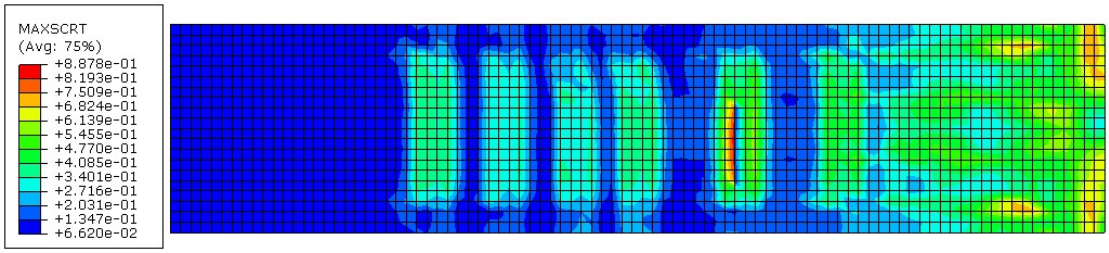

(a)

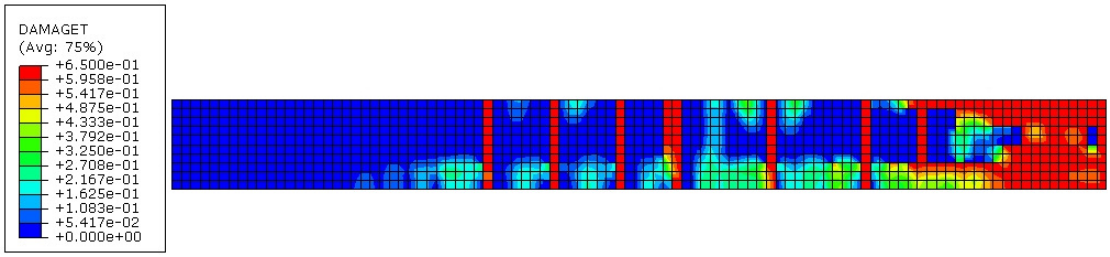

(b)

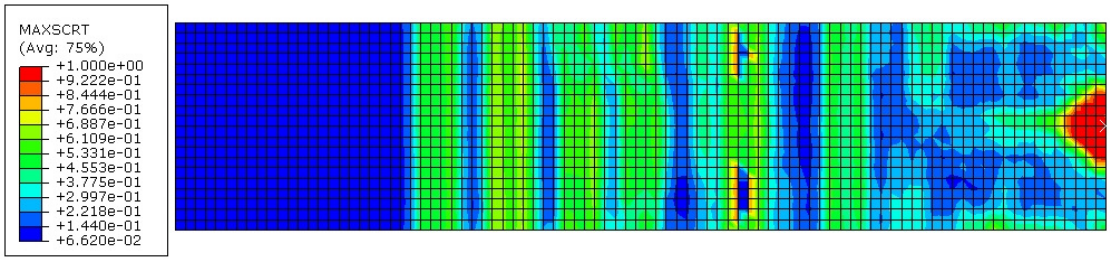

(c)

Figure 53: Damage evolution of (a) Bottom bond interface (plan view);(b) Concrete (side view); and (c) Top bond interface (plan view) of 6TB5R beam

Figures 50 to 53 compares the observed crack pattern with the computed distribution of damage for concrete and the FRP bond interface for TB1, TB2, 6TB4r and 6TB5r, respectively.

The CDP model in Abaqus/Explicit does not have the notion of cracks developing at integration points; however, several options are available to obtain an approximation for the graphical visualisation of the crack patterns in concrete. In one option,

cracking is assumed to initiate at points where the equivalent plastic strain is greater than zero. Alternatively, the distribution of the tension damage variable may be used to approximate crack formation. The latter approach was used in this study.

From a comparison of the observed and computed crack distributions, the following observations were made:

i) Shear crack formation was not shown in the computed damage distribution for concrete for the single impact event simulated. This is consistent with test observations where shear cracks only appeared after four successive impacts from a drop height of 1.37 m in the case of the 6TB-series, and three successive impacts from a drop height of 1.52 m in the case of the TB-series.

ii) Furthermore, flexural crack formations in the FE model were mostly distributed over quarter span on either side of the impact zone. Again, this is consistent with test observations.

iii) Comparison of the computed damage distribution between beams TB1 and TB2, shows that the stiffer carbon composite used in TB1 reduced the number and relative size of flexural cracks.

iv) The FRP interface remained intact after the single impact event simulated. This is consistent with test observations where FRP debonding failure did not occur. In all cases, the damage distribution of the FRP interface outside of the impact zone is greatest between approximated crack planes. This is indicative of the development of intermediate crack-induced interfacial debonding expected in regions of stress concentrations adjacent to cracks in the concrete.

6 CONCLUSIONS AND RECOMMENDATIONS

The main objective of this study was to develop and verify a numerical model based on the finite element (FE) approach, capable of describing the dynamic response of FRP strengthened beams subjected to low velocity impact by accounting for FRP interfacial bond behaviour and dynamic properties of constituent materials at high strain rates.

The FE model was developed in Abaqus/Explicit version 6.10. To account sufficiently for the effects of inertia and the nonlinear behaviour of concrete and steel, a three-dimensional analysis was adopted. A mesh seed of 10mm was used throughout the model. In order to save computational run-time, semi-automatic mass scaling was employed and the drop weight was modelled as a rigid body. Furthermore, the rigid body was offset 1mm away from the beam impact zone with the initial contact velocity associated with a given drop height determined using the free-fall formula . Only a single impact event was considered.

The capability and accuracy of the proposed FE model was demonstrated through comparisons of its predictions with test results of experimental impact studies by Tang (2002) and Tang & Saadatmanesh (2003). The following conclusions were reached after comparing the results of the FE model with the test results:

a) For a given drop height, beam specimens strengthened with the stiffer laminate exhibits a less ductile deflection response, and the observed reaction force and frequency increases with laminate stiffness. Furthermore, the use of stiffer laminates reduced the number and relative size of flexural cracks.

b) Peak support reactions predicted with the FE model showed strong agreement with the test values, with the exception of beam 6TB4r. However, the comparison of post-peak reaction time histories showed some discrepancies the most likely cause relating to the simplification of support conditions in the FE model.

c) Peak displacements obtained from the FE model showed reasonable agreement with the test values, with the exception of beam 6TB4r. A maximum absolute difference of 2.2 mm between observed and computed peak deflection was noted for the remaining beams. The observed discrepancies in the peak response are attributable to the idealisation of the test apparatus in the FE model.

d) Displacement and reaction cycle frequencies obtained from the FE model showed reasonable agreement with the test values, with the exception of beam 6TB4r. Typically, the FE model underestimated the frequencies of the first deflection cycle in all tests. However, for subsequent cycles, the FE model response showed a closer correlation with observed cycles. Discrepancies in the post-peak responses are attributable to the idealisation of the concrete hysteresis model, strain rate effects and test apparatus in the FE model.

e) Although the FE model cannot represent actual crack patterns, it provides a reasonable representation of the induced damage, as it reflected the flexural crack distribution and lack of shear crack formation observed in the tests. Furthermore, it provides a reasonable representation of the development of intermediate crack-induced interfacial debonding in the FRP bond interface.

v) The FE model captured the development of intermediate crack-induced interfacial debonding zones expected in regions of stress concentrations adjacent to cracks in the concrete.

The FE model provides reasonably accurate predictions for the dynamic response of FRP strengthened beams subjected to low-velocity impact loading. However, the discrepancies between the observed and computed response highlights the need for further refinement of the FE model. The following recommendations for further work are put forward:

i) Development of a comprehensive concrete hysteresis model, that considers varying strain rates, within the CDP framework. The model should be implemented in Abaqus/Explicit with a user subroutine VUMAT accounting for full and partial loading-unloading in uniaxial cyclic tension and compression.

This should provide a more accurate model capable of reproducing the complex behaviour of concrete.

ii) Experimental investigations to determine the parameters of the CDP for FE analysed beams. For example, typical laboratory tests should include:

   a) Uniaxial compression tests
   b) Uniaxial tension tests
   c) Biaxial failure in plane state of stress
   d) Triaxial test of concrete

iii) Verification of proposed FE-model based on a wider spectrum of experimental results. The parametric study should include various beam geometries, boundary conditions, FRP strengthening schemes, FRP types, impact energies and concrete grades.

iv) Define the traction-separation response of the FRP-bond interface layer at strain rates of upto 10^2 s^{-1} for application in both low and high velocity impact studies.

v) Modelling the bond interface between steel reinforcement and concrete using appropriate bond-slip models. The models should be valid for strain rates of upto 10^2 s^{-1} for application in both low and high velocity impact studies.

vi) Investigate the application of the extended finite element method (XFEM) for a more accurate representation of crack initiation and propagation in concrete under impact loading and, hence, IC debonding of the FRP.

vii) Investigate alternative ways to model the support condition

7 REFERENCES

Abaqus. (2010). *User's Manual.* Dassault Systemes Simulia Corp: Providence, RI, USA.

Abrate, S. (1991). Impact of composite laminates. *Applied Mechanics Reviews, 44*(4), 155-190.

Abrate, S. (1994). Impact of laminated composites: recent advances. *Applied Mechanics Reviews, 47*(11), 517-544.

Abrate, S. (1997). Localised impact on sandwich strucutres with laminated facings. *Applied Mechanics Reviews, 50*(2), 69-82.

Abrate, S. (1998). *Impact on composite structures.* New York: Cambridge University Press.

Abrate, S. (2011). *Impact Engineering of Composite Structures: CISM Courses and Lectures* (Vol. 526). Italy: SpringerWienNewYork.

Abu-Lebdeh, T., Hamoush, H., Choi, W., & Al Nasra, M. (2011). High rate-dependent interaction diagrams for reinforced concrete columns. *American Journal of Engineering and Applied Sciences, 4*(1), 1-9.

ACI. (1996). *State-of-the-Art Report on Fiber Reinforced Plastic (FRP) Reinforcement for Concrete Structures, ACI 440R-96 (Reapproved 2002).* Farmington Hills: American Concrete Institute.

ACI. (2002). *Guide for the Design and Construction of Externally Bonded FRP Systems for Strengthening Concrete Structures, ACI440.2R-02.* Farmington Hills: American Concrete Institute.

Arya, C., Clarke, J. L., Kay, E. A., & O'Regan, P. D. (2002). TR 55: Design guidelines for strengthening concrete structures using fibre composite materials: a review. *Engineering Structures, 24*, 889-900.

Aslani, F., & Jowkarmeimandi, R. (2012). Stress-strain model for concrete under cyclic loading. *Magazine of Concrete Research, 64*(8), 673-685.

Bahn, B. Y., & Hsu, T. C. (1998). Stress-strain behavior of concrete under cycling loading. *ACI Material Journal, 95*(2), 178-193.

Barpi, F. (2004). Impact behaviour of concrete: a computational approach. *Engineering Fracture Mechanics, 71*, 2197-2213.

Biggs, J. M. (1964). *Introduction to structural dynamics.* New York: McGraw-Hill.

Bischoff, P. H., & Perry, S. H. (1991). Compressive behaviour of concrete at high strain rates. *Materials and Structures, 24*, 425-450.

Bonacci, J. F., & Maalej, M. (2000). Externally bonded FRP for service-life extension of RC infrastructure. *Journal of Infrastructure systems, 6*, 41-51.

Bousselham, A., & Chaallal, O. (2004). Shear Strengthening Reinforced Concrete Beams with Fiber-Reinforced Polymer: Assessment of Influencing Parameters and Required Research. *ACI Structural Journal, 101*(2), 219-227.

Brara, A., & Klepaczko, J. R. (2006). Experimental characterization of concrete in dynamic tension. *Mechanics of Materials, 38*, 253-267.

Buyukozturk, O., & Hearing, B. (1998). Failure behavior of precracked concrete beams retrofitted with FRP. *Journal of Composites for Construction, 2*, 138-144.

Buyukozturk, O., Gunes, O., & Karaca, E. (2004). Progress on understanding debonding problems in reinforced concrete and steel members strengthened using FRP composites. *Construction and Building Materials, 18*, 9-19.

Cantwell, W. J., & Morton, J. (1991). The impact resistance of composite materials - a review. *Composites, 22*(5), 347-362.

Capozucca, R., & Nilde Cerri, M. (2002). Static and dynamic behaviour of RC beam model strengthened by CFRP-sheets. *Construction and Building Materials, 16*, 91-99.

CEB. (1996). *RC elements under cyclic loading: State of the art report.* London: Thomas Telford.

CEB-FIP. (1993). *CEB-FIP Model Code 90.* London: Thomas Telford.

CEB-FIP. (1999). *Structural concrete: Textbook on behaviour, design and performance - Volume 1.* Lausanne: International Federation of Structural Concrete.

CEB-FIP. (2010). *Model Code 2010: First Complete Draft - Volume 1.* Lausanne: International Federation of Structural Concrete.

Ceci, A. M., Casas, J. R., & Ghosn, M. (2012). Statistical analysis of existing models for flexural strengthening of concrete bridge beams using FRP sheets. *Construction and Building Materials, 27*(1), 490-520.

Ceroni, F. (2010). Experimental performance of RC beams strengthened with FRP materials. *Construction and Building Materials, 24*, 1547-1559.

Chajes, M. J., Thomson Jr., T. A., Januszka, T. F., & Finch Jr., W. W. (1994). Flexural strengthening of concrete beams using extrnally bonded composite materials. *Construction and Building Materials, 8*(3), 191-201.

Chang, G. A., & Mander, J. B. (1994). *Seismic energy based fatigue damage analysis of bridge columns. Part 1: Evaluation of seismic capacity.* New York: State University of New York. Technical report NCEER-94-0006.

Chen, G. M., & Teng, J. G. (2011). Finite-element modeling of intermediate crack debonding in FRP-plated RC beams. *Journal of composites for construction, 15*, 339-353.

Chen, J. F., & Teng, J. G. (2003a). Shear capacity of fiber-reinforced polymer-strengthened reinforced concrete beams: fiber reinforced polymer rupture. *Journal of Structural Engineering, 129*, 615-625.

Chen, J. F., & Teng, J. G. (2003b). Shear capacity of FRP-strengthened RC beams: FRP debonding. *Construction and Building Materials, 17*, 27-41.

Clough, R. W., & Penzien, J. (2003). *Dynamics of structures* (3rd ed.). Berkeley: Computers & Structures, Inc.

Cook, R. D., Malkus, D. S., & E., P. M. (1989). *Concepts and applications of finite element analysis* (3rd Edition ed.). New York: John Wiley & Sons.

Cotsovos, D. M., & Pavlovic, M. N. (2008). Numerical investigation of concrete subjected to compressive impact loading. Part 2: Parametric investigation of factors affecting behaviour at high loading rates. *Computers and Structures, 86*, 164-180.

CRC Construction Innovation. (2002). *Review of strengthening techniques using externally bonded fiber reinforced polymer composites.* Brisbane: CRC for Construction Innovation.

Cusatis, G. (2011). Strain-rate effects on concrete behavior. *International Journal of Impact Engineering, 38*, 162-170.

Desai, C. S., & Siriwardane, H. J. (1984). *Constitutive laws for engineering materials with emphasis on geologic materials.* New Jersey: Prentice-Hall.

Elmorsi, M. K., & Tso, W. K. (1998). Nonlinear analysis of cyclically loaded reinforced concrete structures. *ACI Structural Journal, 95*(6), 725-739.

Erki, M. A., & Meier, U. (1999). Impact loading of concrete beams externally strengthened with CFRP laminates. *Journal of Composites for Construction, 3*, 117-124.

FIB. (2001). *Externally bonded FRP reinforcement for RC structures, Technical Report, Task Group 9.3, Bulletin No. 14.* Lausanne, Switzerland: The International Federation of Structural Engineers.

Fu, H. C., Erki, M. A., & Seckin, M. (1991). Review of effecs of loading rate on reinforced concrete. *Journal of Structural Engineering, 117*, 3660-3679.

Fujikake, K., Li, B., & Soeun, S. (2009). Impact response of reinforced concrete beam and its analytical evaluation. *Journal of structural engineering, 135*(8), 938-950.

Gary, G., & Bailly, P. (1998). Behaviour of quasi-brittle material at high strain rate. Experiment and modelling. *European Journal of Mechanics - A/Solids, 17*(3), 403-420.

Georgin, J. F., & Reynouard, J. M. (2003). Modeling of structures subjected to impact: concrete behaviour under high strain rate. *Cement and Concrete Composites, 25*, 131-143.

Grote, D. L., Park, S. W., & Zhou, M. (2001). Dynamic behavior of concrete at high strain rates and pressures: I. experimental characterization. *International Journal of Impact Engineering, 25*, 869-886.

Gylltoft, K. (1984). Fracture mechanics model for fatigue in concrete. *RILEM Materials and Structures, 17*(97), 55-58.

Hamed, E., & Rabinovitch, O. (2005). Dynamic behavior of reinforced concrete beams strengthened with composite materials. *Journal of Composites for Construction, 9*, 429-440.

Hamed, E., & Rabinovitch, O. (2007). Damping and viscoelastic dynamic response of RC flexural members strengthened with adhesively bonded composite materials. *Journal of Engineering Mechanics, 133*, 1278-1289.

Hentz, S., Donze, F., & Daudeville, L. (2004). Discrete element modelling of concrete submitted to dynamic loading at high strain rates. *Computers and structures, 82*, 2509-2524.

Hilber, H. M., Hughes, T. J., & Taylor, R. L. (1977). Improved numerical dissipation for time integration algorithms in structural dynamics. *Earthquake Engineering and Structural Dynamics, 5*, 283-292.

Hillerborg, A., Modeer, M., & Petersson, P. E. (1976). Analysis of crack formation and crack growth in concrete by means of fracture mechanics and finite element. *Cement and Concrete Research, 6*(6), 773-782.

Hollaway, L. C. (2010). A review of the present and future utilisation of FRP composites in the civil infrastructure with reference to their important in-service properties. *Construction and Building Materials, 24*, 2419-2445.

Hollaway, L. C., & Head, P. R. (2001). *Advanced Polymer Composites and Polymers in the Civil Infrastructure.* Oxford: Elsevier.

Hollaway, L. C.; Teng, J. G. Eds. (2008). *Strengthening and rehabilitation of civil infrastructures using fibre-reinforced polymer (FRP) composites.* Cambridge: Woodhead.

Hordijk, D. A. (1991). *Local approach to fatigue of concrete.* Delft: The Delft University of Technology.

Hutton, D. H. (2004). *Fundamentals of finite element analysis.* New York: McGraw-Hill.

Institute of Civil Engineers. (2008). *ICE Manual of bridge engineering* (2nd ed.). (G. Parke, & N. Hewson, Eds.) London: Thomas Telford.

Jankowiak, T., & Lodygowski, T. (2005). *Identification of paramters of concrete damage plasticity constitutive model.* Poznan, Poland: Poznan University of Technology.

Jerome, D. M. (1996). *Dynamic response of concrete beams externally reinforced with carbon fiber reinforced plastic. Ph.D. Thesis.* University of Florida: Gainesville, Florida.

Jiang, H., Wang, X., & He, S. (2012). Numerical simulation of impact tests on reinforced concrete beams. *Materials and Design, 39*, 111-120.

Kachlakev, D., & McCurry, D. D. (2000). Behavior of full-scale reinforced concrete beams retrofiied for shear and flexural with FRP laminates. *Composites: Part B, 31*, 445-452.

Kamali, A. Z. (2012). *Shear strength of reinforced concrete beams subjected to blast loading. MSc Thesis.* Stockholm: Royal Institue of Technology (KTH).

Kappos, A. J. (2002). *Dynamic loading and design of structures.* London: Spon Press.

Karsan, I. D., & Jirsa, J. O. (1969). Behavior of concrete under compressive loadings. *ASCE Journal of Structural Engineering, 95*(12), 2543-2563.

Khalifa, A., Gold, W. J., Nanni, A., & Aziz, A. (1998). Contribution of externally bonded FRP to shear capacity of flexural members. *Journal of Composites for Construction, 2*(4), 195-203.

Kilic, Y. (2008). *Impact and energy absorption of laminated and sandwich composites. M.Sc Thesis.* Massachusetts Institute of Technology: Massachusetts(DOUBLE CHECK).

Krausz, A. S., Dickson, J. I., Immarigeon, J.-P. A., & Wallace, W. (Eds.). (1990). *Mechanical Behavior of materials: Constitutive laws of plastic deformation and fracture.* Netherlands: Kluwer Academic Publishers.

Leppänen, J. (2002). *Dynamic behaviour of concrete structures subjected to blast and impact. Ph.D. Thesis.* Chalmers University of Technology: Göteborg, Sweden.

Lin, A., Zhitoa, L., & Zhiqiang, J. (2001). The first bridge strengthening by CFRP plate in China. *Proceedings of the International Conference on FRP Composites in Civil Engineering* (pp. 1671-1677). Hong Kong: Elsevier.

Liu, G. R., & Quek, S. S. (2003). *The finite element method: A practical course.* Oxford: Butterworth-Heinemann.

Lu, X. Z., Teng, J. G., & Ye, L. P. (2005). Bond-slip models for FRP sheets/plate bonded to concrete. *Engineering Structures, 27*, 920-937.

Macaulay, M. A. (1987). *Introduction to impact engineering.* London: Chapman and Hall.

Malvar, L. J., & Crawford, J. E. (1998a). Dynamic increase factors for concrete. *Proceedings of the Twenty-Eighth Department of Defense Explosives Safety Seminar. 18-20 Aug.* Orlando.

Mavlar, L. J., & Crawford, J. E. (1998b). Dynamic increase factors for steel reinforcing bars. *Proceedings of the Twenty-Eighth Department of Defense Explosives Safety Seminar. 18-20 Aug.* Orlando.

Mavlar, L. J. (1992). Bond of reinforcement under controlled confinement. *ACI Materials Journal, 89*(6), 593-601.

Mansour, M., & Hsu, T. T. (2005). Behavior of reinforced concrete elements under cyclic shear II: Theoretical model. *ASCE Journal of Structural Engineering, 131*(1), 54-65.

Meier, U. (1995). Strengthening of structures using carbon fibre/epoxy composites. *Construction and Building Materials, 9*(6), 341-351.

Mitolidis, G. J., Salonikios, T. N., & Kappos, A. J. (2012). Test results and strength estimation of R/C beams strengthened against flexural or shear failure by the use of SRP and CFRP. *Composites: Part B*, 1117-1129.

Mohammed, T. A. (2011). Impact load response of concrete beams strengthened with composites. *First Middle East Conference on Smart Monitoring, Assessment and Rehabilitation of Civil Structures*, (pp. 2-8). Dubai, UAE.

Mosallam, A. S., & Banerjee, S. (2007). Shear enhancement of reinforced concrete beams strengthened with FRP composite laminates. *Composites: Part B, 38*, 781-793.

Mu, Z. C., Dancygier, A. N., Zhang, W., & Yankelevsky, D. Z. (2012). Revisiting the dynamic compressive behavior of concrete-like materials. *Internation Journal of Impact Engineering, 49*, 91-102.

Ozbolt, J., & Sharma, A. (2011). Numerical simulation of reinforced concrete beams with different shear reinforcements under dynamic impact loads. *International journal of impact engineering, 38*, 940-950.

Palermo, D., & Vecchio, F. J. (2003). Compression field modeling of reinforced concrete subjected to reversed loading: formulation. *ACI Structural Journal, 100*(5), 616-625.

Parke, G., & Hewson, N. E. (Eds.). (2008). *ICE manual of bridge engineering* (2nd ed.). London: Thomas Telford.

Perumalsamy, B., Antonio, N., & Giancaspro, J. (2009). *FRP composites for reinforced and prestressed concrete structures : a guide to fundamentals and design for repair and retrofit.* New York: Taylor & Francis.

Petyt, M. (2010). *Introduction to finite element vibration analysis* (2nd Edition ed.). New York: Cambridge University Press.

Ragueneau, F., & Gatuingt, F. (2003). Inelastic behavior modelling of concrete in low and high strain rate dynamics. *Computers and Structures, 81*, 1287-1299.

Rao, S. S. (2005). *The finite element method in engineering* (4th Edition ed.). Oxford: Elsevier Butterworth-Heinemann.

Reinhardt, H. W. (1986). Tensile tests and failure analysis of concrete. *ASCE Journal of Structural Engineering, 112*(11), 2462-2477.

Rossi, P. (1997). Strain rate effects in concrete structures: the LCPC experience. *materials and Structures/Matériaux et Constructions, Supplement March*, 54-62.

Rots, J. G., Nauta, P., Kusters, G. M., & Blaauwendraad, J. (1985). *Smeared crack approach and fracture localisation in concrete.* Delft: Heron Journal 30(1).

Saatci, S. (2007). *Behaviour and modelling of reinforced concrete structures subjected to impact loads. Phd thesis.* Toronto, Canada: University of Toronto.

Saxena, P., Touanji, H., & Noumowe, A. (2008). Failure Analysis of FRP-Strengthened RC Beams. *Journal of Composites for Construction, 12*, 2-14.

Sharpe, W. N. (2008). *Springer handbook of experimental solid mechanics.* New York: Springer Science+Business Media.

Sierakowski, L. R., & Chaturvedi, S. K. (1997). *Dynamic loading and characterization of fiber-reinforced composites.* New York: John Wiley & Sons.

Sima, J. F., Roca, P., & Molins, C. (2008). Cyclic constitutive model for concrete. *Engineering Structures, 30*, 695-706.

Sinha, B. P., Gerstle, K. H., & Tulin, L. G. (1964). Stress-strain relations for concrete under cyclic loading. *ACI Structural Journal, 61*(2), 195-211.

Smith, G. M., & Young, L. E. (1955). Ultimate theory in flexure by exponential function. *ACI Journal, 52*(3), 349-359.

Smith, S. T., & Teng, J. G. (2002). FRP-strengthened RC beams. I: review of debonding strength models. *Engineering Structures, 24*, 385-395.

Täljsten, B. (2004). FRP strengthening of concrete structures: New inventions and applications. *Progress in structural Engineering and Materials, 6*(3), 162-172.

Tang, T. (2002). *Behavior of concrete beams retrofitted with composite laminates under impact loading. Ph.D. Thesis.* University of Arizona: Tucson, Arizona.

Tang, T., & Saadatmanesh, H. (2003). Behavior of concrete beams strengthened with fiber-reinforced polymer laminates under impact loading. *Journal of composites for construction, 7*, 209-218.

Tavarez, F. A. (2001). *Simulation of behaviour of composite grid reinforced conrete beams using explicit finite element methods. M.Sc. Thesis.* University of Wisconsin-Madison.

Teng, J. G., & Smith, S. T. (2003). Behaviour and strength of FRP-strengthened RC structures: a state of the art review. *Proceedings of the institution of civil engineers - structures and buildings*, (pp. 51-62).

Teng, J. G., Smith, S. T., & Lam, L. (2002). *FRP strengthened RC Structures.* Chichester: John Wiley and Sons.

Toutanji, T., Zhao, L., & Zhang, Y. (2006). Flexural behaviour of reinforced concrete beams externally strengthened with CFRP sheets bonded with an inorganic matrix. *Engineering Structures, 28*, 557-566.

Tu, Z., & Lu, Y. (2009). Evaluation of typical concrete material models ised in hydrocodes for dynamic response simulations. *International journal of impact engineering, 36*, 132-146.

van Meier, J. G. (1997). *Fracture processes of concrete.* Florida: CRC Press.

Weerheijm, J., & Van Doormaal, J. C. (2007). Tensile failure of concrete at high loading rates: New test data on strength and fracture energy from instrumented spalling tests. *Impact Engineering, 34*, 609-626.

White, T., Soudki, K., & Erki, M. (2001). Response of RC beams strengthened with CFRP laminates and subjected to a high rate of loading. *Journal of Composite Construction, 5*(3), 153-162.

Yang, L. M., & Shim, V. P. (2005). An analysis of stress uniformity in split Hopkinson bar test specimens. *International Journal of Impact Engineering, 31*, 129-150.

Yankelevsky, D. Z., & Reinhardt, H. W. (1987). Model for cyclic compressive behavior of concrete. *ASCE Journal of Structural Engineering, 113*(2), 228-240.

Yankelevsky, D. Z., & Reinhardt, H. W. (1989). Uniaxial behaviour of concrete in cyclic tension. *ASCE Journal of Structural Engineering, 115*(1), 166-182.

Zheng, D., & Li, Q. (2004). An explanation for rate effect of concrete strength based on fracture toughness including free water viscosity. *Engineering Fracture Mechanics, 71*, 2319-2327.

Zureick, A., Ellingwood, B. R., Nowak, A. S., Mertz, D. R., & Triantafillou, T. C. (2010). *Recommended Guide Specification for the Design of Externally Bonded FRP Systems for Repair and Strengthening of Concrete Bridge Elements.* Washington D. C.: Transportation Research Board.